# Universitetet i Stavanger

## FACULTY OF SCIENCE AND TECHNOLOGY

# MASTER'S THESIS

| | |
|---|---|
| Study programme/specialisation:<br><br>Petroleum Engineering/<br>Reservoir Engineering | Spring semester, 2019<br><br><br>Open |
| Author: Hedda Elise Sandstrøm Svendsen | …………………………………………<br>(signature of author) |
| Faculty supervisor: Aksel Hiort<br><br>Company supervisor: Lars Sundal (Lundin Norway) | |
| Title of master's thesis:<br><br><br>MICP-Based Rock Typing of Complex, Multi-Modal Formations in Edvard Grieg Field. | |
| Credits: 30 | |
| Keywords:<br><br>Edvard Grieg, MICP data, Parametrization, Thomeer hyperbolas, Gaussian distribution functions, Reservoir Characterization, MICP-based rock/pore typing | Number of pages: 84<br><br>+ supplemental material/other: 1<br><br><br>Stavanger, 15.06.2019 |

Title page for Master's Thesis
Faculty of Science and Technology

# Abstract

Rock/pore typing is a process of classifying reservoir rocks into units with similar petrophysical properties. When properly classified, each unit possesses a unique porosity-permeability relationship. This leads to improved reservoir characterization, which further leads to improved decision-making and finally, improved oil recovery.

This thesis investigates whether parametrization of mercury injection capillary pressure (MICP) curves could be used for rock/pore typing of the complex, multi-modal formations in Edvard Grieg field. The heterogeneous origin of the field together with different diagenetic processes lead to large variation in the porosity-permeability distribution, even within facies. Therefore, conventional rock typing methods tend to fail. This leaves room for improved reservoir characterization by using MICP-based rock/pore typing.

In this study, the parametrization of the MICP data was performed by using Thomeer hyperbolas and modified Gaussian error distribution functions, assisted by a workflow based on a spreadsheet developed by Lundin Norway. Quality control (QC) of MICP data is incorporated in this workflow to ensure that only high-quality MICP data is included in the rock/pore typing procedure. The workflow's main focus is on Thomeer curve fitting procedure.

A total of 273 MICP samples from the Edvard Grieg field were analyzed, including QC. The lithology of the samples varied from good sorted aeolian sandstones to poorly sorted alluvial fan conglomerates. The analysis has shown that parametrization of MICP data using Thomeer hyperbolas provides good results for aeolian sandstone samples, it does not, however, provide good results for alluvial fan conglomerate samples. Further investigations identified a critical weakness related to the Thomeer curve fitting procedure: it is sensitive to heterogeneous pore-throat distributions, resulting in unrealistic Thomeer parameters. These findings indicate that the Thomeer curve fitting procedure is not suitable for evaluation of alluvial fan conglomerates in Edvard Grieg field, since these formations are often associated with heterogeneous pore-throat distributions. This study has suggested that Gaussian error distributions are a better alternative than Thomeer hyperbolas for alluvial fan conglomerates, but future investigations are needed.

Moreover, investigations of the Thomeer parameters were performed and the analysis showed: high correlation between the Thomeer parameter equivalent to largest pore-throat radius and permeability measured by CCA. This was used for rock/pore typing attempts, the study suggests that the Thomeer parameter equivalent to largest pore-throat radius, could be used as cut-off parameter for rock/pore typing of the complex, multi-modal formations in Edvard Grieg field, but future studies are needed to confirm.

# Acknowledgements

# Contents

# Acronyms

**BV**  Bulk volume

**CBW**  Clay bound water

**CCA**  Conventional core analysis

**FWL**  Free water level

**FZI**  Flow Zone Indicator

**GOR**  Gas to oil ratio

**HC**  Hydrocarbons

**IFT**  Interfacial tension

**IQR**  Interquartile range

**MICP**  Mercury injection capillary pressure

**NPD**  Norwegian Petroleum Directorate

**NGL**  Natural gas liquid

**PDO**  Plan for development and operation

**PSD**  Pore-throat size distribution

**PV**  Pore volume

**QC**  Quality control

**REV**  Representative Elementary Volume

**RQI**  Reservoir Quality Index

# 1 Introduction

The spatial distribution of reservoir properties, such as porosity and permeability, is of great importance for hydrocarbon (HC) reservoir evaluation and characterization. Predictions by 3D reservoir models are used for decision making regarding, among others, optimal recovery schemes and well placements. Improved reservoir characterization will improve predictions from the reservoir models and hence improve oil recovery.

Rock/pore typing is a process of classifying reservoir rocks into units with similar petrophysical properties. When properly classified, each unit possesses a unique porosity-permeability relationship. It can be used for prediction of the spatial distribution of reservoir properties, like porosity and permeability, if a strong link is established to a 3D model parameter, such as facies. Hence, rock/pore typing leads to improved reservoir characterization and is of key importance for the accuracy of predictions by reservoir models.

Various rock typing procedures exist. Conventional rock typing procedures are often based on porosity-permeability cross plots together with Reservoir Quality Index (RQI) and Flow Zone Indicator (FZI). For carbonate reservoirs, however, rock/pore typing based on mercury injection capillary pressure (MICP) parametrization is also used, due to the complex pore structure of carbonate formations. There are several case studies of MICP-based rock/pore typing of carbonates, among others (Clerke et al., 2008; Skalinski & Kenter, 2014; Theologou, Skalinski, & Mallan, 2015). However, there are few such studies concerning clastic reservoirs.

The Edvard Grieg field is located at the Utsira High in the Norwegian North Sea. It consists of clastic reservoir rocks spanning an age range of 300 million years with wide variation in reservoir quality, from high-quality sandstone to conglomerate and porous basement. The heterogeneous origin of the field and different diagenetic processes leads to complex pore structures and great variation in porosity and permeability, even within facies. Thus, conventional rock typing procedures are not optimal.

The aim of this thesis is to investigate whether parametrization of MICP data could be useful for rock/pore typing of the complex, multi-modal formations in Edvard Grieg field. To achieve this aim, parametrization of MICP data was performed, analyzed, and quality

controlled (QC), assisted by a workflow based on a spreadsheet developed by Lundin Norway. A total of 273 MICP samples from the Edvard Grieg field were analyzed, including QC. The lithology of the samples varied from good sorted aeolian sandstones to poorly sorted alluvial fan conglomerates.

Moreover, investigations of the Thomeer parameters were performed and the analysis showed: high correlation between the Thomeer parameter equivalent to largest pore-throat radius and permeability measured by CCA. This was used for rock/pore typing attempts, the study suggests that the Thomeer parameter equivalent to largest pore-throat radius, could be used as cut-off parameter for rock/pore typing of the complex, multi-modal formations in Edvard Grieg field, but future studies are needed to confirm.

The rest of this thesis is organized as follows. Chapter 2 provides a short introduction to the Edvard Grieg field and geology, while Chapter 3 introduces the concept of rock/pore typing. Subsequently, Chapter 4 opens with theory related to capillary pressure and capillary pressure measurements. It also describes capillary pressure models and porosity-permeability models. In Chapter 5, the MICP parametrization workflow used in this thesis is described. Chapter 6 presents QC of the MICP dataset, together with the results and discussion of the MICP parametrizations. A final conclusion and future recommendations are described in Chapter 7.

# 2 Edvard Grieg

## 2.1 Field Introduction

The oil-producing Edvard Grieg field lies 180 kilometers west of Stavanger, in block 16/1 on the Utsira High in the Norwegian North Sea (Figure 2.1). The field was discovered in 2007 with the exploration well 16/1-8. The plan for development and operation (PDO) was approved in 2012, and the production started in November 2015 with production license 338. Fourteen wells have been drilled, of which ten are producers and four are water injectors. The owners are Lundin Norway (65 %), which is the operator, and OMV Norge (20 %) and Wintershall Norge (15 %), which are partners. (Lundin Norway, 2012; Oljedirektoratet, n.d.)
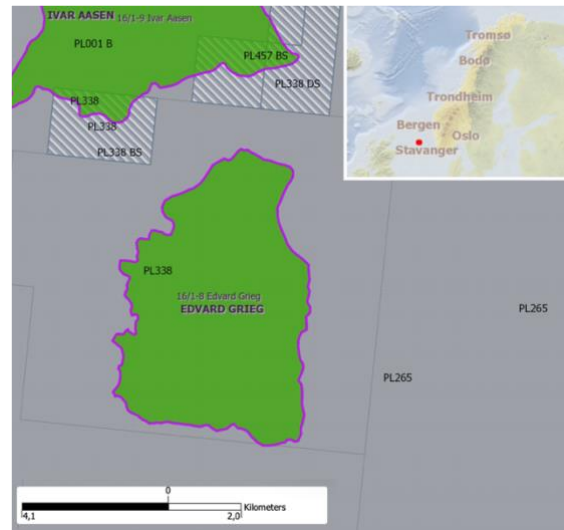


*Figure 2.1: Map of the Edvard Grieg field. Modified after NPD interactive FactMaps (2019).*

The reservoir is located at a depth of around 1900 m below surface, with a water depth of around 110 m. The reservoir fluid is moderately undersaturated oil with a low produced gas/oil ratio (GOR), with the oil-water contact (OWC) located at around 1939 m below sea level. The reservoir does not have a gas cap. The oil is transported to Sture Terminal in Hordaland through the Grane pipeline, while the gas is transported to St. Fergus in Scotland through a separate pipeline system. (Lundin Norway, 2012; Oljedirektoratet, n.d.)

The originally recoverable reserves were estimated to be 36.3 million $sm^3$ oil equivalents (o.e.), including 32.0 million $sm^3$ o.e. of oil, 2.8 million $sm^3$ o.e. of gas, and 1.5 million $sm^3$ o.e. of natural gas liquid (NGL). The expected lifetime of the field is around 30 years with a production plateau rate of 100 000 barrels of oil equivalents per day (boepd). The remaining reserves were estimated by December 2017 to be 25.8 million $sm^3$ o.e., including 22.6 million $sm^3$ o.e. of oil, 2.0 million $sm^3$ o.e. of gas, and 1.3 million $sm^3$ o.e. of NGL. The plateau extended to the end of 2019, which is two additional years compared to the PDO. This is due to a combination of better overall reserves than the pre-drill expectations together with strong reservoir performance. There is potential for further extension of the plateau through the infill

development drilling program planned for 2020. (Lundin Norway, 2012; Norwegian Petroleum, n.d.)

## 2.2  Geology

The Edvard Grieg field contains the Luno and Tellus discoveries, with reservoir rocks spanning an age range of 300 million years, from 440 to 140 million years old. These vary from porous basement rock to alluvial, aeolian, and shallow marine conglomerates and sandstones of Triassic to lower Cretaceous origin. The different depositional environments are illustrated by using Death Valley as an Edvard Grieg analogue in Figure 2.2. (Lundin Norway, 2012, 2017)

With its 2018 "Play" concept, Lundin Norway is focusing on recovering oil and gas from four entirely new reservoir types on the Norwegian continental shelf, called "plays." Three of these new reservoir types can be found in the Edvard Grieg field, namely aeolian sandstone, conglomerate, and fractured basement. These three types are described below. (Lundin Norway, 2012)

### 2.2.1  Aeolian Sandstone

One of the new plays on the Norwegian shelf is aeolian sandstone. Edvard Grieg is the only field on the Norwegian shelf where large parts of the reserves come from aeolian sandstone. (Lundin Norway, 2018a).

Aeolian sandstone is rock formed by wind-blown desert dunes, hence the name. The wind's sorting ability makes the sand type more uniform in quality and size compared to other types of sandstone formed by, for example, rivers. This gives aeolian sandstone higher permeability and porosity. As a result, production from aeolian sandstone can result in a high recovery rate while maintaining a high production rate. (Lundin Norway, 2018a)

Aeolian sandstone constitutes the majority of the reservoir in the western part of the Edvard Grieg field. It originated around 200 million years ago, when Norway was at the same latitude as North Africa is today, giving it a similar hot and dry climate. This climate, together with sand and winds, formed the desert dunes, resulting in the high-quality aeolian sandstone

reservoir at the Edvard Grieg field. An analogue is illustrated in Figure 2.2. (Lundin Norway, 2018a)

## 2.2.2 Conglomerate

Another type of reservoir rocks at Edvard Grieg are conglomerates. Conglomerates are rocks that contain large clasts, which are gravel- or boulder-sized pieces of rock with poor sorting. The clasts are cemented together in a matrix, which may consist entirely of cementing material or contain sand and/or silt. (Lundin Norway, 2018c; Mahmic, Dypvik, & Hammer, 2018; The University of Auckland, n.d.)

The conglomerates in the Edvard Grieg field originated from alluvial fan deposits around 200 million years ago. As mentioned, the climate was hot and dry, which resulted in a barren desert landscape in the area where Edvard Grieg is located today. Since there was little vegetation, floods generated by episodic heavy rains could carry large masses down the hillsides. This created alluvial fan deposits in the valley, which resulted in the conglomerate oil reservoir at Edvard Grieg. An, analogue is illustrated in Figure 2.2. (Lundin Norway, 2018c)

The clasts are made of granite with a diameter of up to 20 cm. Between the clasts, there may be sand, which gives the rock reservoir properties, or there may be silt, resulting in poorer reservoir properties. A challenge regarding the conglomerates is that conventional logs are difficult to interpret. This is due to the low porosity and strong heterogeneity of the conglomerates, with clasts considered to be without flow capacity. Hence, well logs, well test data, and core data are essential for reservoir evaluation. (Lundin Norway, 2018c)

## 2.2.3 Fractured Basement

Fractured basement is the third new reservoir type that exists in the Edvard Grieg field. Previously, it was not considered commercial to produce HC from granitic basement rock. This was mainly due to high rock density, which is usually connected with low porosity. However, if the granite basement is fractured and weathered, meaning that water has flowed through the fractures and dissolved minerals, it can be both porous and permeable. It may then act as good reservoir rock, where cracks and pores can become saturated with

hydrocarbons (HC). A stronger degree of weathering leads to higher dissolution of granite, which gives relatively better reservoir properties. Fractured granite basement underlies the main reservoir rocks in the northern part of the Edvard Grieg field, across the Tellus area. (Lundin Norway, 2018b, 2018d)



*Figure 2.2: Death Valley can be used as an analogue for the Edvard Grieg field. This figure illustrates the depositional environments that resulted in the heterogeneous formations of the Edvard Grieg field. Modified after map retrieved from Google Earth Pro (June 19, 2015).*

# 3 Rock/Pore Typing

The aim of this thesis is to evaluate the potential to use MICP-based rock/pore typing for the complex, multi-modal formations in the Edvard Grieg field. Among other applications, this could improve predictions of permeability from porosity. The purpose of this chapter is to introduce rock/pore typing.
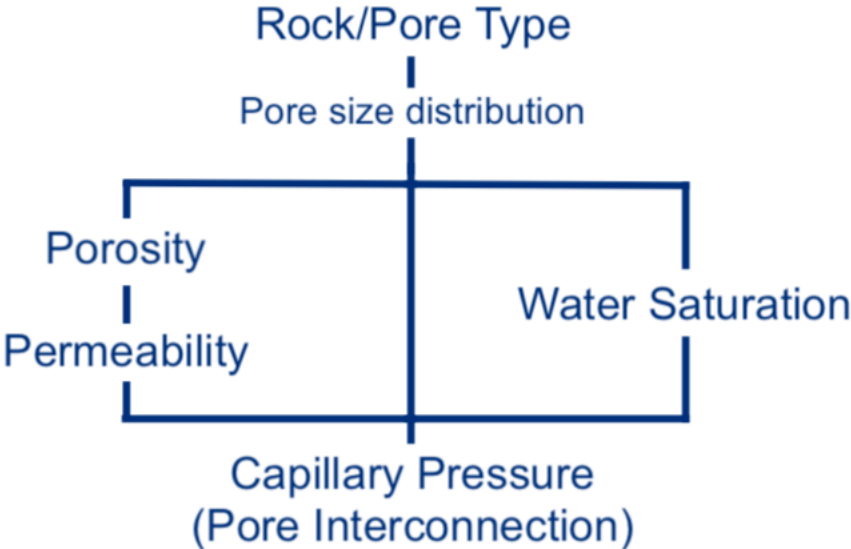


*Figure 3.1: Illustrates how rock/pore types are connected to capillary pressure and other parameters. Modified after Archie (1950).*

There are several different definitions of a rock/pore type, but a frequently used one is Gunter, Finneran, Hartmann, and Miller (1997): "units of rock deposited under similar conditions which experienced similar diagenetic processes resulting in a unique porosity-permeability relationship, capillary pressure profile and water saturation for a given height above free water in a reservoir" (p. 1). Figure 3.1 illustrates how a specific rock/pore type and parameters are connected. According to Archie (1950), a specific "rock type will have certain effective pore-size distributions which will produce a particular family of capillary pressure curves. The pore-size distribution controls the porosity and is related to the permeability and water saturation. Further, a certain rock will exhibit a relation between porosity and permeability" (p. 944).

Rock/pore typing is a way of classifying reservoir rocks into units with similar petrophysical properties. Various definitions of and approaches to rock/pore typing exist, and the petroleum

industry lacks a common definition (Skalinski & Kenter, 2014). Conventional methods are often based on cross plots of porosity and permeability together with RQI and FZI to identify rock types (Amaefule, Altunbay, Tiab, Kersey, & Keelan, 1993). However, these tend to fail for formations with complex pore systems.

In this thesis, rock/pore typing is defined as the process of identifying rock/pore types with unique porosity-permeability relationships at core scale. Extrapolate these to log scale and link to geological attributes in a 3D model for field scale application. When done properly, rock/pore typing can be used to estimate permeability distribution by using the unique porosity-permeability relationship that a given rock type possesses. (Guo, A. Diaz, Paz, Smalley, & A. Waninger, 2007)

MICP based rock/pore typing attempts to correlate pore-throat (passage between pores) structures to petrophysical properties such as porosity and permeability, by using parametrization of MICP curves. To evaluate the potential for improved reservoir characterization of the Edvard Grieg field. Mainly based on the MICP parametrization studies of Clerke et al. (2008) and Theologou et al. (2015). Clerke et al. (2008) used Thomeer hyperbolas (Thomeer, 1983) for parametrization of MICP curves, and Theologou et al. (2015) used modified Gaussian error functions.

During rock/pore typing, the properties of interest are storage and flow of fluids. It is possible that two facies can be grouped as one rock type, or that two or more rock types are needed to describe one facies (Tavakoli, 2018). The reason is that, even if similar facies were deposited in the same depositional environment, they may have been subject to different diagenetic processes, resulting in different petrophysical properties. (Gomes, Teresa Ribeiro, J. Strohmenger, Naghban, & Kalam, 2008)

# 4 Theory

## 4.1 Surface Forces

The main objective of this thesis involves parametrization of MICP curves. Hence, it is essential to have an understanding of capillary pressure, which is closely related to interfacial tension, wettability, and pore-throat radius. This chapter provides an introduction to these parameters and how capillary pressure is measured.

### 4.1.1 Surface Tension

Speight (2017b, p. 685) defines surface tension as "the elastic tendency of a fluid surface which makes it acquire the least possible surface area". The phenomenon occurs because of attractive forces between liquid molecules and because the system aims to minimize its energy.
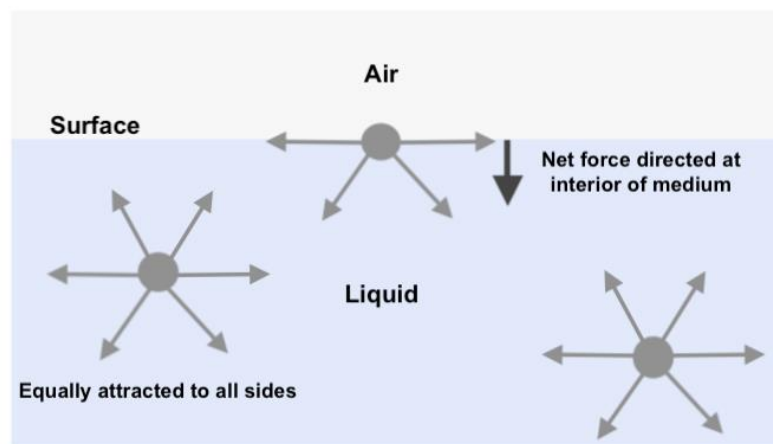


*Figure 4.1: Illustration of surface tension. Liquid molecules experience strong cohesive forces. When a liquid molecule is completely surrounded by other liquid molecules, it is equally attracted to all sides, whereas when a liquid molecule is at an interface, it experiences a net force directed at the interior of the medium.*

When a liquid molecule is completely surrounded by other similar molecules, it is equally attracted to all sides, and thus experiences balanced cohesive forces (zero net force). In contrast, when a liquid molecule is at an interface, like liquid-gas, it experiences greater attraction to its own molecules (called cohesion) than to the gas molecules (called adhesion). This leads to a net force directed at the interior of the medium; see Figure 4.1. This force is called surface tension, and it is responsible for liquids contracting to the smallest surface area

possible. The force is often referred to as interfacial tension (IFT) when the interface is between two immiscible liquids. Values for IFT can be found through laboratory experiments or in the literature. (Glover, n.d.; Speight, 2017a)

## 4.1.2 Wettability

Wettability is defined as the "the tendency of one fluid to spread on or adhere to a solid surface in the presence of other immiscible fluids" (Speight, 2017b, p. 745).

At a solid surface, the wetting fluid will displace non-wetting fluid. If a liquid is placed on a solid surface, the shape it will make depends on the wettability; see Figure 4.2. At one extreme, if the surface is completely non-wet, the liquid drop will remain a sphere to minimize the contact with the surface. At the other extreme, if the surface is completely wet, the fluid will spread out on the entire surface. If the wetting is somewhere in between, the bottom of the liquid drop will flatten out. The extent to which this occurs depends on the wetting. The liquid drop will make a contact angle ($\theta$) with the surface; this is shown in Figure 4.2, and possible values are listed in Table 4.1. (Abdallah et al., 2017)
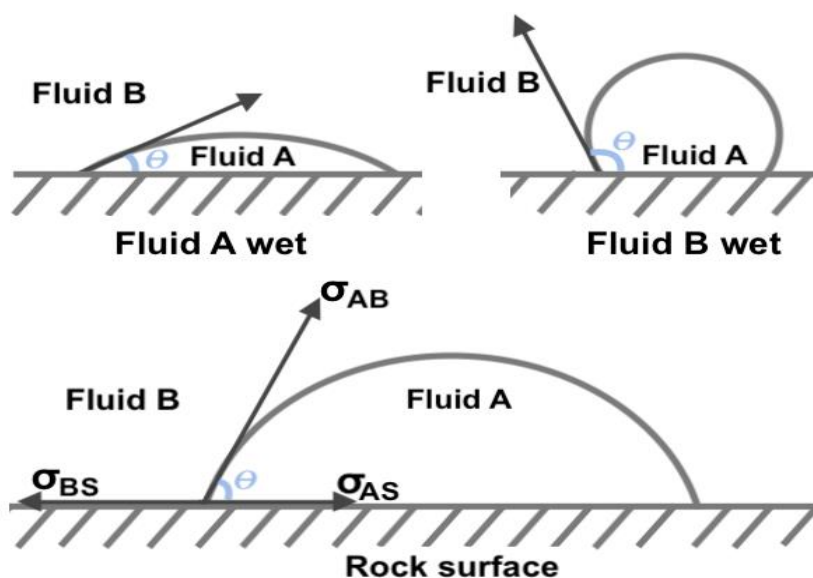


*Figure 4.2: Illustration of the equilibrium contact angle that a liquid drop makes on an ideal solid surface for different wettabilities. Modified after Anderson (1986).*

*Table 4.1: Contact angles ($\theta$) for different wettabilities of the surface. (Glover, n.d.)*

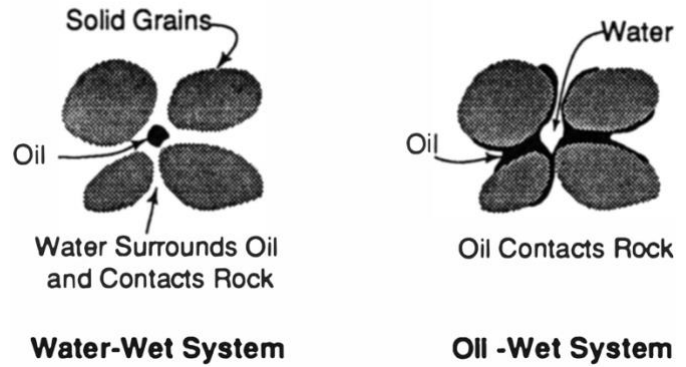| Contact angle measured through Fluid A, $\theta$ [degrees] | Wettability of the surface |
|---|---|
| 0° | Completely Fluid A wet |
| 0° − 90°, | Fluid A wet |
| 90° | Neutrally wet |
| 90° − 180° | Fluid B wet |
| 180° | Completely Fluid B wet |

The wettability of a solid surface can be studied by measuring the contact angle. Young's equation describes the contact angle on an ideal solid surface:

$$\sigma_{AB} \cos \theta = \sigma_{BS} - \sigma_{AS}, \qquad\qquad (4.1)$$

where $\sigma_{AS}$ is the interfacial energy between fluid A and the solid, $\sigma_{BS}$ is the interfacial energy between fluid B and the solid, $\sigma_{AB}$ is the interfacial energy between fluid A and fluid B, and $\theta$ is the contact angle. Equation (4.1) can be derived from the force balance between the interfacial energies shown in Figure 4.2. Young's equation applies for ideal, smooth surfaces, but most rock surfaces are heterogeneous, and few can be prepared with a smooth surface. (Ebnesajjad & Ebnesajjad, 2013, pp. 11-12)

When a porous solid is in contact with fluids, it will tend to imbibe the wetting phase. Thus, the non-wetting phase will be displaced, which is called imbibition. The wettability of a reservoir rock can either be water-wet, oil-wet, or an intermediate state between the two, called intermediate-wet. Intermediate-wetting can mean that the rock is neutral-wet, which is when the rock does not have a strong preference for contacting either the water or the oil, or that the rock is mixed-wet, meaning that some surfaces or grains of the rock are water-wet while others are oil-wet. (Schlumberger, n.d.-b)

In reservoir rocks, different minerals may have different wettability. Sandstone, carbonate, and dolomite are usually water-wet prior to oil migration (Figure 4.3a). Oil migration is a drainage process (i.e. a process with decreasing wetting-phase saturation). However, when the pore surfaces are contacted by oil during and after migration, the surfaces may be altered to oil-wet (Figure 4.3b). This may leave the



*Figure 4.3: Illustration of (a) a water-wet system and (b) an oil-wet system, from left to right, respectively. (Green & Willhite, 1997)*

contacted surfaces oil-wet while the un-touched surfaces remain water-wet, resulting in mixed-wet conditions. Since oil migrates more easily through the larger pore-throats, large pores and pore-throats are more likely to be oil-wet, while smaller pores and pore-throats are most likely to be water-wet. Thus, the mixed-wet state depends on pore and pore-throat geometry in addition to surface roughness. (Abdallah et al., 2017; Christiansen, 2005; Schlumberger, n.d.-a)

Several methods exist to measure the wettability of a reservoir. The most common methods performed on cores are the Amott (imbibition) test and the USBM (centrifuge) test. Values also exist in the literature. (Abdallah et al., 2017)

### 4.1.3  Capillary Pressure

Capillary pressure is "the difference in pressure across the interface between two phases and has also been defined as the pressure differential between two immiscible fluid phases occupying the same pores caused by interfacial tension between the two phases that must be overcome to initiate flow" (Speight, 2017b, p. 109).

Capillary pressure, $P_c$, is related to IFT and curvature of the interface through:

$$P_c = P_{nw} - P_w = \sigma \left( \frac{1}{R_1} + \frac{1}{R_2} \right). \qquad\qquad (4.2)$$

This is known as the Young-Laplace equation, where $P_{nw}$ and $P_w$ are the pressure of the non-wetting phase and of the wetting phase, respectively, $R_1$ and $R_2$ are the principal radii of curvature of the interface, and $\sigma$ is the IFT. (Brooks & Corey, 1964)

When a capillary tube is placed in contact with a wetting fluid, the wetting fluid is drawn into the tube due to net cohesive forces. This phenomenon is known as capillary rise. The fluid continues to rise until equilibrium is reached, which is when the capillary force is balanced by the gravitational force. This results in an interface with an approximately half sphere shape; see Figure 4.4. Then, the two radii of the curvature are equal, and equation (4.3) is reduced to

$$P_c = P_{nw} - P_w = \frac{2\sigma}{R}, \qquad (4.3)$$

where the radius of the straight capillary tube, $r$, is related to the radius of the curvature, $R$, and the contact angle, $\theta$, as follows:

$$r = R \cos \theta. \qquad (4.4)$$

Inserting equation (4.4) into (4.3) yields:

$$P_c = (P_{nw} - P_w) = \frac{2\sigma \cos \theta}{r}, \qquad (4.5)$$

The equation above shows that capillary pressure rises with increasing IFT and decreasing capillary tube radius. (Christiansen, 2005; Glover, n.d.)
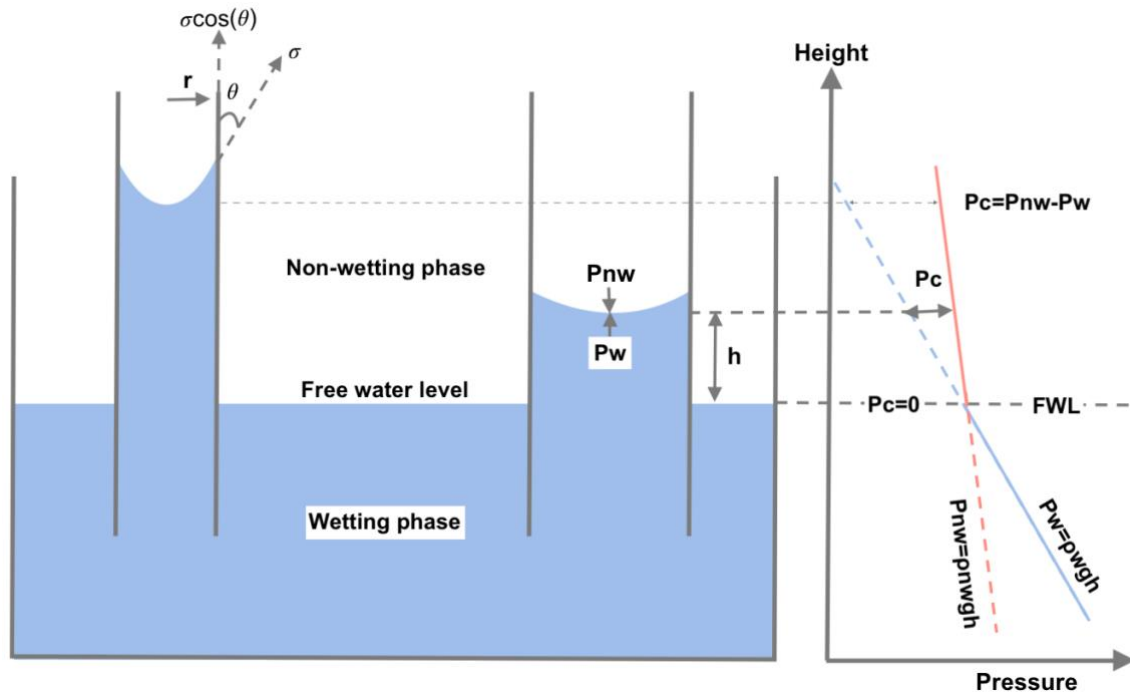
*Figure 4.4: Illustration of capillary rise. The wetting fluid rises in the capillary tube until equilibrium is reached. Inspired by Vavra et al. (1992).*

Capillary pressure is related to the height of the capillary rise ($h$) through the following equation:

$$P_c = P_{nw} - P_w = (\rho_w - \rho_{nw})gh, \tag{4.6}$$

where $\rho_w$ and $\rho_{nw}$ are the density of the wetting phase and non-wetting phase, respectively. $h$ is measured as height above free water level (FWL); see Figure 4.4. FWL is defined as the depth at which the capillary pressure is zero, $P_c = 0$. Rearranging equation (4.6) gives the height:

$$h = \frac{P_c}{(\rho_w - \rho_{nw})g}. \tag{4.7}$$

The above equations shows that the capillary pressure rises as height above FWL increases. (Glover, n.d.; Vavra et al., 1992)

The complex geometry of pore systems can be approximated using a simplified model known as the bundle of capillary tubes model, where a capillary tube radius is analogous to pore-

throat size. Hence, a cylindrical approximation of pore-throat radius can be calculated from capillary pressure by rearranging (4.5) to solve for pore-throat radius:

$$r = \frac{2\sigma \cos\theta}{P_c}. \tag{4.8}$$

Combined with equations (4.6) and (4.7) shows capillary pressure rises with decreasing pore-throat radius and with an increasing height above FWL. In other words, as HC column height increases, the water saturation decreases. This explains how HC are able to enter increasingly small pore-throats as height above FWL rises. (Glover, n.d.; Vavra et al., 1992)

## 4.2  Capillary Pressure Measurements

As previously mentioned, during migration, HC displaces formation water in the reservoir, which is usually a drainage process. The HC saturation increases with HC column height, as HC are able to enter smaller pore-throats. The capillary pressure curve can be evaluated using laboratory experiments conducted on rock samples, where non-wetting fluid displaces wetting fluid by applying increasing external pressure. For each pressure step, the non-wetting fluid saturation is measured.

The experiment result in a capillary pressure curve, where capillary pressure is plotted against non-wetting or wetting phase saturation. A capillary pressure curve for a sample with a single pore system is illustrated in Figure 4.5, where a pore system is defined as "an aggregate of pores and pore throats that shares a similar morphology" (Hartmann & Beaumont, 2000, p. 18). The geometry of a pore system includes pore and pore-throat sizes, pore system shapes, pore connectivity, and the ratio of pore-throat radius to pore radius.
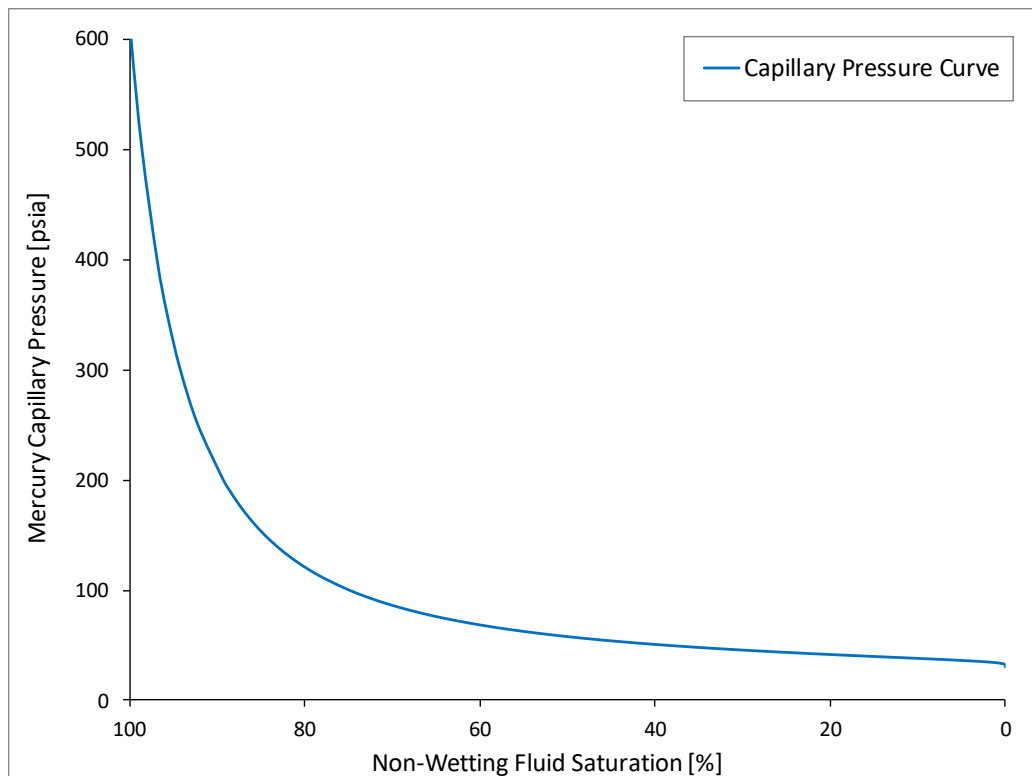
*Figure 4.5: Illustration of a capillary pressure curve for a sample with a single pore system. As the external pressure is increased, the non-wetting saturation also increases.*

Capillary pressure also provides an estimation of pore-throat size distributions using equation (4.8). This distribution is essential to reservoir quality since it has strong influence on many petrophysical properties, like permeability and saturation (Elnaggar & Temraz, 2018)

There exist multiple methods to measure capillary pressure curves in rocks. The three most used in the petroleum industry are MICP, porous plate, and centrifuge. These methods are discussed below, with greater detail given on MICP since the capillary pressure data used in association with this thesis were obtained using this method.

## 4.2.1  MICP Method

Capillary pressure measurements can be performed using the MICP method. This method is routinely employed in the petroleum industry to evaluate geological/petrophysical parameters of conventional cores, sidewall cores, and cuttings. It involves injecting mercury into a cleaned, dry rock sample. Mercury is a non-wetting fluid, so pressure must be applied in order for mercury to intrude the rock sample. In other words, it is not a spontaneous process and

provides measurements of drainage capillary pressure. (Purcell, 1949; Shafer & Neasham, 2000)

First, the rock sample is weighed and placed in a chamber. Air is evacuated from the chamber and then filled with mercury (Figure 4.6). Next, the pressure on the mercury is increased in the desired number of steps, ranging from vacuum to 60 000 psi. (McPhee, Reed, & Zubizarreta, 2015)
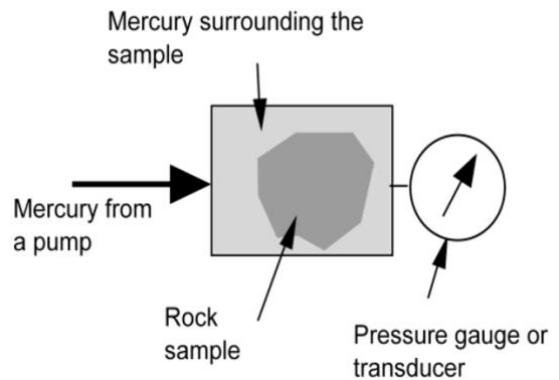


*Figure 4.6: Simple illustration of MICP measurements. (Christiansen, 2005)*

 The first volume of mercury enters the pores of the rock sample when the displacement pressure is reached, which is the pressure required for mercury to overcome the capillary pressure of the largest pores of the rock sample. As the pressure is increased beyond the displacement pressure, mercury overcomes higher entry pressures. As a result, mercury is able to intrude increasingly small pore-throats (Glover, n.d.; Hirasaki, n.d.; Purcell, 1949)

At each pressure step, the volume of mercury injected into the sample is measured, which yields the mercury saturation. Based on the experiment, the capillary pressure curve can be constructed by plotting the pressure in the mercury at each step against the volume of mercury intruded. The shape of the capillary pressure curve contains information about pore-throat sizes and pore geometries. (Glover, n.d.)
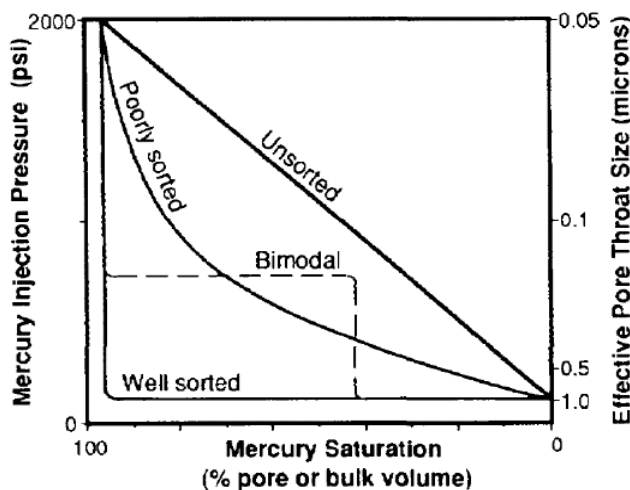


*Figure 4.7: Idealized MICP curves for samples with different degrees of sorting. All have the same displacement pressure and maximum mercury saturation, but different MICP curves due to different pore-throat size distributions: from the one extreme of a very well sorted sample with a flat plateau (lower curve), to a poorly sorted sample with a steeper plateau, and to the other extreme of an unsorted sample (upper curve). (Vavra, Kaldi, & Sneider, 1992)*

17

Idealized MICP curve shapes for samples with different degrees of sorting are shown in Figure 4.8. Well sorted samples, which are dominated by similarly sized pore-throats, yield long, flat plateaus. The plateaus become steeper with lower degrees of sorting. Thus, even though samples with different degrees of sorting may have the same displacement pressure and maximum mercury saturation, their different pore-throat size distributions will result in different fluid saturation distributions. This can be observed from the difference in the shapes of the MICP curves in Figure 4.8. (Vavra et al., 1992)

Some of the advantages of the MICP method are that it is low-cost and faster than the other methods mentioned. It generates large amounts of data in a short time and is therefore usually the preferred method to define pore-throat size distributions. In addition, it can be performed on samples that are much smaller than conventional core analysis (CCA) plugs, and these samples can have irregular shapes and even be broken into several pieces, like core chips. Together, this normally makes MICP a favored and routine method. (McPhee et al., 2015; Shafer & Neasham, 2000)

However, there are also disadvantages associated with the method. First, MICP is not a capillary test, since there is no strong wetting phase and provides total wetting phase drainage ($s_{air} = 0$) if the pressure is raised high enough. Furthermore, mercury-air is not representative of reservoir fluids, so corrections are needed. A closure correction is also often required. Some other disadvantages are that the test is sensitive to sample size, destructive, and not suitable for samples with sensitive or reactive clays, as clays might be damaged during cleaning and drying when clay bound water (CBW) is removed. (McPhee et al., 2015)

## 4.2.2  Other Methods

### 4.2.2.1  Porous Plate

Another method to measure capillary pressure is the porous plate method.

First, the sample is fully saturated with a wetting fluid, typically formation water. Then, one end of the sample is placed on a porous plate in a pressure vessel (Figure 4.9). The porous plate is saturated with the same formation water as the sample and is a semipermeable membrane that is only permeable to the water. Non-wetting fluid, oil or gas, is then admitted under pressure into the vessel. As a result, some of the water is expelled from the sample through the porous plate. The expelled water is



*Figure 4.8: Illustration of porous plate capillary pressure measurement. (Christiansen, 2005)*

collected, and the volume is measured. After equilibrium is reached, the procedure is repeated by increasing the pressure of the non-wetting phase in steps. As a result, the capillary pressure curve can be constructed by plotting the pressure against water saturation (or non-wetting phase). (Ahmed, 2010; Glover, n.d.)

Some of the advantages of the porous plate method are that actual reservoir fluids can be used for the measurements, so no fluid correction is needed, and the method is considered the most accurate. In addition, it is not destructive, so the samples are reusable, and it is the preferred method for clay-rich samples. In addition, it is usually cheaper than the centrifuge method. (McPhee et al., 2015)

However, it is also a slow method: several weeks or months may be required to reach equilibrium for each pressure step, and the shape of the resulting capillary pressure curve is sensitive to the time allowed to reach equilibrium. Another disadvantage is that it requires the sample to be water-wet to provide representative drainage capillary pressure. (Glover, n.d.; McPhee et al., 2015)

### 4.2.2.2 Centrifuge

The third method to measure capillary pressure is the centrifuge method.

First, the sample is fully saturated with a wetting fluid, typically water, and placed inside a centrifuge core holder (Figure 4.10). Then, it is rotated with steps of increasingly high speed. The centripetal force displaces wetting fluid from the sample and replaces it with non-wetting fluid (oil or air). The displaced wetting fluid accumulates in the fluid collector and the volume is measured for each rotational speed. When equilibrium is reached, the speed is increased to the next step. As the speed increases, the centripetal force is able to displace the wetting fluid from increasingly small pores, and the corresponding capillary pressures are calculated. The water saturation is calculated from the collected volumes for each rotational speed. Then, the capillary pressure curve can be constructed by plotting the capillary pressure against the water saturation (or non-wetting phase). (Christiansen, 2005; Glover, n.d.)
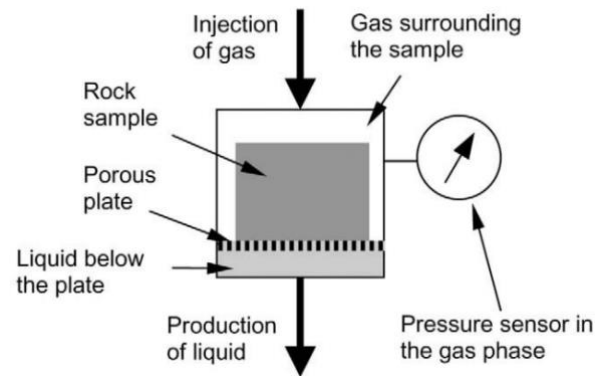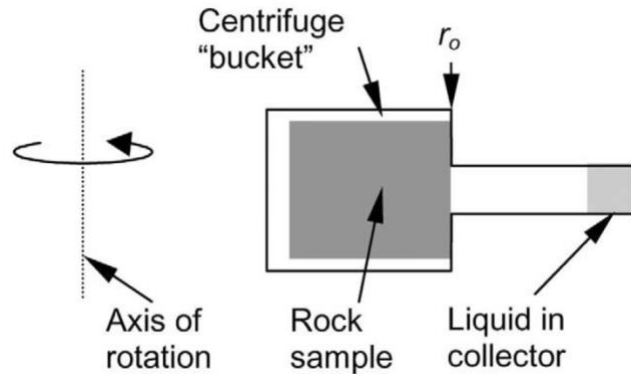
*Figure 4.9: Illustration of centrifuge capillary pressure measurements. (Christiansen, 2005)*

Some of the advantages of the centrifuge method are that it is faster than the porous plate method and that it is relatively simple. The test is not destructive, so the samples can be reused for other tests. Furthermore, the test can be used for both drainage and imbibition cycles, and tests with reservoir conditions are possible. (McPhee et al., 2015)

On the other hand, the centrifuge method is the most expensive method. Moreover, the rotational speed generates an unusual stress field where fracturing of the sample is possible, so it should not be used for samples sensitive to these kinds of stress. Another drawback is that the capillary pressure is a function of distance from the axis of rotation, and raw data therefore needs to be corrected. Some additional disadvantages are that air is typically used as displacing fluid and, as for the porous plate method, the sample is required to be water-wet to produce a representative drainage capillary pressure curve. (Glover, n.d.; McPhee et al., 2015)

## 4.3  Reliability of Measurements

The main objective of an MICP study is often to measure capillary properties for use in reservoir evaluation and modeling, like in the present work. Thus, the reliability of the measurements is a critical issue. To obtain reliable MICP data, it is important to ensure proper sampling of rocks for measurements, measurement methods, and treatment of data from the measurements, among others. The measurement methods were described above, but some other critical issues related to the reliability of the measurements are elaborated below. (Christiansen, 2005)

### 4.3.1  Sample Selection

Proper sampling of rocks for measurements is essential to achieve reliable MICP data. To be able to use MICP data for reservoir characterization such as rock/pore typing, it is important to gather sufficient and representative data to extrapolate representative pore/rock types from clustering analysis. Sample selection is an important step to achieve this. (Theologou et al., 2015)

How often cores are taken and how the samples are chosen are essential for proper sampling. Biased sampling, like selecting the most homogeneous samples, might result in undesirable bias in the results. Therefore, the selection should be based on a logical or statistical selection of samples. The MICP data should be able to reflect the porosity and permeability distribution from CCA data. If samples are selected from a narrow range of porosity-permeability relationships, this may lead to an unrepresentative dataset and, hence, unrepresentative results based on that dataset. Poor or biased sample collection is one of the reasons why saturation-height models from capillary pressure data fail. The minimum requirement for statistical validity is 10 samples per facies or rock/pore type. (Christiansen, 2005; McPhee et al., 2015)

### 4.3.2  Sample preparation

Air is the wetting phase in the mercury-air system, and since air is not a strong wetting phase, all water needs to be removed from the sample. If not, the water will act as the wetting phase instead of air, yielding error in the results. MICP samples are usually cleaned by immersion in a Soxhlet extractor and convection oven drying. Chemical and visual checks should be conducted to ensure complete removal of fluids. However, the harsh preparation techniques

have disadvantages, one being that CBW will most likely be removed from the system, hence requiring a correction for these cases. (McPhee et al., 2015)

### 4.3.3  Sample Size

The MICP method can be performed on samples of various sizes and shapes. However, Hirsch and Thompson's (1995) percolation theory states that sample size and shape affect capillary pressure measurements: smaller samples with higher "surface area/bulk volume" tend to give slightly lower displacement pressure and a more optimistic MICP curve. Thus, the ideal MICP sample "should be as large as possible but still compatible with the bulk and pore volume capacity of the glass penetrometer" (Shafer & Neasham, 2000, p. 5). This is typically a sample size of 1x1 inch.

When it comes to sample size, the representativeness of the sample for the whole CCA plug must also be discussed. CCA plugs are typically 1-1.5 x 2 inch in size, while MICP samples are smaller. They can even be plug end-trims or chips (an even smaller piece of an end-trim). For homogeneous samples, end-trims and chips are usually representative of the whole plug and hence yield reasonable results, but for heterogeneous samples, like conglomerates, they may not be. The porosity and permeability measurements are usually performed on the whole CCA plug, and results from end-trims and chips may thus cause problems when trying to relate measured permeability to pore structure. (Theologou et al., 2015)

The volume of the MICP sample should be larger than the representative elementary volume (REV). The REV can be defined as the minimum volume where the average values for a quantity of interest, like porosity or permeability, remain more or less constant – that is, when the investigated "parameter becomes independent of the size of the sample" (Al-Raoush & Papadopoulos, 2010, p. 69). The REV should be "such that parameters that represent the distributions of the void space and of the solid matrix within it are statistically meaningful" (Bear & Bachmat, 1991, p. 5). This is especially critical when it comes to conglomerates where the volume of the MICP sample (especially for end-trims and chips) may be smaller than REV, or where a sample may contain only matrix or clast, or a distribution of such that is not representative. (Bear & Bachmat, 1991)

To summarize, performing MICP analysis on larger pieces of CCA plugs will increase the reliability of measurements compared to MICP analysis performed on end-trims or chips. Another advantage is that all of the measured data, like porosity and permeability, come from the same sample. This is especially important when the aim is to correlate measured permeability and pore-throat distribution, as is the case in this thesis. (Theologou et al., 2015)

### 4.3.4  Data Correction

As mentioned above, corrections are required for MICP data to be reliable and applicable to reservoir settings. Some of these corrections are discussed below.

#### 4.3.4.1  Blank Cell Corrections

During high-pressure MICP measurements, compression of the components of the MICP testing equipment occurs. To account for these effects, blank corrections are needed. These are often performed by using correction data from a blank run without a sample, and they are usually incorporated in the MICP instrumental software. The corrections do not correct for grain compressibility. (Shafer & Neasham, 2000)

#### 4.3.4.2  Closure Correction

A sample is rough and may contain surface irregularities, like induced fractures. If mercury is injected to samples with surface voids larger than the largest pore-throats, mercury first fills the voids before it intrudes the true pore system of the rock sample; see Figure 4.10. This results in a so-called closure effect, also known as conformance effect, in the MICP data, which is due to the non-wetting characteristics of the mercury. The closure effect appears in the MICP data as lower displacement pressure than actual and must be corrected. The correction, called closure correction, is performed by subtracting the apparent volume of mercury intruded prior to the actual displacement pressure from the MICP raw data. Hence, measure-dependent data that is not a property of the rock is removed. Smaller samples with irregular surfaces, like end-trims, require greater correction than larger samples, such as plugs. This is because smaller samples have larger external surface area to volume ratios. The closure correction is subjective and thus leads to uncertainty. In addition, if some pore-throats are large enough, mercury may intrude the sample while closing around it, which makes it

difficult to discriminate between their contribution to the increasing mercury saturation. (McPhee et al., 2015; Shafer & Neasham, 2000)
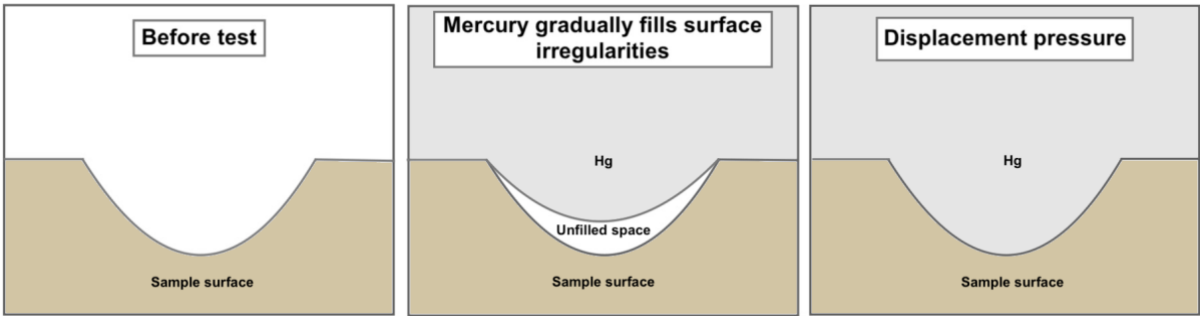


*Figure 4.10: Schematic illustration of closure effect on a samples outer surface.*

### 4.3.4.3 Fluid Correction

To be able to apply the capillary pressure curve to the reservoir, it must represent reservoir fluids and rocks; therefore, correction is needed. The MICP data can be converted from a mercury-air system to an oil-water system by using the following relationship:

$$P_c(ow/rock) = P_c(ma/rock)\frac{\sigma_{ow}\cos\theta_{ow}}{\sigma_{ma}\cos\theta_{ma}}, \qquad (4.9)$$

where ma is mercury/air. In this thesis, values from the literature are used for the contact angle and surface tension of the different systems, as listed in. (Glover, n.d.; Vavra et al., 1992)

Table 4.2: Contact angle and surface tension values used in this thesis.

| System | IFT ($\sigma$) | | Contact angle ($\theta$) | $\cos\theta$ | $\sigma\cos\theta$ |
|---|---|---|---|---|---|
| Mercury/air/rock | 485 | dynes/cm | 130 | 0.643 | 312 |
| Oil/brine/rock | 30 | dynes/cm | 30 | 0.866 | 26 |

## 4.4 Capillary Pressure Models

Capillary pressure can be used to obtain information about other reservoir properties, such as water saturation and permeability, using the relationships between them. Several capillary pressure models exist. The ones discussed here are the Leverett J-function, Thomeer model, Brooks and Corey's model, and the Swanson permeability relation.

### 4.4.1 Leverett J-function

The Leverett J-function, $J(S_w)$, is a dimensionless correlation between capillary pressure, water saturations and rock properties, given by

$$J(S_w) = \frac{P_c}{\sigma \cos \theta} \sqrt{\frac{k}{\phi}},$$

(4.10)

where $k$ is permeability, $\phi$ is porosity, $\sigma$ is IFT, and $\theta$ is the contact angle. $J(S_w)$ can be obtained by plotting $\frac{P_c}{\sigma \cos \theta} \sqrt{\frac{k}{\phi}}$ against $S_w$. Then, it may be used to calculate capillary pressures. Note that by assuming $J(S_w)$ is unaffected by fluid type, one can obtain the fluid correction relationship given in equation (4.9). (Fanchi, 2010)

### 4.4.2 Thomeer model

Thomeer (1960, 1983) presented a mathematical model describing MICP data "based on the observation that the location and shape of a capillary pressure curve reflect characteristics of the pore structure of the sample" (p. 73). He observed that the MICP curve present in a log-log plot of capillary pressure against bulk volume occupied by mercury could be approximated by a hyperbola, and that the curve could be uniquely described by three pore-network parameters.

Thomeer (1960, 1983) presented the following hyperbola equation:

$$\frac{V_b}{V_{b\infty}} = e^{-G/(\log P_c/P_d)},$$

(4.11)

where $V_b$ is the bulk volume occupied by mercury and the three pore-network parameters are $P_d$, $V_{b\infty}$ and $G$. $P_d$ is the displacement pressure, $V_{b\infty}$ is the percent bulk volume occupied by mercury at infinite capillary pressure and $G$ is the pore geometrical factor.

Thomeer (1983) also related absolute permeability ($k_a$) to the three pore-network parameters: $G$, $V_{b\infty}$, and $P_d$. He presented the following empirical relationship:

$$k_a = 3.8068 G^{-1.3334} \left(\frac{V_{b\infty}}{P_d}\right)^{2.0}. \tag{4.12}$$

He obtained this by using weighted regression from 279 samples, with $k_a$ in [mD], $V_{b\infty}$ in [%], $P_d$ in [psi] and G is unitless.

### 4.4.3  Brooks and Corey

Brooks and Corey (1964) provided the following power-law relationship

$$S_e = \left(\frac{P_d}{P_c}\right)^{\lambda}, \tag{4.13}$$

where $\lambda$ is the pore-size distribution index and $P_d$ is displacement pressure. $S_e$ is defined as the effective saturation of the wetting phase given by:

$$S_e = \frac{S - S_r}{1 - S_r}, \tag{4.14}$$

where $S$ is the saturation of the wetting phase and $S_r$ is the residual wetting phase saturation.

### 4.4.4  Swanson Permeability Relation

Swanson (1981) sought to improve Purcell (1949) and Thomeer (1960) with

improvements that would enhance our ability to estimate permeability of small rock samples such as portions of sidewall core samples or drill cuttings. Capillary pressure curves measured on drill cuttings usually present a very gradual, poorly defined plateau … The depressed plateau leads to optimistic estimates of permeability using

the Purcell approach. Also, cuttings capillary pressure data are not well represented by a hyperbola. This results in poor fits of Thomeer parameters to cuttings data. (p. 2498)

Swanson (1981) used a data set consisting of 203 sandstone samples from 41 formations and 116 carbonate samples from 33 formations, all with permeability and capillary pressure measured on the same sample. He obtained the following permeability and MICP correlation using regression analysis:

$$k_a = 399 \left( \frac{S_b}{P_c} \right)_A^{1.691},$$
(4.15)

where $k_a$ is permeability and $S_b$ corresponds to the Thomeer parameter $V_b$. The apex ($A$) is defined as the intersection of the capillary pressure curve in the log-log plot of $P_c$ against $S_b$ with a 45° tangent to the origin of the hyperbolic axes; see Figure 4.11.
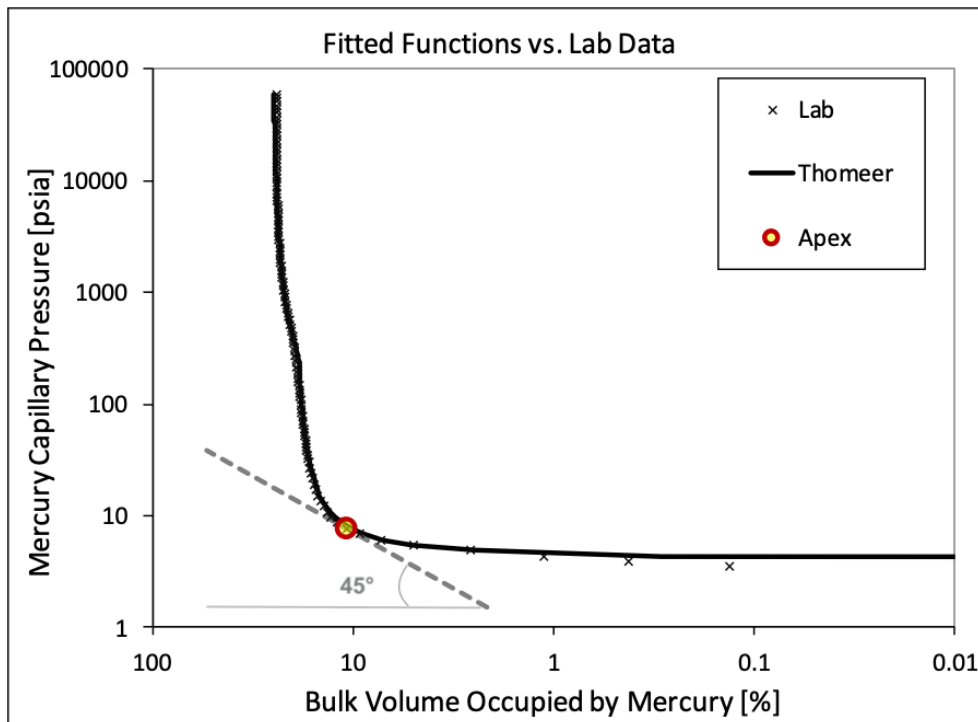


*Figure 4.11: Illustrating the definition of correlating parameter at the apex (A).*

### 4.4.5　MICP Curve Fitting Algorithms

For parametrization of MICP curves, curve fitting algorithms are used. While several exist, the Thomeer hyperbolas and Gaussian error functions are used in the present study. The main focus is on the Thomeer hyperbolas.

#### 4.4.5.1　Thomeer Hyperbolas

The fundamentals of the Thomeer model were described in Section 4.4.2. Further elaboration is given below.

Figure 4.13 illustrates the Thomeer (1960) hyperbola from equation (4.11) for one pore system. The equation can be derived by considering the general equation for a hyperbola present in a log-log plot, which is given by:

$$(\log y - \log y_a)(\log x - \log x_a) = k, \qquad (4.16)$$

where $x_a$ and $y_a$ are the vertical and horizontal asymptote, respectively, and k is the shape factor. As shown in in Figure 4.13, the vertical asymptote of the Thomeer hyperbola represents the fractional bulk volume occupied by mercury at infinite capillary pressure ($V_{b\infty}$), while the horizontal asymptote represents the displacement pressure ($P_d$). As a result, equation (4.16) can written as:

$$\left(\log \frac{P_c}{P_d}\right)\left(\log \frac{V_b}{V_{b\infty}}\right) = k. \qquad (4.17)$$

Thomeer uses the shape factor $k = \log e^{-G}$. Therefore, by introducing this shape factor and rearranging equation (4.17), one can arrive at the Thomeer hyperbola equation (4.11), namely:

$$\frac{V_b}{V_{b\infty}} = e^{-G/(\log P_c/P_d)},$$

where $G$ is defined as the pore geometrical factor and determines the shape of the hyperbola. (Clerke et al., 2008)
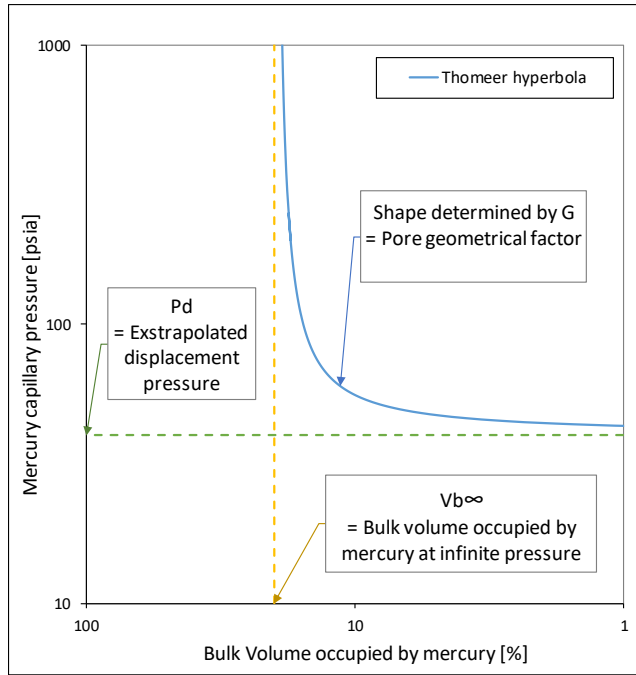
*Figure 4.12: Illustration of Thomeer hyperbola (blue line) in a log-log plot of MICP ($P_c$) against bulk volume occupied by mercury ($V_b$), including definitions of the three Thomeer parameters.*

To create the plot in Figure 4.13, it is necessary to convert the mercury saturation ($S_{Hg}$) to percent bulk volume occupied by mercury ($V_b$). The mercury saturation is defined as

$$S_{Hg} = \frac{V_{Hg}}{V_{Pore}}, \tag{4.18}$$

where $V_{Hg}$ is the volume of mercury intruded while $V_{Pore}$ is the pore volume (PV) of the sample. Bulk volume occupied by mercury ($V_b$) is defined as:

$$V_b = \frac{V_{Hg}}{V_{bulk}}, \tag{4.19}$$

where $V_{bulk}$ is the bulk volume (BV) of the sample. Combining equation (4.18) and (4.19) together with the definition of porosity, leads to the following conversion:

$$V_b = \frac{V_{Hg}}{V_{bulk}} = \frac{V_{pore}}{V_{bulk}} \times \frac{V_{Hg}}{V_{pore}} = \varphi \times S_{Hg}. \tag{4.20}$$

Thus, the conversion is done by multiplying the mercury saturation with the porosity of the sample.

$V_{b\infty}$ and $P_d$ defines the location of the Thomeer hyperbola. In Figure 4.14, the G parameter is kept constant to highlight the effect that change in $V_{b\infty}$ and $P_d$ has on the location of the curve. As mentioned, $V_{b\infty}$ is percent bulk volume occupied by mercury at infinite capillary pressure. This is equal to the total interconnected pore volume (effective porosity) given that mercury is able to fill all the interconnected pores. $P_d$ is controlled by the size of the largest pore-throat, where increasing pore-throat radius leads to a decrease in $P_d$. (Thomeer, 1960)

The value of G is determined by the pore geometry, and, as mentioned, G defines the shape of the hyperbola. In Figure 4.15, the location parameters are kept constant to highlight the effect of changing the G parameter. At one extremity, for very good sorting, the pore-throats will be of almost uniform size; therefore, the mercury will enter almost all pore-throats at the same capillary pressure, and the value of G will be extremely low. The other extremity is that when the sample has very poor sorting, meaning that it has a very wide variety of pore-throat sizes, the shape of the curve will become more linear and the value of G will be very high. (Thomeer, 1960)
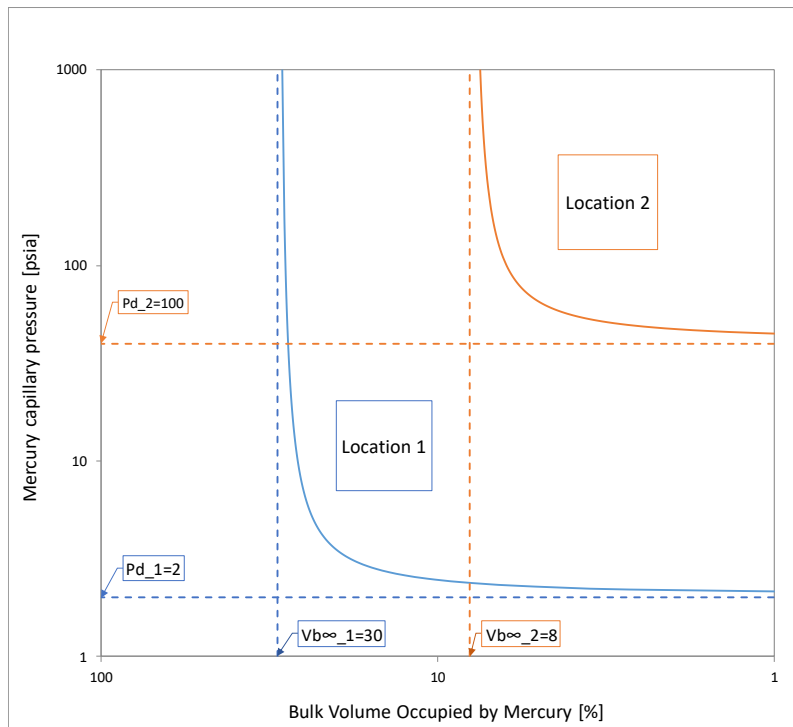
*Figure 4.13: Illustration of the effect of change in $V_{b\infty}$ and $P_d$ on location of the Thomeer hyperbola. The G parameter is kept constant to highlight the effect.*
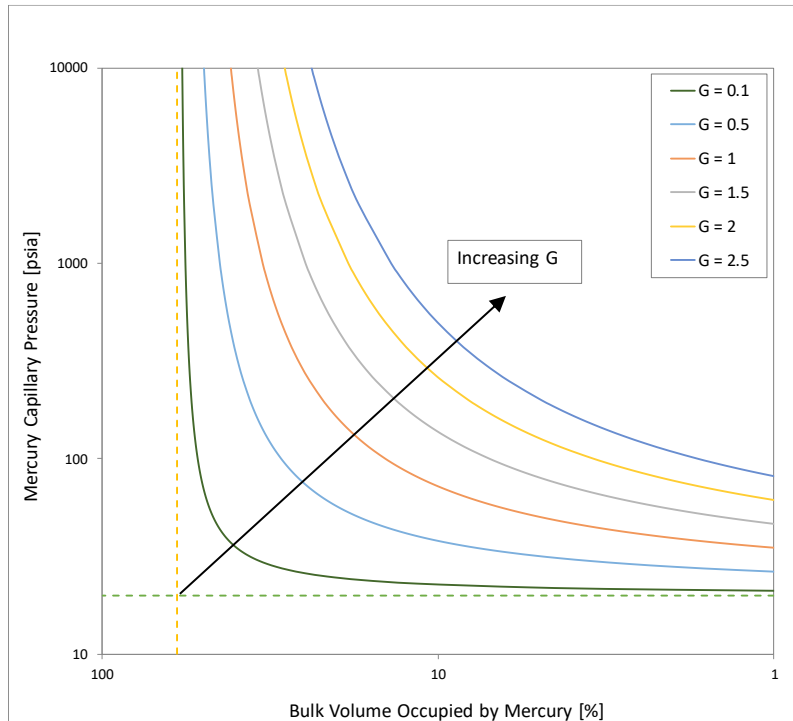


*Figure 4.14: Illustration of the effect of the G parameter on the Thomeer hyperbola. The location parameters are kept constant to highlight the effect. A better degree of sorting leads to a lower G.*

31

Thomeer (1960) also provided a method to fit the capillary pressure curve for multi-modal pore systems: namely, while one pore system is described by one Thomeer hyperbola, Thomeer proposed to simply use a combination of individual hyperbolas. However, he did not explain how to calculate the Thomeer permeability – equation (4.12) – when more than one pore system is present. Clerke et al. (2008) proposed to use the parameter from the first pore system since it mainly controls the permeability. Other investigators has followed their recommendation (Gao, Wu, Chen, Kwak, & Funk, 2011).

Clerke et al. (2008) used Thomeer hyperbolas to curve-match over 500 MICP data to investigate "the basic geological and petrophysical properties of the multimodal pore systems in the Arab D limestone facies in Ghawar field, Saudi Arabia" (p.113). In this study, the Thomeer parameter $P_d$ was found to be the major controlling parameter on permeability among the three Thomeer parameters. Clerke et al. (2008) defined porositons as a "distinct and separable frequency distribution of maximum pore-throat diameters, $P_d$, which has a Gaussian distribution in the $Log(P_d)$ domain, i.e. a mode in the maximum pore-throat diameter space" (p. 115). They also identified the dominant porositons of each sample, resulting in four major porositons. Based on a grouping of these, the pore systems of the Arab D limestones were classified in terms of petrophysical rock types. Then, the authors related these types to geological facies.

Clerke et al. (2008) proposed the use of the following two-term model to predict permeability:

$$\text{Log}\big(k_{predicted}\big) = a + b \times \text{Log}(d_{max}) + c \times \varphi, \qquad\qquad (4.21)$$

where a, b and c are empirical constants, $d_{max}$ is maximum pore-throat diameter (calculated from $P_d$ from the first pore system) in [μm], and $\varphi$ is the porosity in [%]. This resulted in a correlation coefficient ($R^2$) of 89% when related to measured permeability. The two-term model has the potential for well-site implementation when using properly processed well-log data.

Theologou et al. (2015) observed two disadvantages of the Thomeer model. First, the combination of individual Thomeer hyperbolas leads to artificial discontinuities at the merge of the hyperbolas; see Figure 4.16. The discontinuities are a result of the superposition of the hyperbolas and were not present in the authors laboratory data. Second, the model shows a skewness to smaller pore-throats.
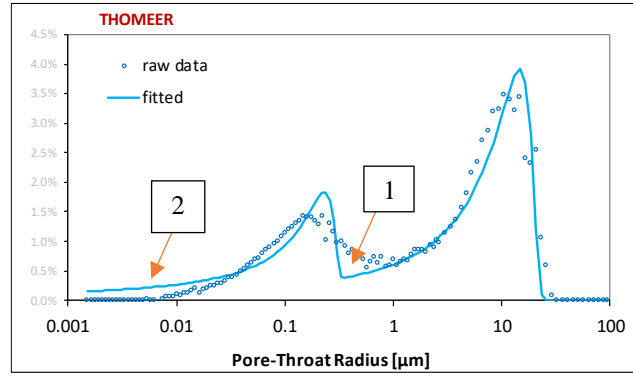


*Figure 4.15: Pore-throat distribution curve-matched with Thomeer hyperbolas. Artificial discontinuity and skewness to smaller pore-throats are highlighthed as 1 and 2, respectivly.*

### 4.4.5.2 Modified Gaussian Error Function

By using a log-normal distribution that provided a better fit with their data, Theologou et al. (2015) developed a model with modified Gaussian error functions instead of Thomeer hyperbolas. They stated that "key features of the proposed Gaussian model form are that it mimics the observed character of many pore-throat systems, the implemented parameters relate to real characteristics of the pore system, and that multiple modes can be superimposed without the creation of discontinuities in the model" (p. 3).

Theologou et al. (2015) provided the following equation for the pore volume displaced for a given capillary pressure, $V_{P_c}$, for pore system i:

$$V_b(i) = \frac{V_{b\infty}(i)}{2}(1 + \text{erf}[x(i)]),\tag{4.22}$$

where the Gaussian error function is included, and defined as

$$\text{erf}[x(i)] = \frac{2}{\sqrt{\pi}} \int_0^{x(i)} e^{-t^2} dt,\tag{4.23}$$

and $x(i)$ is defined as:

$$x(i) = \frac{1}{S(i)} \log \left( \frac{P_c}{P_m(i)} \right). \qquad (4.24)$$

$S$, $P_m$ and $V_{b\infty}$ are the pore system parameters, where $S$ is the shape factor, $P_m$ is the modal pressure and $V_{b\infty}$ is the bulk volume of the pore system. Figure 4.16 illustrates the Gaussian error function given by equation (4.22) in a semi-log plot of MICP against bulk volume occupied by mercury [%].

When more than one pore system is present the total pore volume displaced, $V_{P_T}$, is given by the sum of the contributions from the individual pore systems:

$$V_{P_T} = \sum_{i=1}^{p} V_{P_c}(i), \qquad (4.25)$$

where p is the total number of pore systems present. (Theologou et al., 2015)
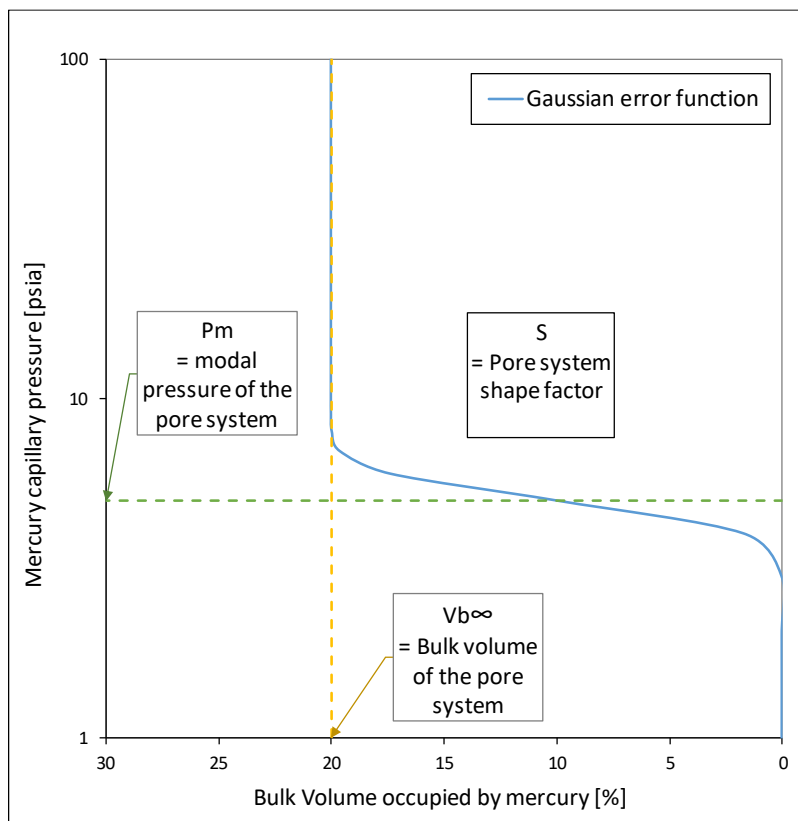


*Figure 4.16: Illustration of the implemented Gaussian error function (blue line) given by equation (4.22) in a semi-log plot of MICP against bulk volume occupied by mercury [%], including definitions of the three Gaussian fitting parameters.*

The value of $S$ is determined by the pore geometry. In Figure 4.17, $P_m$ and $V_{P_\infty}$ are kept constant to highlight the effect that varying the $S$ parameter has on the Gaussian error function for a pore system. Increasing $S$ leads to a steeper slope of the MICP saturation curve and is equivalent to decreasing the degree of sorting. (Theologou et al., 2015)

The value of $P_m$ is related to the pore-throat size of the largest connected pore system. In Figure 4.18, the curve fitting parameters $S$ and $V_{P_\infty}$ are kept constant to highlight the effect of varying $P_m$ on the Gaussian error function for a pore system: namely, increasing $P_m$ leads to upwards vertical displacement of the MICP saturation curve and is equivalent to decreasing pore-throat sizes. (Theologou et al., 2015)

As mentioned, $V_{b\infty}$ is the bulk volume of that pore system. In Figure 4.19, $S$ and $P_m$ are kept constant to highlight the effect that change in $V_{b\infty}$ has on the Gaussian error function for a pore system. An increase in $V_{P_\infty}$ of a pore system is equivalent to an increase in the fraction of total porosity occupied by this pore system. (Theologou et al., 2015)
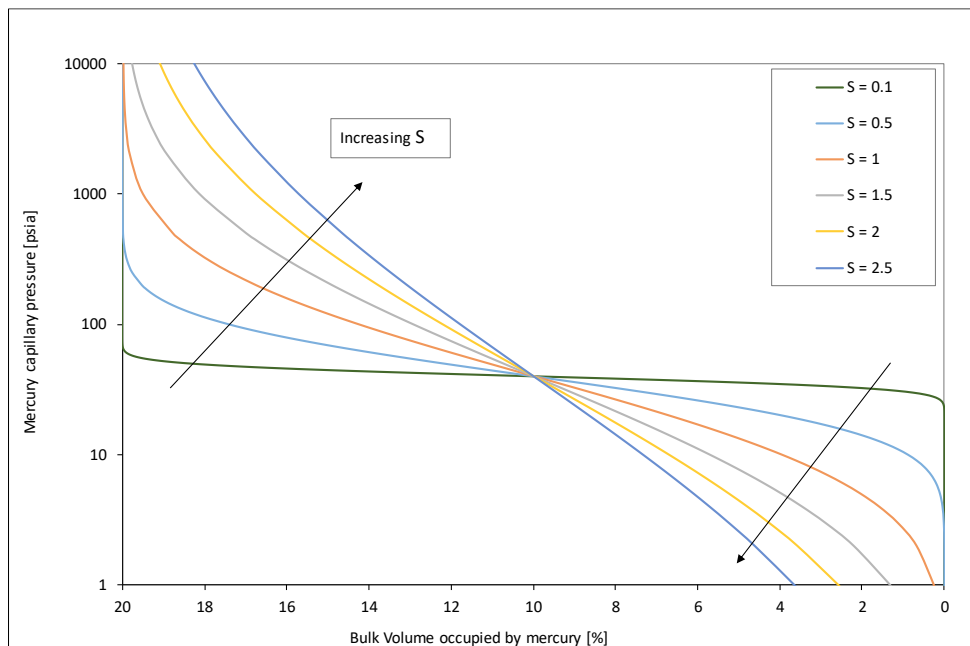


*Figure 4.17: Illustration of the effect of the S parameter on the Gaussian error function for a pore system. The other curve fitting parameters ($P_m$ and $V_{P_\infty}$) are kept constant to highlight the effect. Increasing S leads to a steeper slope of the MICP saturation curve and is equivalent to decreasing the degree of sorting. Inspired by Theologou et al. (2015).*
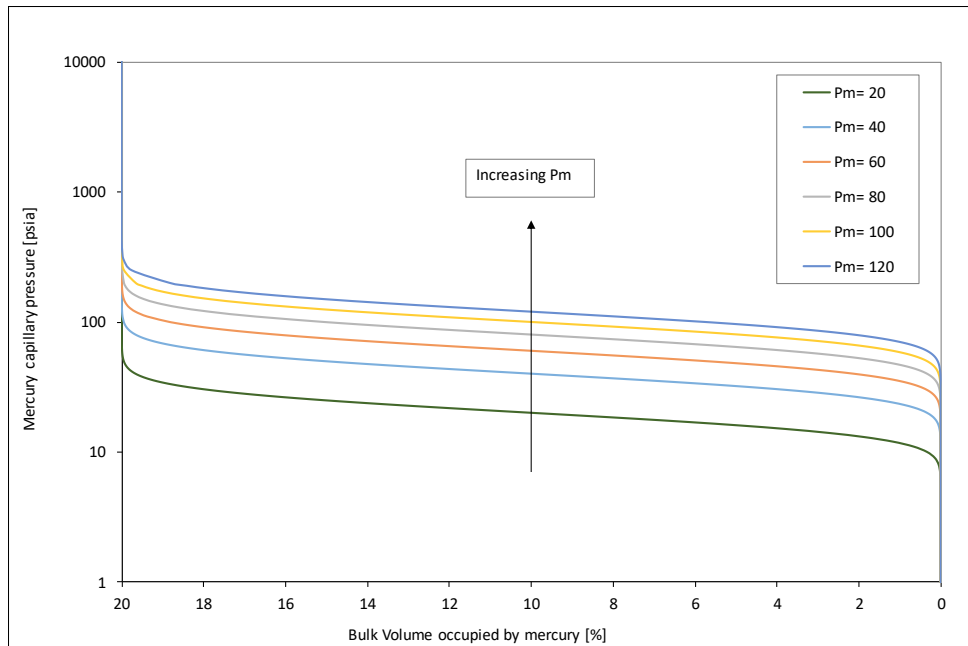
*Figure 4.18: Illustration of the effect of the curve fitting parameter $P_m$ on the Gaussian error function for a pore system. The other curve fitting parameters (S and $V_{P_\infty}$) are kept constant to highlight the effect. Increasing $P_m$ leads to upwards vertical displacement of the MICP saturation curve. Inspired by Theologou et al. (2015).*
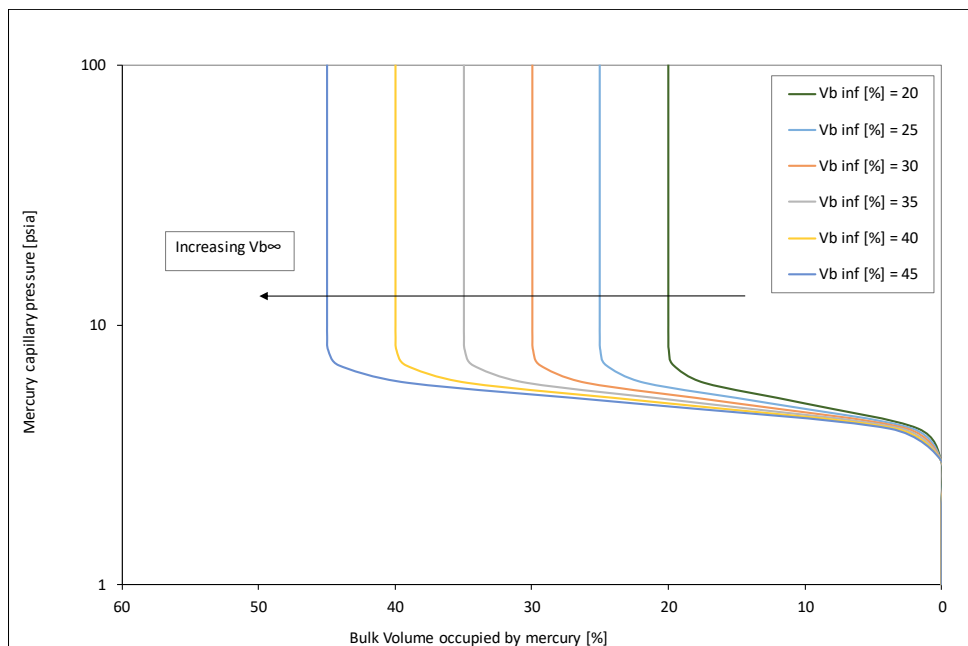


*Figure 4.19: Illustration of the effect of the $V_{b\infty}$ parameter on the Gaussian error function for a pore system. The other curve fitting parameters (S and $P_m$) are kept constant to highlight the effect. Increasing $V_{P_\infty}$ of a pore system leads to horizontal displacement of the MICP saturation curve to the left and is equivalent to increasing fraction of total porosity that is occupied by this pore system. Inspired by Theologou et al. (2015).*

36

Clearly, there are similarities between the proposed Gaussian model and the Thomeer model. $V_{P_\infty}$ is defined equally in both models, and $S$ is comparable with the Thomeer pore geometrical parameter $G$. However, the Gaussian model differs from the Thomeer model by using $P_m$, which depends on the pore-throat size of the largest connected pore volume, instead of the displacement pressure, $P_d$, used in the Thomeer model. (Theologou et al., 2015)

Theologou et al. (2015) used modified Gaussian error functions for the parametrization of 501 MICP samples. They identified MICP-based pore type groups using cluster analysis of the MICP-derived parameters. Then, they extrapolated the pore types from MICP samples to CCA samples, and finally, they extrapolated to the log domain.

## 4.5 Porosity-Permeability Models

To obtain effective reservoir descriptions, it is critical to have strong knowledge about permeability and the permeability distribution. This is usually determined from core data, but since there are often uncored intervals and wells, it is important to have good prediction methods to estimate this information. Two typical porosity-permeability relationships used to estimate permeability from log-derived porosity are described below. (Amaefule et al., 1993)

### 4.5.1 Classical Porosity-Permeability Relationship

The classical empirical porosity-permeability relationship used to estimate permeability from log-derived porosity is given by

$$\log k = a\varphi + b,$$

where $k$ is the estimated permeability, $\varphi$ is log-derived porosity, and a and b are empirical constants. Since permeability appears to be log-normally distributed, the cross plot of permeability against porosity is plotted in semi-log space; hence, $\log k$ is used.

### 4.5.2 Hydraulic Units

To improve existing reservoir description techniques Amaefule et al. (1993) proposed to base rock typing on flow units. They developed a technique to identify and characterize units with similar pore-throat geometrical attributes, called hydraulic units, from core and log data. Among others, they did this to improve permeability predictions in uncored intervals or wells.

Amaefule et al. (1993) based their technique on a modified Kozeny-Carman equation. A generalized form of the Kozeny-Carman relationship is given as

$$k = \frac{\varphi_e^3}{(1-\varphi_e)^2} \frac{1}{F_s \tau^2 S_{gv}^2}, \tag{4.26}$$

where $F_s \tau^2$ is known as the Kozeny constant. According to Amaefule et al. (1993), the Kozeny constant is only constant within a hydraulic unit, whereas it varies between different units. They focused their studies on solving the issue of a variable Kozeny constant. They

addressed this by dividing both sides of equation (4.26) by porosity ($\varphi_e$) and taking the square root of both sides. This results in the following:

$$\sqrt{\frac{k}{\varphi_e}} = \left[\frac{\varphi_e}{1-\varphi_e}\right]\left[\frac{1}{\sqrt{F_s}\tau S_{gv}}\right]. \tag{4.27}$$

Furthermore, they introduced the three variables; $RQI$, $\varphi_z$, and $FZI$. $RQI$ is defined as the Reservoir Quality Index and is given by the following equation:

$$RQI = 0.0314\sqrt{\frac{k}{\varphi_e}}, \tag{4.28}$$

where the constant 0.0314 is included to account for $RQI$ measured in [μm] and $k$ in [mD]. $\varphi_z$ is the pore volume to grain volume ratio, given by

$$\varphi_z = \frac{\varphi_e}{1-\varphi_e}, \tag{4.29}$$

and $FZI$ is the Flow Zone Indicator and is given by

$$FZI = \frac{1}{\sqrt{F_s}\tau S_{gv}} = \frac{RQI}{\varphi_z}. \tag{4.30}$$

Including these three variables into equation (4.27) and taking the logarithm of both sides gives:

$$\log RQI = \log \varphi_z + \log FZI. \tag{4.31}$$

Clearly, when $RQI$ is plotted against $\varphi_z$ on a log-log scale, equation (4.31) yields a straight line with a unit slope. Then, on the same plot, $FZI$ can be found from the intersection between the graph and $\varphi_z = 1$; see Figure 4.20. Different FZI values will yield parallel lines, where samples that lie on the same line constitute a hydraulic unit, having similar pore-throat attributes.
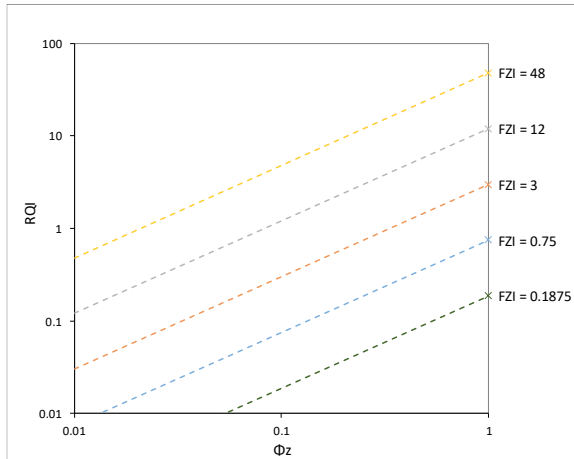
*Figure 4.20: Graph of RQI plotted against $\varphi_z$ in log-log space. FZI can be found from the intersection between the graph and $\varphi_z = 1$.*
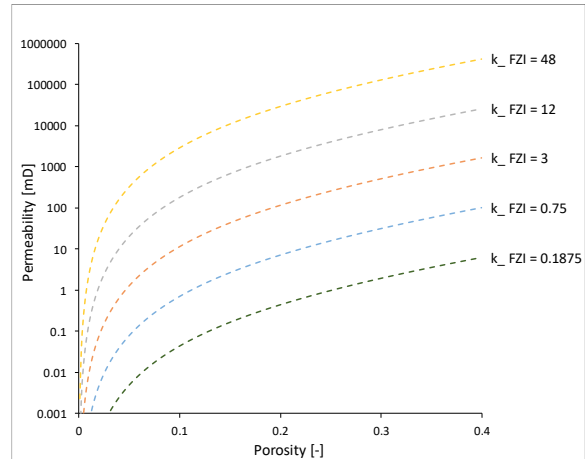
*Figure 4.21: FZI lines in semi-log plot of permeability against porosity.*

Equation (4.31) can also be rearranged to solve for permeability. This results in the following:

$$k = 1014(FZI)^2 \left[ \frac{\varphi_e^3}{(1-\varphi_e)^2} \right], \tag{4.32}$$

where k is in [mD], FZI is in [μm] and $\varphi_e$ as fraction. Figure 4.21 illustrates FZI lines in a graph of permeability against porosity. (Amaefule et al., 1993)

# 5 Workflow for Parametrization of MICP Curves

To perform the parameterization of the MICP curves, a spreadsheet developed by Lundin Norway AS was used. In addition, to be able to perform both Thomeer and modified Gaussian analysis, a QC of the laboratory data was incorporated in the workflow. This was done to ensure that only high-quality MICP data was included in the rock/pore typing procedure. The following workflow was followed for one sample at a time: QC of the raw laboratory data, closure correction, pore system collection, and, finally, the MICP curve matching procedure.

## 5.1 Quality Control of Laboratory Data

The first step when starting the analysis of a new rock sample is to QC the laboratory data. This is done to ensure that only high-quality MICP data is included in the rock/pore typing procedure. Each sample is left with a QC flag of 1, 2, or 3, as well as comments on observations from the sample picture and data when necessary. QC flag 1 corresponds to there being no specific errors/problems with the data, QC flag 2 means that there are uncertainties regarding the data, and QC flag 3 means that the MICP data should be rejected. Detailed descriptions of the QC flags are listed in Table 5.1, and some are elaborated below.

The first point to consider during QC is the sample size; larger samples are usually preferred. As mentioned, smaller samples with irregular surfaces are more prone to closure effects and may not be representative, among other issues. Hence, very small samples are given QC flag 2, if they are not rejected.

The next QC step is to examine the difference between the helium (He) porosity measured by CCA and the MICP porosity. The MICP porosity should reflect the CCA porosity for the MICP data to be representative. A tolerable deviation of 20% is used:

$$\left| \frac{\varphi_{He} - \varphi_{MICP}}{\varphi_{He}} \right| \cdot 100\% < 20\%. \qquad (5.1)$$

If the difference is larger, the sample is given QC flag 3 and is rejected from the study. Next QC examines, look at the difference in the permeability measurements between the Klingenberg corrected gas permeability from CCA ($k_l$) and the Swanson permeability from

MICP ($k_{swanson}$). $k_{swanson}$ should reflect $k_l$ for the MICP data to be representative. The tolerable difference is set to a factor of 10:

$$0.1 < \frac{k_{swanson}}{k_l} < 10. \hspace{3cm} (5.2)$$

If the deviation is larger, the sample obtains QC flag 3 and is thus rejected from the study.

Next, QC of the sample photo is performed, if present. During this step, it is especially important to pay close attention to the outer surface of the sample to have an idea about the degree of closure correction needed. As mentioned, irregular surfaces may result in high closure correction. However, when the permeability of the sample is relatively high, it may have some large pores that will reduce the closure correction. If the sample photo is not included in the report, core photos together with lithological descriptions from CCA are used as an alternative.

*Table 5.1: Description of how a QC flag is selected for a sample.*

| QC flag | Description of QC flag | Details |
|---|---|---|
| 1 | No specific errors/problems with the data | • Data OK |
| 2 | Uncertainties regarding MICP data | • Very small sample<br>• Possible but difficult to match (low confidence in fitting parameters) |
| 3 | Rejection of MICP data | • Noisy data (the points should define a smooth shape)<br>• Suspicious closure results (especially for tight samples)<br>• Difference between He-porosity and MICP porosity is large (> 20% in homogeneous sample)<br>• Unrealistic Thomeer fitting parameters (G > 2, $\Sigma V_{b_\infty,1+2+3}$ >> actual volume injected)<br>• Significant difference in permeability between CCA Kl-permeability and MICP Swanson permeability (> factor of 10) |

## 5.2 Closure Correction

Then the closure correction is determined to account for irregularities in the sample surface. Several approaches exist to determine the closure correction needed for MICP data, like the intercept method and EOG method. In analyses associated with this thesis, the intercept method is mainly used for the closure corrections.

The intercept method uses a closure correction chart, which is a semi-log plot of MICP against uncorrected (raw) bulk volume occupied by mercury [%]; see Figure 5.1. The closure correction is selected as the intersection of two tangents. The first tangent is defined at the steep slope at the beginning of the capillary pressure curve, using a closure value. In contrast, the second tangent is placed at the plateau of the capillary pressure curve, which is where it first starts to stabilize, resulting from the first pore system entered. This tangent is defined by a seat value. The intersection of these two tangent lines is the closure correction, shown in Figure 5.1.
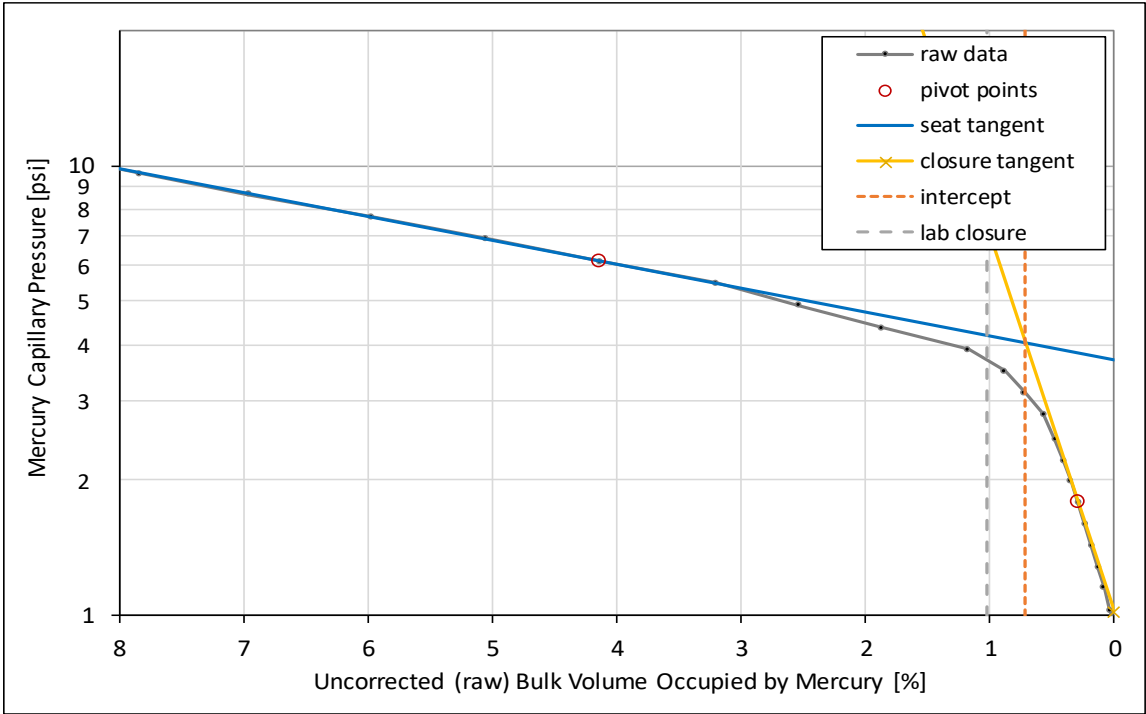


*Figure 5.1: Closure correction chart: a semi-log plot MICP [psi] plotted against uncorrected (raw) bulk volume occupied by mercury [%]. The closure correction is determined by the intersection of two tangent lines to the curve: the closure tangent and the seat tangent.*

The intercept method is chosen because it reduces subjectivity related to the determination of closure correction, and thus decreases the bias related to the interpreter. Furthermore, it is a

relatively simple method. As an additional QC of the closure correction from the intercept method, this closure correction is compared to the closure correction determined by the laboratory. However, there are not always well-defined seat and closure tangents, especially for low-permeability samples. In these cases, the closure value from the laboratory is tested and corrected if needed, resulting in higher subjectivity.

Bailey (2009) observed that the closure-corrected MICP-derived porosity for samples with low permeability, specifically shales, was often significantly lower than porosity derived from other methods, such as He-porosity. According to him, this is a consequence of pore volume (PV) compressibility prior to mercury entering the largest pore-throats. This statement is based on observations that a log-log plot of PV compressibility against MICP results in a straight line with a negative slope until actual intrusion begins. This leads to three places where the injected mercury could go, namely the closure, the compressibility, and the actual intrusion. Bailey (2009) then proposed a modified closure correction approach that accounts for this PV compressibility, called the EOG method.

In this workflow, the EOG method is implemented in the spreadsheet (Figure 5.2), but it is mainly used as QC of the closure correction obtained using the intercept method, or the closure correction stated by the laboratory. This is done to evaluate whether the PV compressibility will cause significant error if not accounted for, especially for tight (i.e. low-permeability and low-PV) samples.

Samples with suspicious closure results obtain QC flag 3 and are rejected, as shown in Table 5.1.
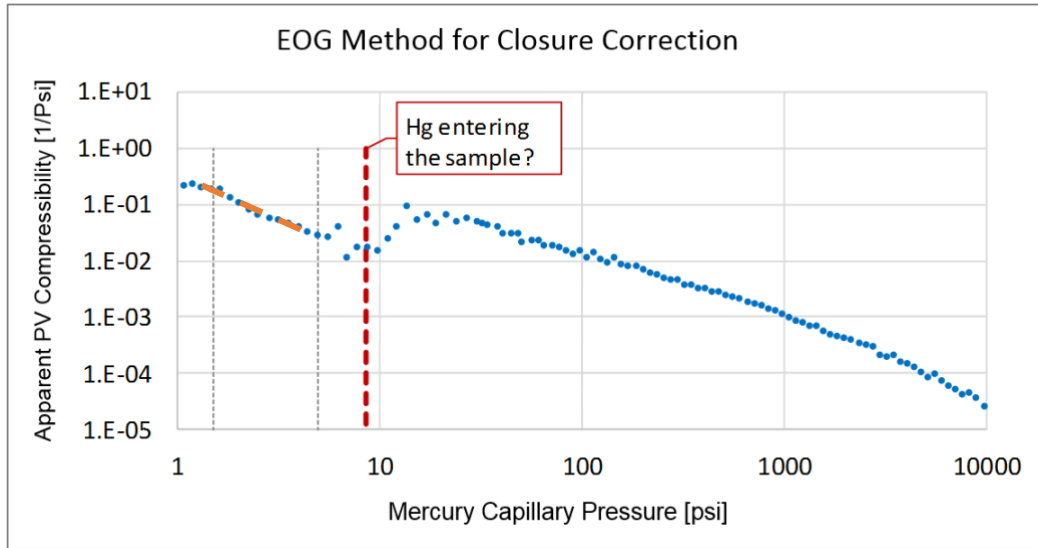
*Figure 5.2: Illustration of EOG plot used for QC of closure correction and to evaluate wheter PV compressibility will cause significant error if not accounted for.*

## 5.3 Pore Systems Selection

The next step in the framework is to select the pore systems from the MICP data. The pore system intervals are determined from the MICP curve in a semi-log plot of MICP against bulk volume occupied by mercury [%], as shown in Figure 5.3. Pore systems are identified as arches in the curve. The number of pore systems can also be identified by examining the histogram of the pore-throat size distribution (Figure 5.4). Each pore system is defined by an interval limited by the maximum and minimum value of bulk volume occupied by mercury. In the procedure used in this spreadsheet, a maximum of three pore systems can be selected. This can be justified by the fact that pore systems above the maximum HC column height will be water filled, and the largest pore systems are the most essential for permeability.
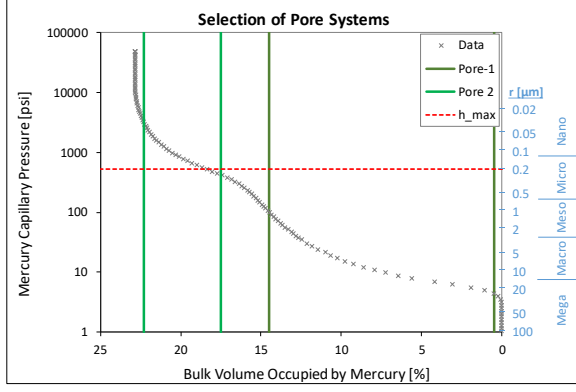
*Figure 5.3: Selection of pore systems from MICP plotted against bulk volume occupied by mercury [%]. Solid lines represent pore system intervals, while the dashed line represents maximum HC column height.*
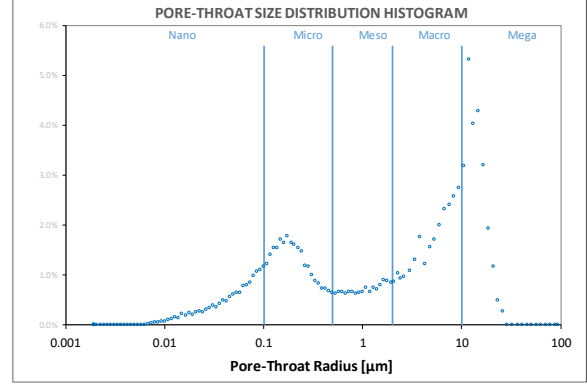


*Figure 5.4: Pore systems can also be identified from the pore-throat size distribution histogram.*

### 5.3.1 Maximum HC Column Height

The maximum HC column height ($h_{max}$) is included in the semi-log plot of MICP against bulk volume occupied by mercury [%], as a tool to evaluate which pore systems are most important. The pore systems above the maximum HC column height will be less relevant for analyses since they are mainly water filled and contribute little to flow. The height is indicated by a red dashed line in Figure 5.5, and it is approximated from the field of interest, here Edvard Grieg.

The oil-water capillary pressure, $P_{cow}$, that corresponds to the maximum HC column height can be calculated using equation (4.6) with oil as the non-wetting phase and water as the wetting phase:

$$P_{cow} = C(\rho_w - \rho_o)gh = 0.145(\rho_w - \rho_o)gh, \qquad (5.3)$$

where $C = 0.145$ is the correction factor needed to obtain $P_{cow}$ in [psi] when $\rho$ is in [g/cm$^3$], $g$ in [m/s$^2$], and h in [m]. To apply this to the MICP plot, it needs to be converted to mercury-air capillary pressure as described in Section 4.2.1, by rearranging equation (4.9) in combination with the values listed in Table 4.2. This results in the following:

$$P_{cma} = P_{cow} \frac{\sigma_{ma} \cos\theta_{ma}}{\sigma_{ow} \cos\theta_{ow}} = P_{cow} \frac{312}{28} = 1.616(\rho_w - \rho_o)gh. \quad (5.4)$$

The densities and maximum HC column height values used in this thesis are listed in Table 5.2.
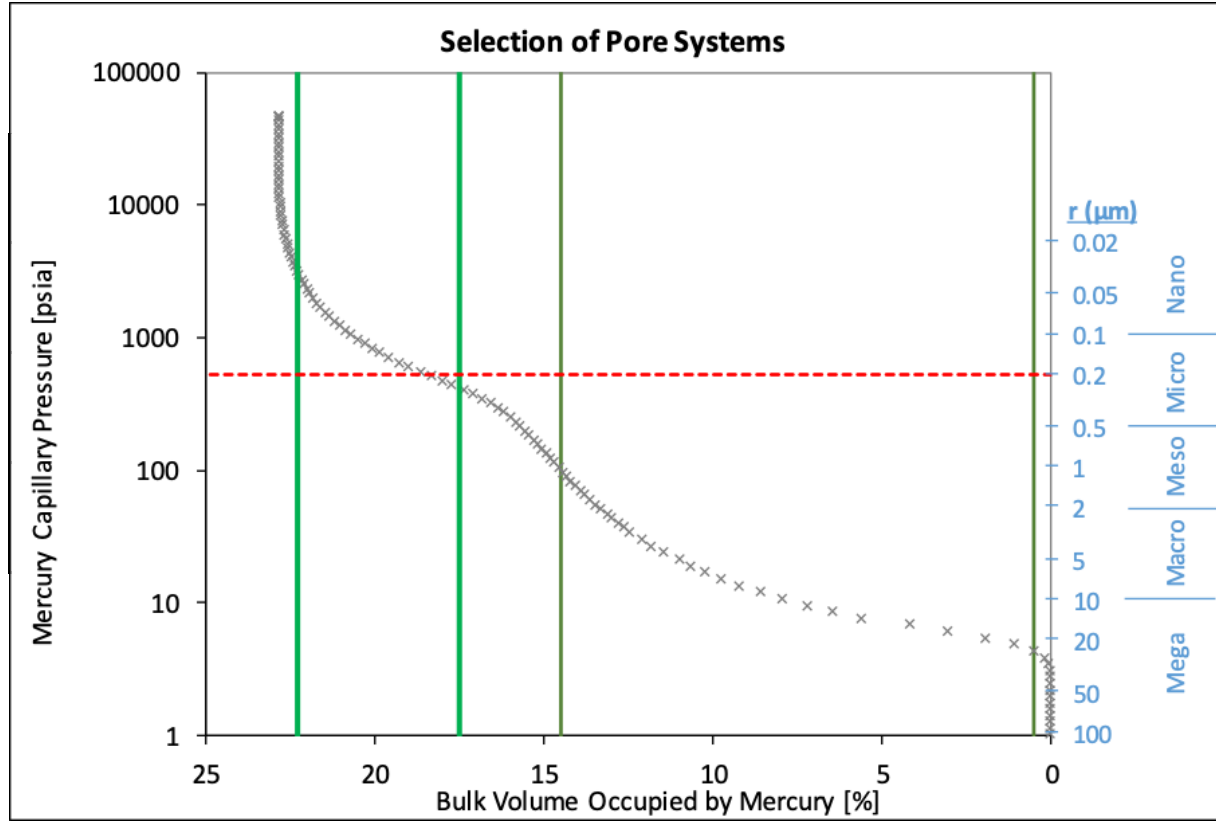


*Figure 5.5: MICP plotted against bulk volume occupied by mercury. The red dashed line represents the maximum HC column height converted to MICP. It indicates that for this sample, mainly the first pore system will be relevant.*

### 5.3.2  Histogram of Pore-Throat Size Distribution

The pore-throat size distribution, illustrated in Figure 5.6, is obtained from MICP data. First, pore-throat sizes are estimated using equation (4.8) in combination with the values listed in Table 4.2. The pore-throat radius from the mercury-air system becomes

$$r = C\frac{2\sigma\cos\theta}{P_c} = 0.145038\frac{2\sigma\cos\theta}{P_c} = \frac{90.4318}{P_c}, \tag{5.5}$$

where $C = 0.145038$ is the correction factor needed to obtain the radius in [μm], when $P_c$ is in [psi] and $\sigma$ in [dynes/cm]. Then, the logarithm of the pore-throat sizes ($\log r$) is calculated.

This is done because pore-throats are highly variable in size, ranging over several orders of magnitude, so their sizes are characterized on a logarithmic scale. Next, the pore-throat size distribution ($PSD$) can be determined by deriving the fractional PV injected ($v$) with respect to $\log r$:

$$PSD = \frac{dv}{d(\log r)}. \tag{5.6}$$

The following approximation for the derivative is used:

$$PSD_i \approx \left| \frac{v_{i+1} - v_i}{\log r_{i+1} - \log r_i} \right|, \tag{5.7}$$

which can be normalized by using

$$PSD = \frac{PSD_i}{\sum PSD_i}. \tag{5.8}$$

Finally, the histogram of pore-throat size distribution is obtained by plotting PSD against $\log r$ in a semi-log plot, as shown in Figure 5.6. The definitions of the pore-throat sizes are listed in Table 5.3.
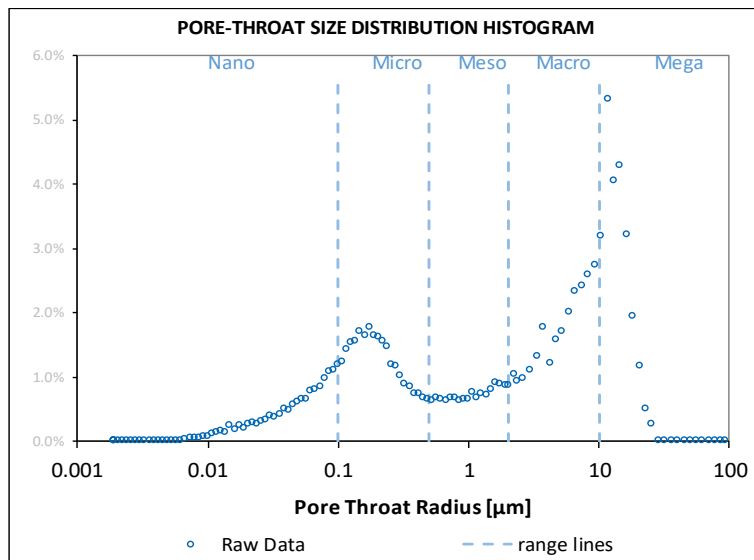


*Figure 5.6: Histogram of pore-throat size distribution, obtained by plotting PSD against pore-throat radius (r) on a semi-log plot.*

*Table 5.3: Definitions of the Pore-throat sizes*

| Pore-throat size | r [µm] |
|---|---|
| Mega | >10 |
| Macro | 2–10 |
| Meso | 0.5–2 |
| Micro | 0.1–0.5 |
| Nano | <0.1 |

## 5.4 MICP Curve Fitting Algorithms

After the pore system intervals are determined, the curve fitting procedure can begin. The following MICP curve fitting algorithms are used in this study: Thomeer hyperbolas and modified Gaussian error function. The procedures are described below.

### 5.4.1 Thomeer Hyperbolas

First, the MICP curve fitting procedure with Thomeer hyperbolas is performed. Starting with the first pore system (i.e. the pore system with the largest pore-throats), an initial estimate of the Thomeer parameters ($V_{b\infty}$, $P_d$, and $G$) is made based on the selected pore system. Then, the Solver module in Excel is used to find the best fit between the Thomeer fitting curve and the data points (further details in Section 5.4.1.1). The objective of the Solver is set to the solution cell and the Thomeer parameters as variable cells: $V_{b\infty}$, $P_d$, and $G$ (Figure 5.7). It may be useful to include a constraint in the solver that $G \leq 2$, to avoid unrealistic solutions. After Excel Solver has found a match, as in Figure 5.8, the histogram of pore-throat size distribution is studied to evaluate that match (Figure 5.9). Next, the Thomeer permeability is calculated based on the fitted parameters from the first pore system using equation (4.12), and it is compared to the Klinkenberg corrected permeability from CCA, if available, for QC. The procedure is subsequently repeated for pore systems 2 and 3, if present. Samples with unrealistic Thomeer parameters are given QC flag 3 and rejected; see Table 5.1.
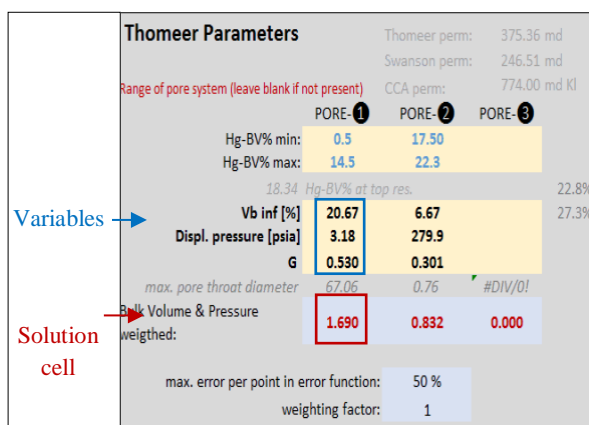


*Figure 5.7: Illustration of the objective of the Solver, which is to minimize the bulk volume and pressure weighting by changing the Thomeer variables.*
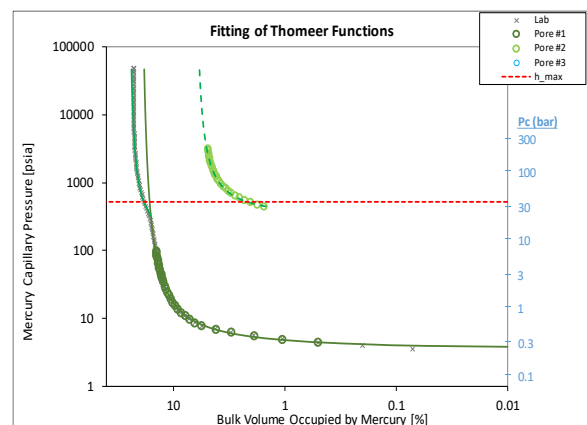
*Figure 5.8: An example of a good match obtained using Thomeer hyperbolas and the Excel Solver tool for a bimodal pore system.*
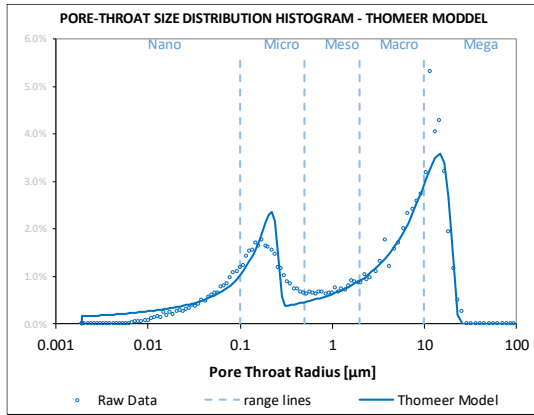
*Figure 5.9: Once Excel Solver has found a match between the Thomeer fitting curve and the data points, the quality of the match is evaluated in the histogram of pore-throat sizes.*

Attempts have been made to develop software-supported analysis of MICP curves with Thomeer hyperbola functions. For example, Göppert (2016) developed software to address drawbacks from previous programs, namely complex pore geometry, raw data corrections, and a continuous work flow. Since it is not necessary to go through samples one at a time using Göppert's software, analysis speed is increased. However, this also affects the quality of the analysis, mainly the QC associated with going through one sample at a time, such as QC for the core photo and the visualization of the closure correction. As a result, analyses associated with this thesis are conducted sample-by-sample with QC and the Excel Solver module for curve matching, as described above.

### 5.4.1.1 Best Fit Procedure

The quality of the curve fitting of the MICP curve with Thomeer functions is evaluated for each pore system using Pearson's (1900) chi-squared goodness-of-fit test. The Pearson's chi-squared test for the capillary pressures is given by the following equation:

$$\chi^2 = \sum_{i=1}^{n} \left( \frac{P_{c,calc,i} - P_{c,i}}{P_{c,i}} \right)^2,$$  (5.9)

where $P_{c,calc,i}$ is calculated by rearranging equation (4.11):

$$P_{c,calc,i} = P_d \times 10^{-G/(\ln V_{b,i}/V_{b\infty})}.$$  (5.10)

In addition, to reduce the effect of extreme values, a maximum error threshold value of 50% is used. If $\chi^2$ exceeds this value, it is clipped to 50%.

Similarly, for the fractional bulk volume,

$$\chi^2 = \sum_{i=1}^{n} \left( \frac{V_{b,calc,i} - V_{b,i}}{V_{b,i}} \right)^2, \tag{5.11}$$

where $V_{b,calc,i}$ is calculated by rearranging equation (4.11):

$$V_{b,calc,i} = V_{b\infty} \times e^{-G/(\log P_{c,i}/P_d)}. \tag{5.12}$$

The same maximum error threshold concept as above applies.

To obtain the best possible match between the Thomeer hyperbola for a given pore system and the MICP curve, a weighted combination method is used. This weighted combination is given by:

$$\chi^2 = \frac{1}{2} \sum_{i=1}^{n} \left[ \left( \frac{P_{c,calc,i} - P_{c,i}}{P_{c,i}} \right)^2 \times i^w + \left( \frac{V_{b,calc,i} - V_{b,i}}{V_{b,i}} \right)^2 \times [(n+1) - i]^w \right], \tag{5.13}$$

where $n$ is the total number of measurements for the given pore interval, and $w$ is the weighting factor ($w = 1$, is used in this study). The objective of the Excel Solver tool is set to minimize $\chi^2$ with the Thomeer parameters as the variables. The solution is used as the best fit.

## 5.4.2 Modified Gaussian Error Function

The procedure for curve fitting with the modified Gaussian error function is similar to the Thomeer function. Starting with the first pore system, an initial guess is made of the error function variables, $V_{b\infty}$, $P_m$, and $S$. Excel Solver is used to find the best fit by minimizing the error cell by changing the variables (described in Section 5.4.2.1). Next, the histogram of the pore-throat size distribution is



*Figure 5.10: Result of curve fitting with the Gaussian error function in the histogram of pore-throat distributions.*

studied to determine whether it is a good match (Figure 5.10). The procedure is then repeated for pore systems 2 and 3, if present.
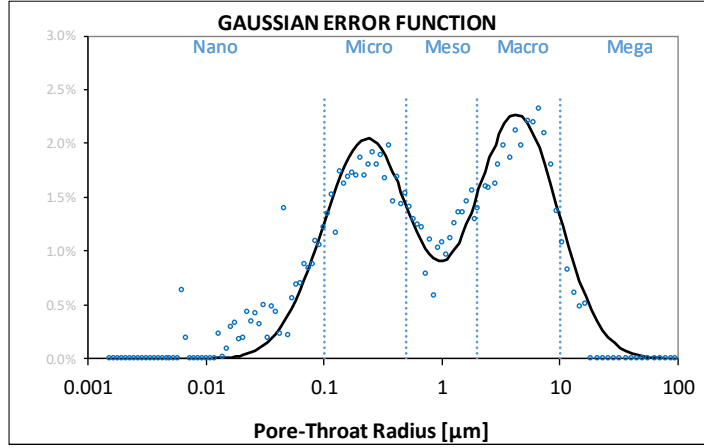
The QC process in this workflow is mainly based on Thomeer analysis, so the QC flag is unaffected by the Gaussian analysis results.

### 5.4.2.1 Best Fit Procedure

To obtain the best possible match between the modified Gaussian error functions given by equation (4.22) and the MICP curve, the Pearson (1900) chi-squared test for fractional bulk volume is used. This is given by:

$$\chi^2 = \sum_{i=1}^{n} \left( \frac{V_{b,calc,i} - V_{b,i}}{V_{b,i}} \right)^2, \tag{5.14}$$

where $V_{b,calc,i}$ is calculated from equation (4.22). In addition, to reduce the effect of extreme values, a maximum error threshold value of 50% is used. If $\chi^2$ exceeds this value, it is clipped to 50%. Then, the best fit used is the solution obtained by setting the Excel Solver objective to minimize $\chi^2$ by using the Gaussian parameters as the variables.

# 6 Results and Discussion

For the study associated with this thesis, data from the Edvard Grieg field was used. First an introduction to databases developed during this study is provided. Followed by an introduction to the main facies. Next QC of the database are performed. Followed by the results from MICP analyses and finally, rock/pore typing attempts.

## 6.1 Data Description

### 6.1.1 Database intro

Three databases were developed during the study associated with this thesis, consisting of rock samples retrieved from nine cored wells in Edvard Grieg field. These are presented below.

The first database is a CCA database. It consists of data from 3711 CCA samples. The database is developed with purpose of comparison and QC of MICP samples.

The second database is a MICP database without QC filter. It consists of data from 273 MICP samples without QC. The database is developed with purpose of comparison and QC of MICP sampling database.

The third and main database is a MICP database after QC filter. After careful QC only 168 of the original 273 MICP samples was accepted to the QC filtered database for further rock/pore typing analyses. The rejection of samples is due to QC flag 3 caused by low quality MICP data or unrealistic Thomeer parameters.

As previously stated, MICP data from samples consisting on lager pieces of CCA plugs is preferred. Ideally only these samples should be included in the main database for further rock/pore typing analyses. The majority of the MICP samples on Edvard Grieg are end-trims or chips. To obtain sufficient data for statistical analyses, it was decided to accept these MICP samples. The included samples are accepted after careful QC and thus the uncertainty linked to sample size should have been minimized. Still, there will be some uncertainty related to sample size.

### 6.1.2 Facies intro

The rock samples (both CCA and MICP) were assigned facies from the facies log using depth shifted sample depth. 151 of the 168 QC filtered MICP samples identifies as four facies. Thus, the main focus was given to these facies. The facies are called Aeolian, Fluvial Aeol Rework, Alluvial Sand Matrix, and Alluvial Silty Matrix. These are described in Table 6.1.

*Table 6.1: Description of the four main facies.*

| Facies | Abbreviation in plots | Description | Facies color in plots |
|---|---|---|---|
| Aeolian | Aeol | Aeolian sandstone with better reservoir quality | |
| Fluvial Aeol Rework | FluvAeolRew | Aeolian sandstone with poorer reservoir quality | |
| Alluvial Sand Matrix | AlluSdMx | Alluvial fan conglomerates with matrix of better reservoir quality | |
| Alluvial Silty Matrix | AlluSltMx | Alluvial fan conglomerates with matrix of poorer reservoir quality | |

## 6.2 Quality Control of MICP Dataset

After the databases was developed, QC of the MICP dataset was performed. The aim was to investigate the representativeness of the MICP dataset, because a sufficient and representative MICP dataset is essential for successful rock/pore typing.

In Figure 6.1a, a cross plot of permeability and porosity of all the CCA samples was made. Data points are colored by facies and the lines are FZI-lines. Note that there is a very high scatter in the data, also within the facies. The data from each facie is spread across several FZI-lines; hence, the FZI plot is not optimal for rock typing. As a result, finding other or additional ways to establish improved porosity-permeability relations from MICP data may have great potential. Note that there is a tendency that Aeolian samples dominates at higher permeability, followed by Fluvial Aeol Rework, Alluvial Sand Matrix and Alluvial Silty Matrix from higher to lower permeability, respectively.

In Figure 6.1, scatter plots of the permeability and porosity measured of all the samples measured by CCA were made. There are three plots, one for each database. The colors of the data points represent facies. Note that there is a much higher scatter in the data from the CCA database compared to the MICP databases. Also note that there are very few MICP samples at low porosity and permeability, especially for the MICP samples after QC filter.
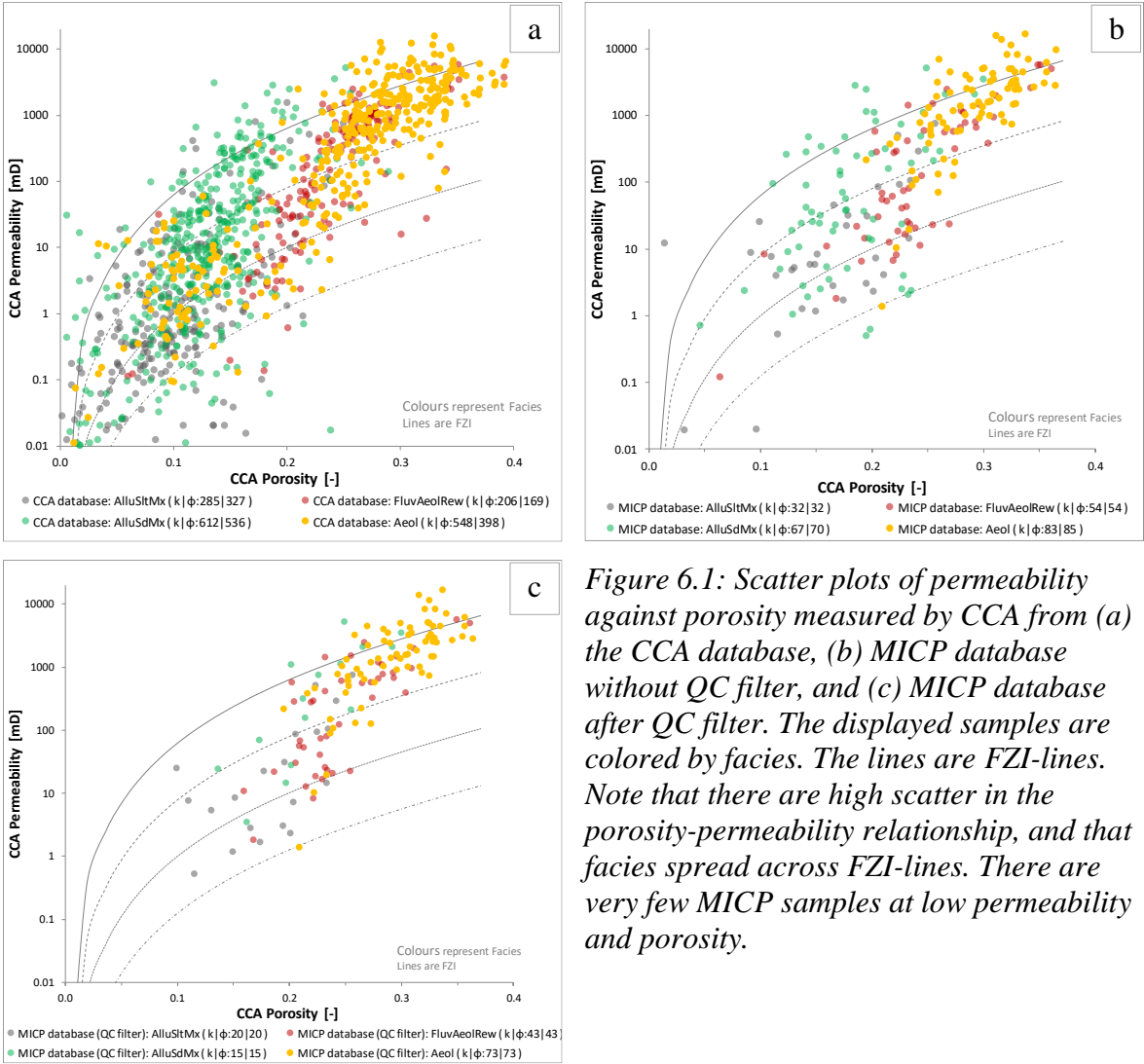


Figure 6.1: Scatter plots of permeability against porosity measured by CCA from (a) the CCA database, (b) MICP database without QC filter, and (c) MICP database after QC filter. The displayed samples are colored by facies. The lines are FZI-lines. Note that there are high scatter in the porosity-permeability relationship, and that facies spread across FZI-lines. There are very few MICP samples at low permeability and porosity.

To be representative, the porosity-permeability distribution from the MICP samples should reflect the heterogeneity of the distribution from the CCA samples. The few samples in the low porosity-permeability region shows that this region is underrepresented in the MICP databases, and hence suggest biased MICP sampling towards best-quality rocks, which might lead to bias in the results, so it should be further investigated.

In Figure 6.2 and Figure 6.3, plots of the porosity and permeability measured by CCA data are displayed, respectively. Three plots are made in each figure, one for each database. The boxes represent the 25th and 75th percentile (P25 and P75), while the line in the box represents the median (P50). The outgoing lines, called whiskers, represents the maximum or minimum values that does not exceed a distance of 1.5 times the interquartile range (IQR). IQR is the range between the 25th and 75th percentile. The boxes are colored by facies.
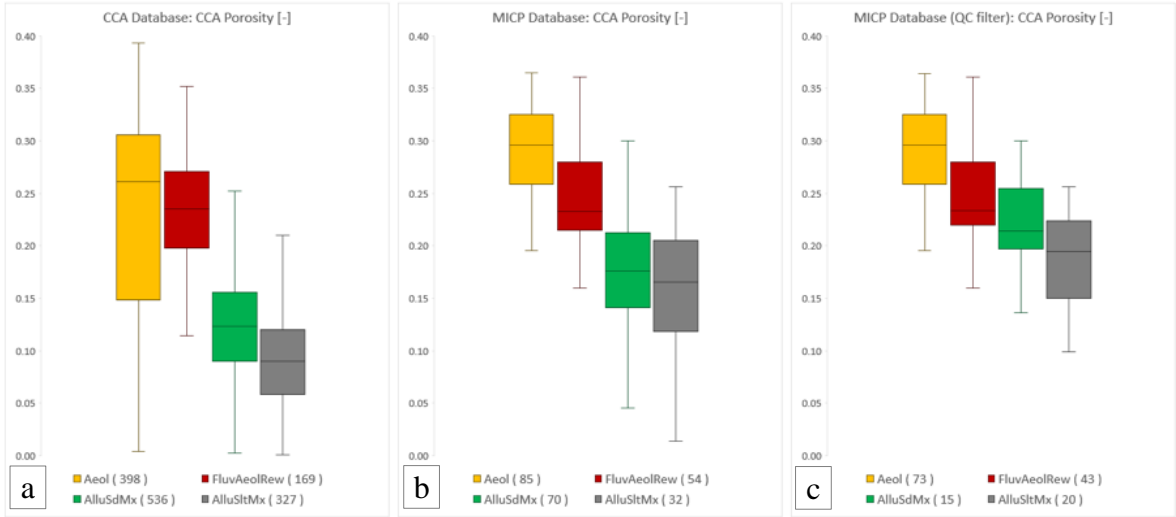


*Figure 6.2: Box plots of porosity measured by CCA from (a) CCA database, (b) MICP database and (c) QC filtered MICP database, colored by facies.*
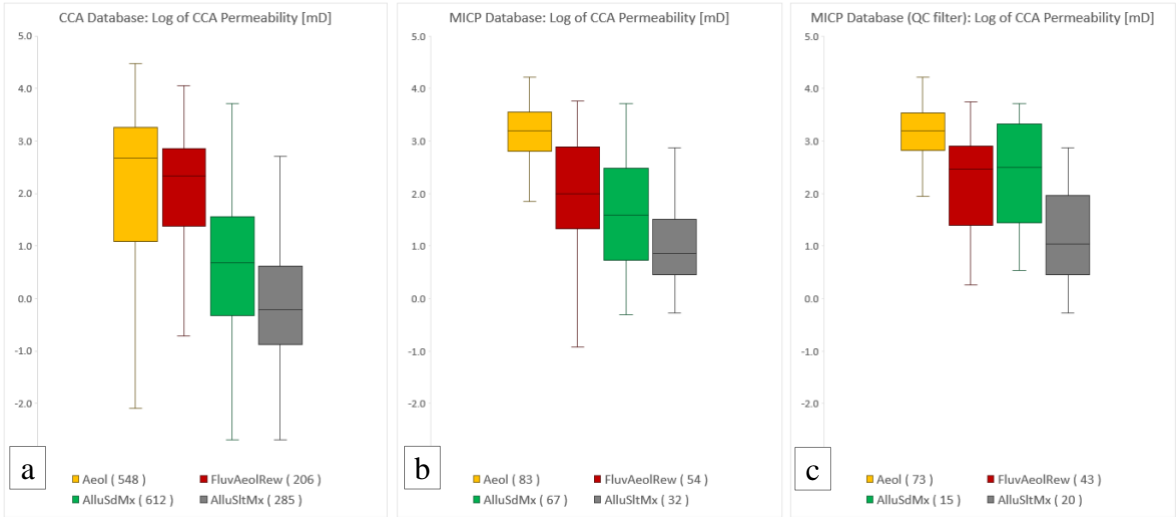


*Figure 6.3: Box plots of permeability measured by CCA from (a) CCA database, (b) MICP database and (c) QC filtered MICP database, colored by facies.*

These plots (Figure 6.2 and Figure 6.3) was used to further investigate how the representativeness of the MICP dataset was affected by few MICP samples at low porosity and permeability. Note that the P50 values are generally higher for both porosity and permeability in the MICP samples, especially after QC filter, and there is generally less spread in the data from MICP samples. To be representative for the facies, the MICP dataset from each facies should reflect both the porosity and permeability distribution from CCA samples. The P50 values, together with the distribution, should be similar, however, this is not the case here.

Overall, this QC study suggests biased MICP sampling towards best-quality rocks. For a future study, it would recommend selecting more MICP samples in the low porosity-permeability region to better reflect the CCA database. However, the grid cells used during reservoir modeling are coarse and the parameters assigned to the grid is intended to represent an average. Thus, it is not necessarily critical that these samples are underrepresented.

### 6.2.1  Quality Control of MICP Samples from Wells

Next, the MICP samples from the different wells was investigated, to study whether the MICP sample collection were representative of the porosity-permeability distribution of each well.

The study was performed by using scatter plots of permeability against porosity measured by CCA shown in Figure 6.4 and Figure 6.5. There are 9 plots, one for each well from which MICP samples are collected. The wells are here referred to as well A-I. The colored points are the MICP samples surviving QC filter. In addition to the observations made from the QC studies above, note that there are very few MICP samples that survives QC filter in the low porosity and permeability region, and there are some high permeability MICP samples that are removed. Furthermore, in well G and well I, there are very few samples in both low and high porosity-permeability region that survives QC, and the samples that do survive QC are outliers.

The study suggests that well A-F have a representative collection of MICP samples, if disregard the low porosity-permeability region. Furthermore, well G-I does not have a representative collection of MICP samples.
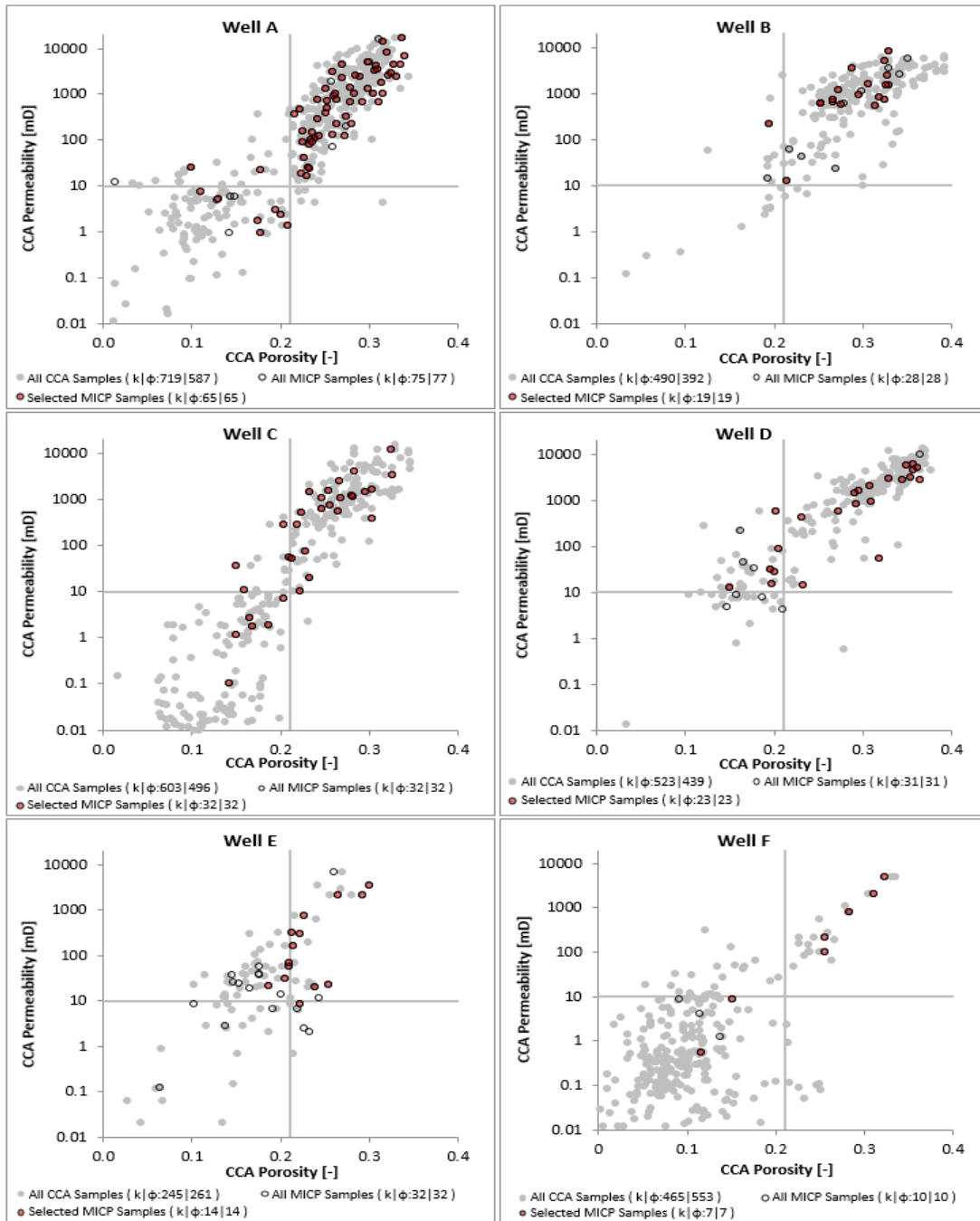
*Figure 6.4: Plots of permeability against porosity measured by CCA for 6 of the 9 wells with MICP samples, A-F. Grey points are CCA data, black hollow circles are MICP samples, and colored points are MICP samples surviving QC.*
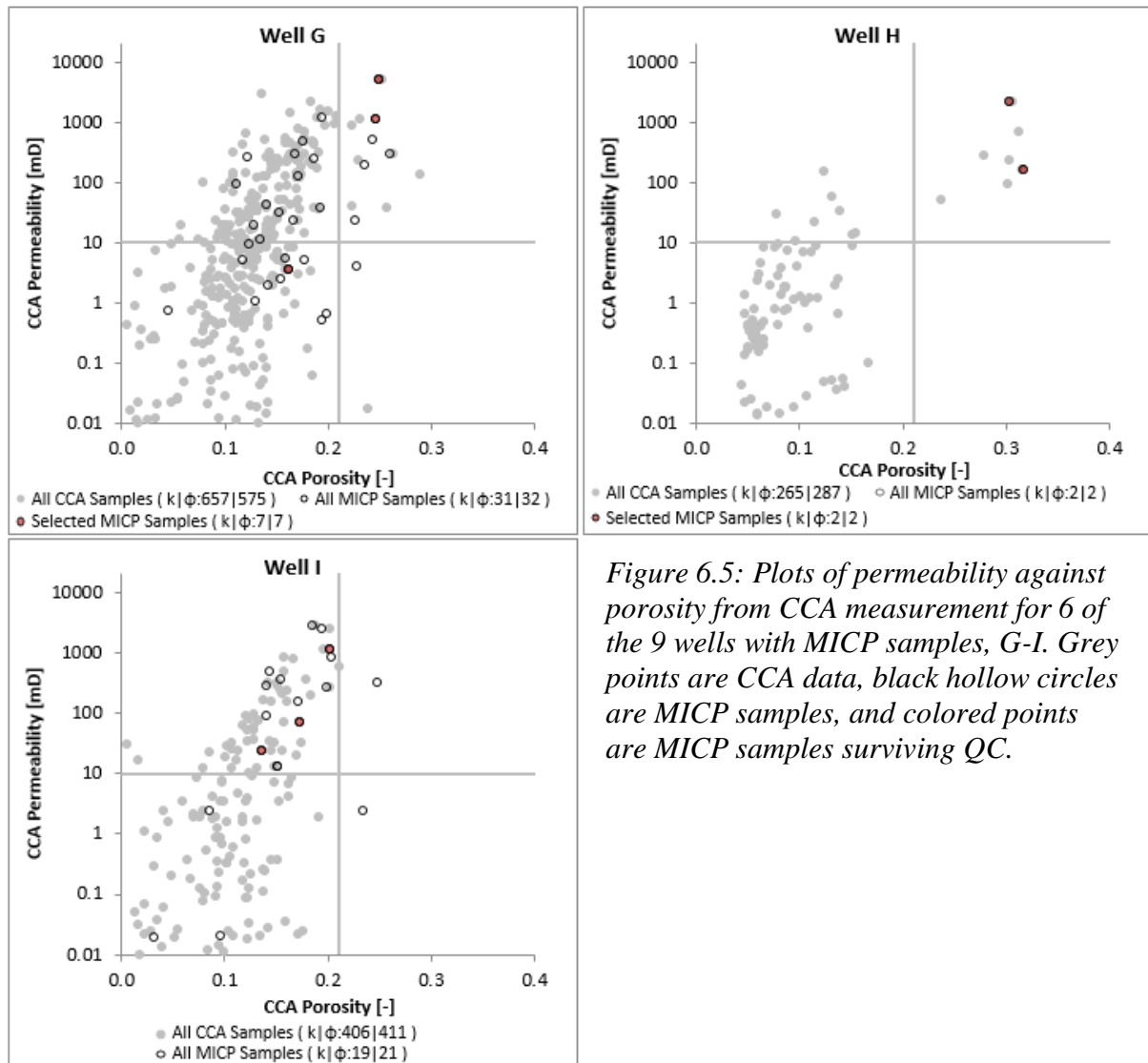
*Figure 6.5: Plots of permeability against porosity from CCA measurement for 6 of the 9 wells with MICP samples, G-I. Grey points are CCA data, black hollow circles are MICP samples, and colored points are MICP samples surviving QC.*

## 6.2.2 Quality Control of MICP Samples from Facies

The next QC of the MICP dataset was performed by investigating the MICP samples from the different facies. To study whether the MICP sample collection were representative of the porosity-permeability distribution of each facies.

In Figure 6.6, scatter plots of the permeability and porosity of all the samples measured by CCA was made. There are four plots, one for each facies. The colored points are the MICP samples surviving QC. Note that there are very few MICP samples at the low porosity-permeability, and the majority are removed by QC filter. There is a much higher scatter in the porosity-permeability distribution form the CCA samples (grey dots) than the MICP samples for Alluvial Sand Matrix and Alluvial Silty Matrix.

Non-weighted regression lines were included to the scatter plots in Figure 6.6, to investigate how the MICP sample collection was affected by QC filter. There are two regression lines for each facie, one for all MICP samples (colored line) and one for MICP samples surviving QC (black line). Note that the two regression lines should overlap for the QC filtered MICP samples to reflect all MICP samples.

For Aeolian facies (Figure 6.6a) the regression line from all MICP samples (yellow line) overlaps with the QC filtered MICP samples (black line). The QC filtered samples reflects the heterogeneity in the porosity-permeability distribution from CCA samples, when disregards the lower porosity-permeability region.

For Fluvial Aeol Rework, the observations were similar to that of Aeolian. The two regression lines are quite similar, and the selected samples capture the heterogeneity in the porosity-permeability distribution from CCA quite well, when disregards the lower porosity-permeability region.

For Alluvial Sand Matrix (Figure 6.6c) the observations were different. The two regression lines are quite different. The MICP samples from this facies has the poorest reflection of the porosity-permeability distribution from the CCA database, and many of the MICP samples are outliers.

For Alluvial Silty Matrix (Figure 6.6d) the regression lines are more similar than that for Alluvial Sand Matrix. However, the regression lines are slightly offset to lower increase in permeability with increasing porosity compared to the CCA samples.
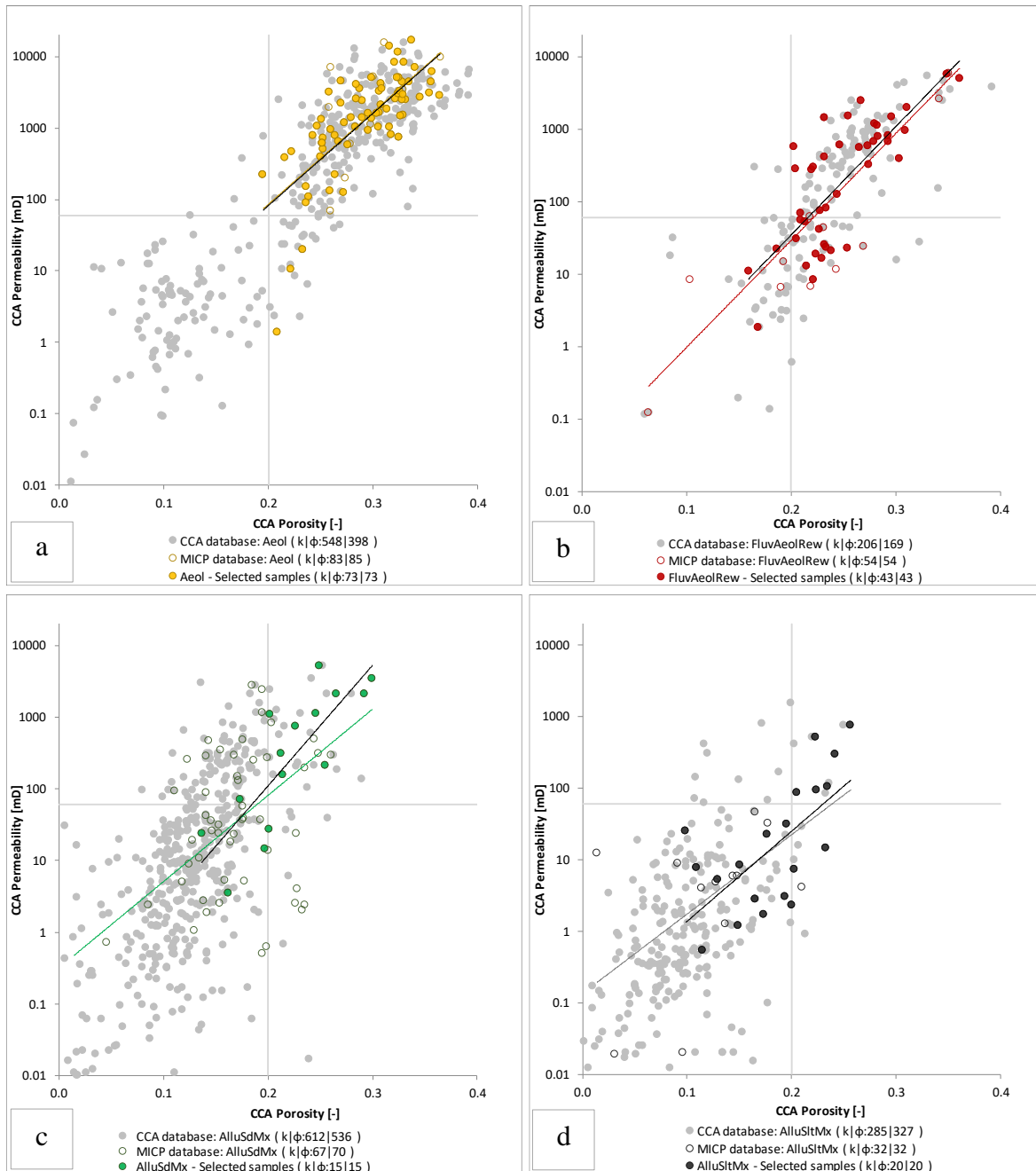
*Figure 6.6: Plots of permeability against porosity measured by CCA for (a) Aeolian, (b) Fluvial Aeol Rework, (c) Alluvial Sand Matrix, and (d) Alluvial Silty Matrix. The grey points are CCA samples, the hollow circles are MICP samples removed by QC, and the colored points are the QC filterd MICP samples. The colored line is the regression from the MICP database, while the black line is the regression from the selected (QC filtered) samples.*

The number of MICP samples by facies for each database were investigated and are listed in Table 6.2. Note that all facies meet the minimum requirement of 10 MICP samples for statistical validity. There is little reduction in the number of samples per facies for Aeolian Sand Matrix and Fluvial

*Table 6.2: Number of samples by the four main facies for each database.*

| Database | Number of samples by facies | | | |
|---|---|---|---|---|
| | Aeolian | Fluvial Aeol Rework | Alluvial Sand Matrix | Alluvial Silty Matrix |
| MICP | 85 | 54 | 70 | 32 |
| MICP (QC filter) | 73 | 43 | 15 | 20 |

Aeol Rework, and high reduction in the number of samples per facies for Alluvial Sand Matrix and Alluvial Silty Matrix. Highest reduction for Alluvial Sand Matrix.

Overall, this study showed that the MICP datasets from Aeolian and Fluvial Aeol Rework are representative, if disregard the low porosity-permeability region. The number of MICP samples from these to facies, are much higher than the minimum requirement for statistical validity. There is higher uncertainty related to the MICP datasets from Alluvial Sand Matrix and Alluvial Silty Matrix, especially the former. Although the number of samples per facies is greater than the minimum requirement for statistical validity, the great reduction in samples after QC filter together with poorer reflection of the porosity-permeability distribution, leads to uncertainty regarding the representativeness. Hence, any results from these two facies, especially Alluvial Sand Matrix, should be used with caution.

## 6.3 Review of the Curve Fitting Procedures

Furthermore, a comparison study between the two MICP curve fitting procedures: Thomeer hyperbolas and Gaussian distribution functions, was performed. The aim of the study was to investigate whether one model proved to be significantly better than the other based on parametrization of 273 samples.

Pore-throat size distribution plots was used to evaluate the curve fitting results, typical examples are shown in Figure 6.7 and Figure 6.8. There are two plots in each figure, one for each curve fitting result. The points are laboratory measurements, and the lines are curve fitting results. Note that for samples with good sorting (Figure 6.7) Thomeer model provides

better result than Gaussian model, and for samples with poor sorting (Figure 6.8) Gaussian model provides a better result than Thomeer model.
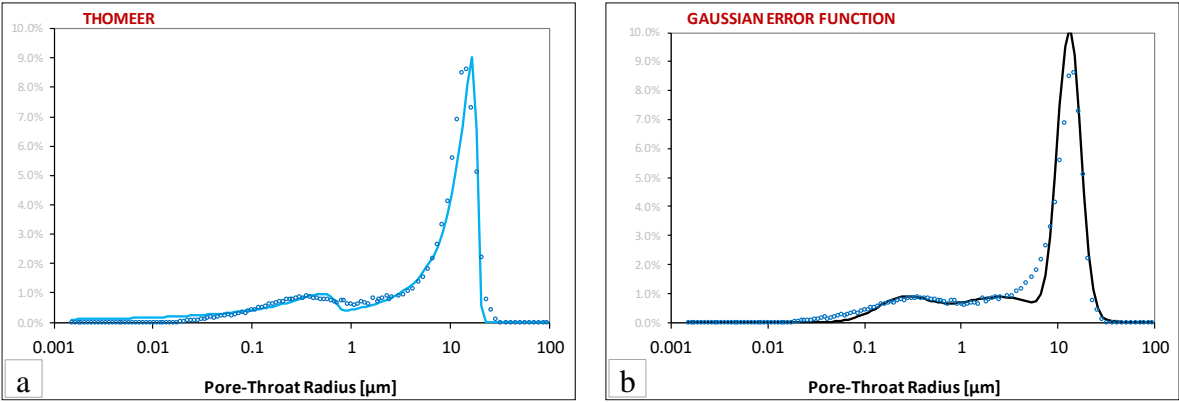


*Figure 6.7: Plots of a typical pore-throat size distribution where (a) Thomeer model provides a very good match, (b) Gaussian model provides poor match. The points are MICP measurenments converted to pore-throat sizes, and the lines are curve matches. Note that Gaussian model needs three curves to match the two pore systems evident in the data.*
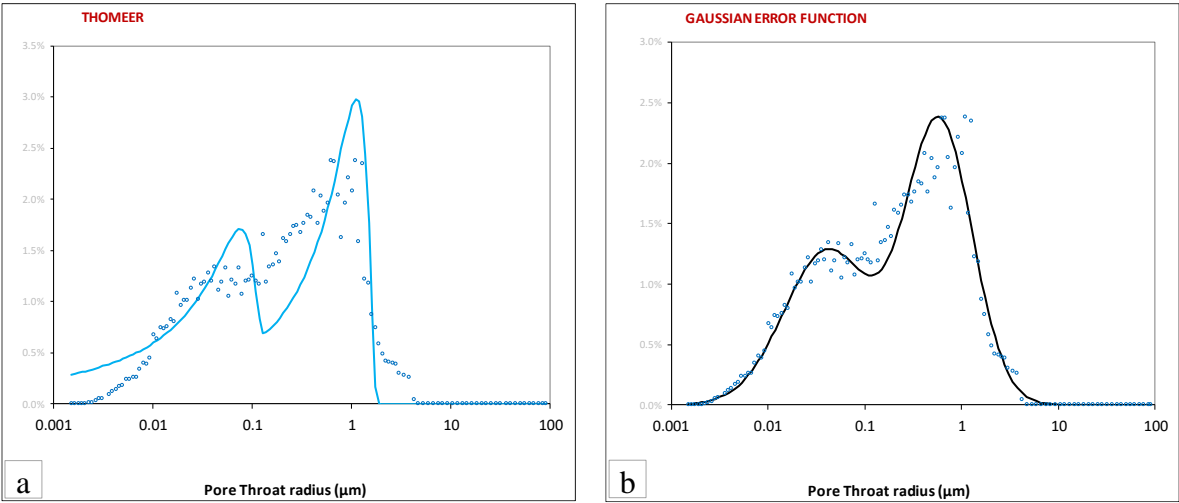


*Figure 6.8: Plots of a typical pore-throat size distribution where (a) Thomeer model provides a poor match, (b) Gaussian model provides a better match. The points are MICP measurenments converted to pore-throat sizes, and the lines are curve matches.*

The study showed that Thomeer model provided good curve fitting results on MICP data from samples with good sorting, i.e. less heterogeneous pore-throat distribution (Figure 6.7a). For samples with poor sorting, i.e. heterogeneous pore-throat distribution, the model provided poor results (Figure 6.8a).

The study also showed that Gaussian model did not provide good curve fitting results on MICP data from samples with good sorting, i.e. less heterogeneous pore-throat distribution (Figure 6.7b). For samples with poor sorting, i.e. heterogeneous pore-throat distribution, the model provided poor results (Figure 6.8b).

Aeolian and Fluvial Aeol Rework are aeolian sandstones with relatively good sorting. For these samples the Thomeer model generally provided good curve fitting results. Alluvial Sandy Matrix and Alluvial Silty Matrix are alluvial fan conglomerates with relatively poor sorting. For these samples the Thomeer model generally did not provide good curve fitting results.

The QC filter used on the MICP samples were based on Thomeer curve fitting results. This explains why the majority of the MICP samples from alluvial fan conglomerates, in Figure 6.6, were rejected by QC filter. In addition, why the majority of MICP samples from aeolian sandstones, in Figure 6.6, survived QC filter.

Overall, this study shows that parametrization of MICP data using Thomeer model generally provides good results of MICP data from aeolian sandstones in Edvard Grieg field. It does not, however, provide good results on the majority of MICP data from alluvial fan conglomerates. Hence, a separate workflow or a separate QC flag (unaffected by Thomeer model) for the Gaussian model are recommended for future MICP parametrization studies of alluvial fan conglomerates. Furthermore, the curve matching procedures are time-consuming by using the proposed workflow. Hence, a more automated access, while maintaining the sample-by-sample QC are recommended for future studies.

## 6.4  Results from Database

After the curve fitting procedures review of the curve fitting procedures was finalized, the data from the resulting QC filtered MICP database were thoroughly examined.

The MICP data from each sample was parameterized using Thomeer hyperbolas and modified Gaussian error functions. The results from both models were included in the MICP databases. Due to time constraints the Thomeer parameters was chosen for further investigations, since the workflow is mainly based on Thomeer results.

A total of 293 Thomeer hyperbolas was used to curve fit the MICP data from the 151 QC filtered MICP samples from the four facies, that is 293 $P_d$, $V_{b\infty}$, and $G$ values. In Table 6.4, a table of the pore system modality of the different facies was made. The pore system modality is referred to as the number of Thomeer hyperbolas (pore systems) required to fit the MICP data from each sample. Note that all facies mainly have bimodal pore-throat size distribution, which is probably related to the heterogeneous origin of the Edvard Grieg field.

*Table 6.3: Pore system modality of the different facies.*

| Facies | Number of pore systems [%] | | |
|---|---|---|---|
| | **1** | **2** | **3** |
| Aeolian | 16.4 | 75.3 | 8.2 |
| Fluvial Aeol Rework | 20.9 | 62.8 | 16.3 |
| Alluvial Sand Matrix | 13.3 | 53.3 | 33.3 |
| Alluvial Silty Matrix | 30.0 | 60.0 | 10.0 |

## 6.4.1 Comparison of MICP and CCA Porosity

The CCA (He) porosity and the porosity derived from MICP was investigated.

In Figure 6.9, a plot of CCA porosity against MICP porosity was made. The red points are the data, the dashed line is the one-to-one (1-1) relationship and the black line is a linear regression line. Note that the CCA porosity is generally higher than MICP porosity (possible reasons are listed in Table 6.4), however the correlation factor ($R^2$) is high.
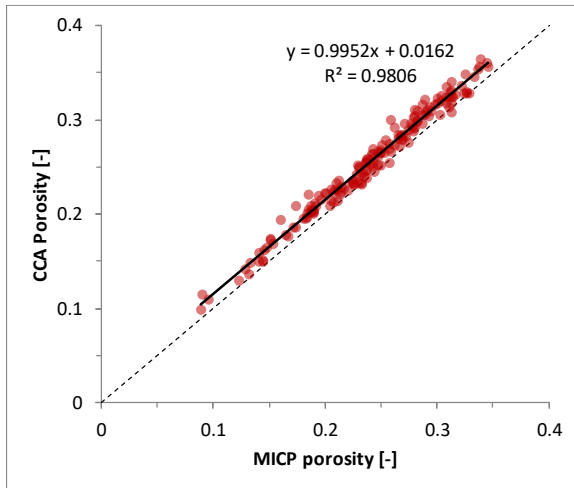
*Figure 6.9: CCA (He) porosity vs MICP porosity for QC filtered samples. The red points are data, the stipled line is 1-1 relationship, and the black line is a linear regression line.*

*Table 6.4: Some possible reasons why CCA (He) porosity overestimates MICP porosity.*

| Cause | Description |
|---|---|
| Size of helium (He) atoms | He atoms are very small in size and are thus able to intrude to smaller pores than mercury. |
| High pressure MICP measurements | The shape of the MICP curve can be affected by sample compressibility and thermal effects which results in higher uncertainty related to total volume of mercury intruded. |
| Pore volume size | Uncertainty is also a function of the pore volume size, for example, He porosity may be slightly overestimated when measured on smaller end trims. |

## 6.4.2 Comparison of MICP and CCA Permeability

Next, the Thomeer permeability was calculated from the Thomeer parameters from the first pore system, and then compared with CCA ($k_l$) permeability.

In Figure 6.10, a scatter plot of Thomeer permeability and permeability measured by CCA was made. The green triangles are datapoints, the black line is regression. Note that the CCA permeability tends to be slightly higher than Thomeer permeability, and that the correlation factor ($R^2$) is high.

Based on the observation that CCA permeability tends to be higher than Thomeer permeability, attempts were made to include the second pore system to the Thomeer permeability calculations. The attempts did not provide significant improvement, and the high $R^2$ of 93 % strongly suggests that the first pore system has primary control on permeability.
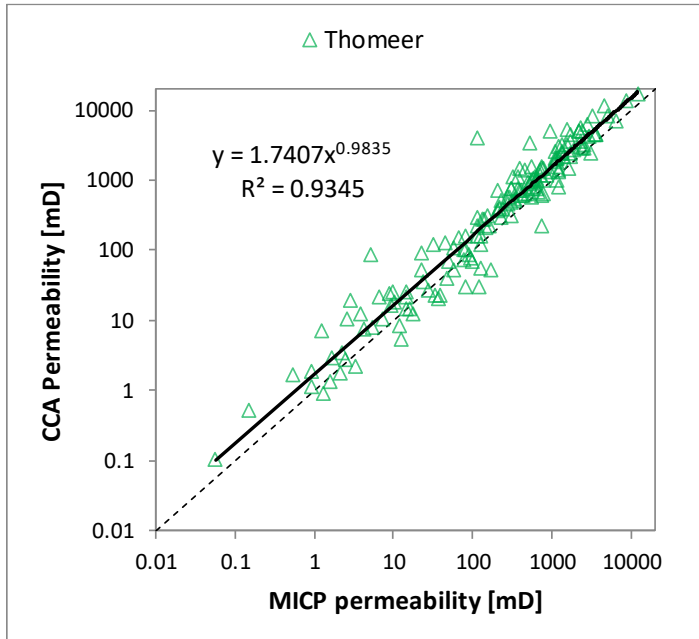
*Figure 6.10: Log-log plot of CCA permeability against Thomeer permeability. The Thomeer parameters from the first pore system was used to calculate Thomeer permeability.*

### 6.4.3  MICP Curves

The closure-corrected MICP curves and corresponding pore-throat size distributions was investigated to evaluate whether the different facies characteristics was reflected in the MICP data. Among other, to investigate whether the MICP dataset from one facies are sufficiently homogeneous to assign one unique rock type to the facies, or whether it will be necessary to divide the facies into several rock types.

In Figure 6.11, a log-log plot of MICP curves was made, colored by facies. Note that there is a large spread in the capillary pressure curves, also within the facies, however tendencies of groupings are evident. Aeolian tend to group in the low MICP for a given bulk volume occupied by mercury in [%], $V_b$. Followed by Fluvial Aeol Rework, Alluvial Sand Matrix and Alluvial Silty Matrix from lower to higher MICP for a given $V_b$, respectively.

In Figure 6.12, a plot of pore-throat size distributions was made, colored by facies. Note that there is a large spread in the pore-throat size distributions, also within the facies, and the same tendencies of groupings are evident.

This study suggests that the MICP curves are not necessarily sufficiently homogeneous for assigning one unique rock/pore type to describe one facies.
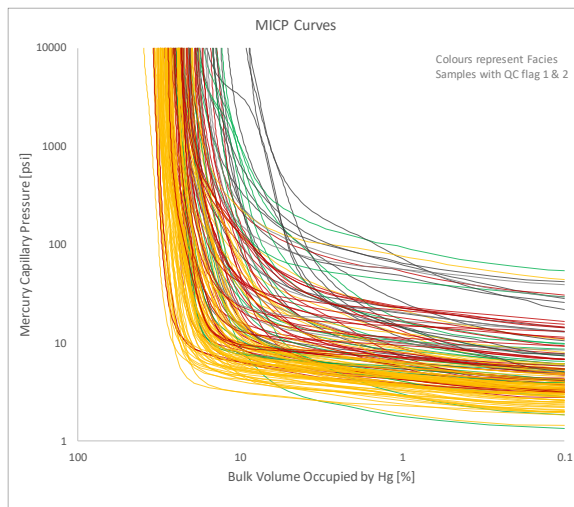


*Figure 6.11: MICP curves colored by the facies considered from QC filtered samples.*
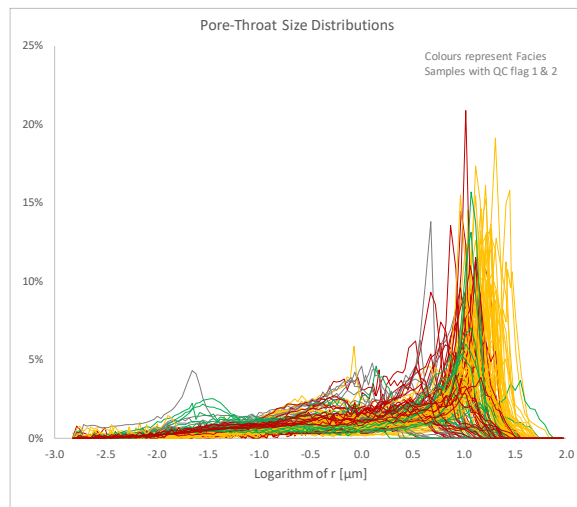


*Figure 6.12: Pore-throat size distribution colored by the facies considered from QC filtered samples.*

### 6.4.4  Thomeer Median (P50) Hyperbolas

Thomeer curve fitting parameters from the first pore system was studied. The aim was to investigate whether there was a distinct connection between Thomeer parameters and facies.

In Figure 6.13, a plot of MICP against $V_b$ was made. There are four Thomeer hyperbolas, one for each facie. The Thomeer hyperbolas was defined by the P50 Thomeer parameters from the first pore system, values are listed in Table 6.5. Note that there is a clear distinction between the Thomeer P50 hyperbolas for the different facies. Aeolian facies show the most optimistic MICP curve, while Alluvial Silty Matrix shows the least optimistic. In Figure 6.14 the Thomeer P50 hyperbolas was converted to saturation height functions, which illustrates how the non-wetting fluid behavior with increasing height above FWL.
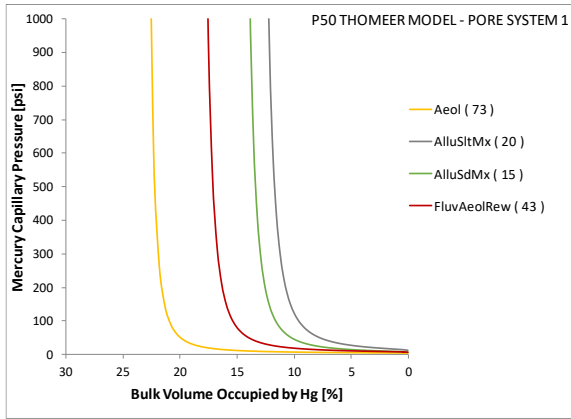
*Figure 6.13: Thomeer hyperbolas constructed from the P50 Thomeer parameters for the first pore system, colored by facies. The Thomeer hyperbola is displayed in a linear plot of MICP against $V_b$.*
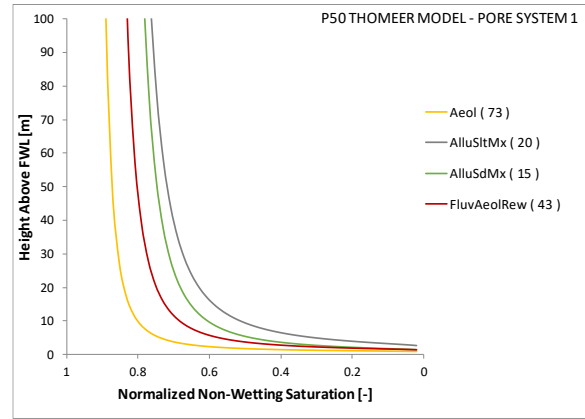
*Figure 6.14: Plot of Thomeer P50 hyperbolas converted to saturation height functions. Height above FWL against normalized non-wetting saturation.*

Aeolian (yellow curve) has the lowest P50 for $P_{d,1}$ and $G_1$, i.e. largest pore-throats and best sorting, compared to the other facies. Combined with highest $V_{b\infty,1}$, Aeolian has higher permeability than the other facies; see Table 6.5.

Fluvial Aeol Rework (red curve in Figure 6.13) has the second lowest P50 for both $P_{d,1}$ and $G_1$, and the second highest $V_{b\infty,1}$. Hence, the facies show poorer sorting, smaller pore-throat sizes and lower reservoir quality than Aeolian, but better sorting than the alluvial fan conglomerates.

Alluvial Sand Matrix (green curve in Figure 6.13) has the second highest P50 for $P_{d,1}$ together with second lowest $V_{b\infty,1}$. Consequently, the facies show better reservoir quality with respect to permeability than Alluvial Silty Matrix, as expected. Despite having slightly higher $G_1$ than Alluvial Silty Matrix. $P_{d,1}$ seems to have the main control over permeability.

Alluvial Silty Matrix (grey curve in Figure 6.13) has the highest P50 for $P_{d,1}$ together with the lowest $V_{b\infty,1}$. Consequently, it is the facies with generally lowest reservoir quality with respect to permeability. Despite the fact that the P50 $G_1$ value is slightly lower than for Alluvial Sand Matrix. Alluvial Silty Matrix generally shows a slightly more homogeneous pore-throat distribution, which can also be observed from Table 6.4, than Alluvial Sand Matrix, but with smaller pore-throats explaining the lower permeability.

In Figure 6.17, Thomeer P50 hyperbolas was superimposed on the MICP plot from Figure 6.11. Colored by facies, highlighted lines are P50 hyperbolas. Note that the P50 hyperbolas are able to reflect the principal differences of the facies. The red dashed line is Maximum HC column height and was included to demonstrate the most essential parts of the capillary pressure curve.

Overall, it seems to be potential to investigate the possibility of using the Thomeer parameters for rock/pore-typing, like intended in this study, especially $P_d$. There is also potential for a later study to investigate the possibilities for application of the Thomeer hyperbolas to saturation-height modeling. The study could start with comparison of the P50 Thomeer models for each facies to the existing model.
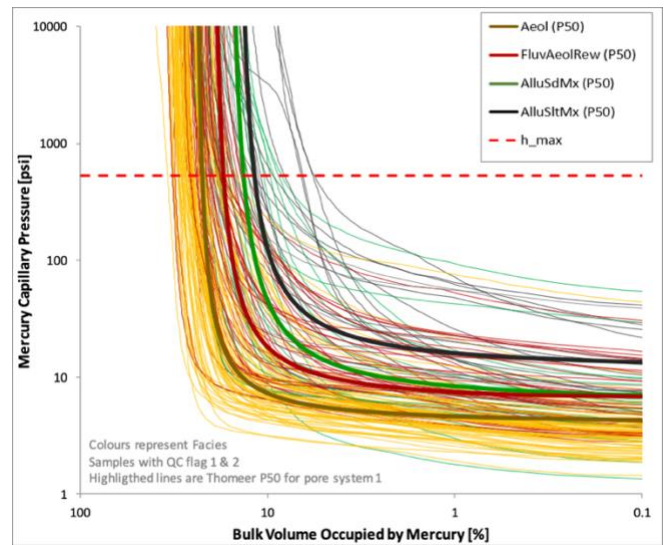


*Figure 6.15: The Thomeer P50 curves for the first pore system, superimposed on MICP curves colored by facies from QC filtered samples, in log-log space. The red dashed line is maximum HC column height converted to mercury capillary pressure.*

*Table 6.5: P50 for QC filtered MICP samples*

| Facies | $P_{d,1}$ [psi] | $V_{b\infty,1}$ [%] | $G_1$ | $k_{Thomeer}$ [mD] | $\varphi_{MICP}$ [-] | $k_{Kl}$ [mD] | $\varphi_{He}$ [-] |
|---|---|---|---|---|---|---|---|
| Aeolian | 3.9 | 25.1 | 0.25 | 1147.2 | 0.28 | 1558.0 | 0.30 |
| Fluvial Aeolian Rework | 5.6 | 20.7 | 0.37 | 215.5 | 0.23 | 292.2 | 0.23 |
| Alluvial Sand Matrix | 5.7 | 17.2 | 0.48 | 154.5 | 0.21 | 312.7 | 0.21 |
| Alluvial Silty Matrix | 10.9 | 15.4 | 0.46 | 10.9 | 0.18 | 11.4 | 0.19 |

## 6.4.5  Thomeer Parameters

The Thomeer parameters from the first pore system were studied. The study was conducted to evaluate whether the Thomeer parameters could provide cut-offs for rock/pore typing.

### 6.4.5.1  Cluster Analysis of Thomeer Parameters

First, investigation of correlation between $P_{d,1}$ and $G_1$, i.e. displacement pressure with sorting, was performed. Simple cluster analysis was used for the investigation. The result is shown in Figure 6.16, the boxes represents P25 and P75 values, while the dashed lines represents P10 and P90 values. There are four clusters, one for each facies. Note that there is a clear distinction between Aeolian and Alluvial Silty Matrix, while there is less distinction between Fluvial Aeol Rework and Alluvial Sand Matrix.

Second, correlation between $P_{d,1}$ and $V_{b\infty,1}$, i.e. displacement pressure with effective pore volume of the first pore system, was performed. The same type of cluster analysis as the above study was used. The result is shown in Figure 6.17. There are four boxes, one for each facies. The observations are similar to the study above, there is a clear distinction between Aeolian and Alluvial Silty Matrix, while there is less distinction between Fluvial Aeol Rework and Alluvial Sand Matrix.
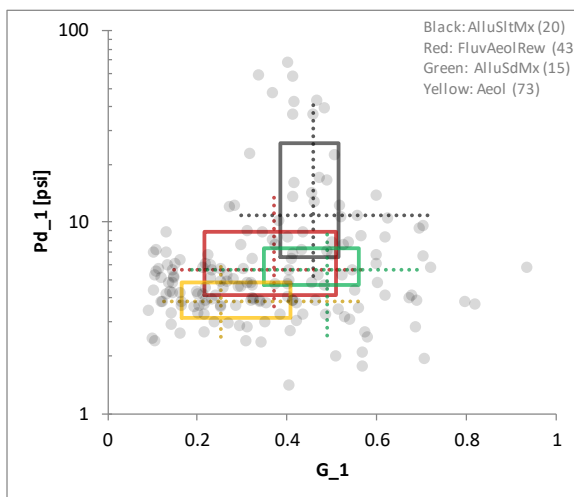


*Figure 6.16: $P_{d,1}$ is plotted against $G_1$ for simple cluster analysis. The boxes represent P25 and P75, while the lines are P10 and P90.*
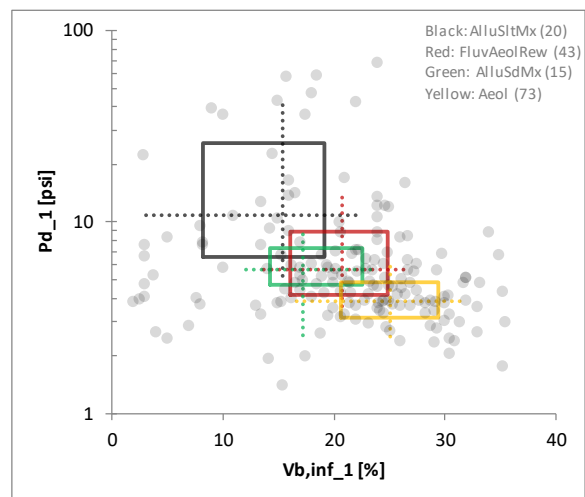
*Figure 6.17: $P_{d,1}$ is plotted against $V_{b\infty,1}$ for simple cluster analysis. The boxes represent P25 and P75, while the lines are P10 and P90.*

### 6.4.5.2 Comparison of CCA Permeability and Thomeer Parameters

Next, comparison of CCA permeability and the Thomeer parameters from the first pore system $P_{d,1}$, $V_{b\infty,1}$ and $G_1$ was performed.

In Figure 6.18, a scatter chart of CCA permeability and the Thomeer parameters from the first pore system was made. There are three plots, one for each Thomeer parameter, colored by facies. Note that there is highest correlation between CCA permeability and $P_{d,1}$. Increase in CCA permeability with increase in largest pore-throat. There is a higher scatter in the relation between CCA permeability and $V_{b\infty,1}$ and $G_1$, highest for $G_1$. However, they follow the expected trends: the permeability increased with decreasing $G_1$ and with increasing $V_{b\infty,1}$. Moreover, note that all facies follow the same trends.

Similar to the findings of (Clerke et al., 2008), this study suggests that the major control on permeability is the Thomeer parameter, $P_{d,1}$. It is difficult to separate the observations by facies other than the tendencies observed from earlier, namely that Aeolian tends to dominate the high permeability region, followed by Fluvial Aeol Rework, Alluvial Sand Matrix and Alluvial Silty Matrix from higher to lower permeability regions, respectively.
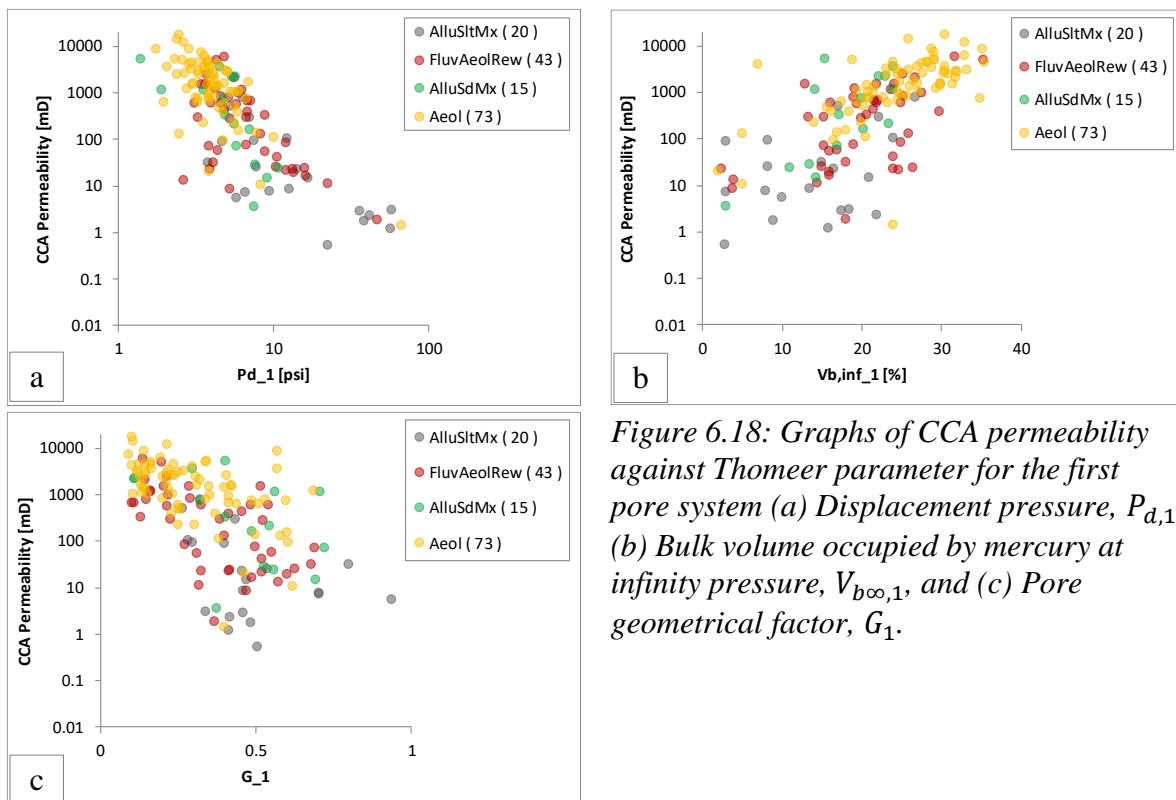
*Figure 6.18: Graphs of CCA permeability against Thomeer parameter for the first pore system (a) Displacement pressure, $P_{d,1}$, (b) Bulk volume occupied by mercury at infinity pressure, $V_{b\infty,1}$, and (c) Pore geometrical factor, $G_1$.*

A similar study was conducted to compare the curve fitting parameters of the Thomeer model and the Gaussian model, to investigate whether one model would prove to be significantly better than the other. The study is included in Appendix A.

### 6.4.5.3   Two-Term Permeability Model

To further investigate whether the Thomeer parameter, $P_{d,1}$, could be used to predict permeability, the two-term permeability model proposed by Clerke et al. (2008) was investigated.

To modify the empirical constants to fit data form Edvard Grieg field, goodness-of-fit tests were performed from the MICP dataset used in this thesis. The empirical constants were found by to be $a = -2.42, b = 1.35$ and $c = 0.112$. The resulting modified two-term permeability model became:

$$\text{Log}(k_{\text{predicted}}) = -2.42 + 1.35 \times \text{Log}(d_{max}) + 0.112 \times (\varphi),$$

where k is the predicted permeability in [mD], $d_{max}$ is maximum pore-throat diameter calculated from $P_{d,1}$ in [µm] and $\varphi$ is the porosity in [%].

In Figure 6.19, a scatter chart of predicted two-term permeability and CCA permeability was made. Black points are data and the dashed red line is the 1-1 relationship. Note that the predicted permeability gives very good predictions over several orders of magnitude in permeability. There is a high correlation, with $R^2$ of 85%. This suggests that the model works well also for clastic reservoirs.

The two-term permeability model reduces the number of unknowns compared to Thomeer permeability equation, with proper calibration, log-derived porosity may be used to predict permeability. If so, $P_{d,1}$ is the only unknown. This study suggests that if a clear link is established between $P_{d,1}$ and a continuous value in wells that can be extrapolated to 3D, the two-term model may have potential for improved permeability predictions for the Edvard Grieg field.
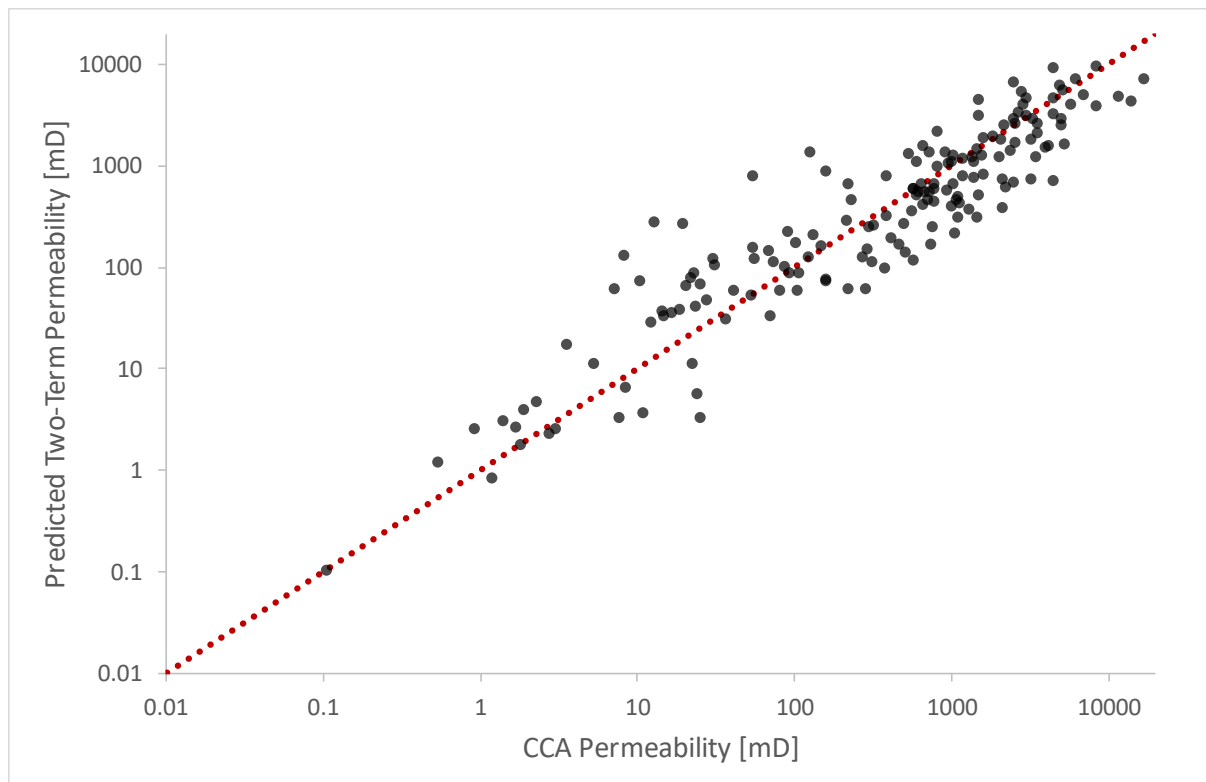
*Figure 6.19: Predicted permeability using Clerke et al. (2008) two-term permeability model with modified empirical constants for the data from Edvard Grieg versus measured (CCA) permeability.*

## 6.5 Rock/Pore Typing Attempts

After the MICP dataset were closely investigated, simple rock/pore typing attempts was performed. The aim was to investigate whether rock/pore types based on MICP data could establish improved relationships between porosity and permeability on Edvard Grieg field. First, two rock/pore typing attempts based on the Thomeer parameter, $P_d$, were performed, followed by an attempt based on the mode of the pore-throat size distribution.

### 6.5.1 Rock/Pore Typing Methods Based on Parametrizations of MICP Curves

After closely investigation of Thomeer parameters, there was established that there was highest correlation between the Thomeer parameter, $P_d$, and permeability. Based on this observation it was investigated whether the Thomeer parameter, $P_d$, could be used as cut-off for rock/pore typing. First, a study based on the displacement pressure from the first pore system, $P_{d,1}$, was performed. Followed by a study inspired by Clerke et al. (2008) Porositons groups.

### 6.5.1.1 Rock/Pore Typing Based on Thomeer Parameter, $P_{d,1}$

First, rock/pore typing attempt based on Thomeer parameter, $P_{d,1}$, was performed. $P_{d,1}$ was converted to the size of the largest pore-throat ($r_{max,1}$), to be more relatable.

In Figure 6.20, a scatter chart of permeability and porosity measured by CCA was made. The points are colored by rock/pore type based on $r_{max,1}$ cut-off values, listed in Table 6.6. Note that groups show order, especially the two groups defined by smallest $r_{max,1}$, namely group 3 and 4. There is a higher scatter between the two groups with greatest $r_{max,1}$. Overall, relatively distinct porosity-permeability trends are observed.

The definition of the groups was defined by observations and trials from the cumulative frequency of $r_{max,1}$ (Figure 6.21), so it should be improved for proper analyses. However, the aim of this study was to evaluate whether it has potential for rock/pore typing, more advanced analyses tools are necessary to establish rock/pore types.
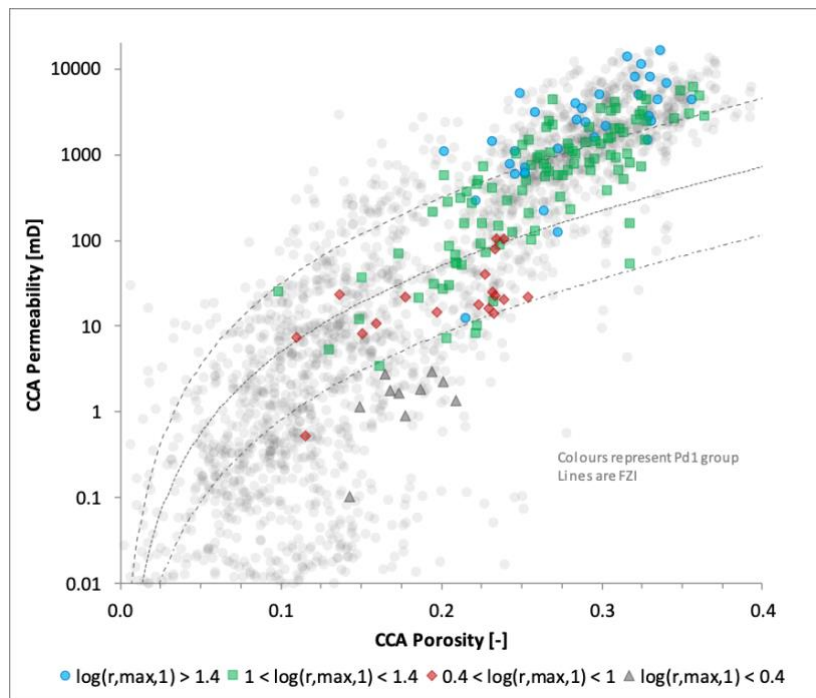


*Figure 6.20: Graph of permeability against porosity, with colors from grouping of samples based on Thomeer parameter $P_{d,1}$. The grey circles are CCA data and the lines are FZI, included as a reference.*

Table 6.6: Definitions of groups based on size of the larges pore-throat.

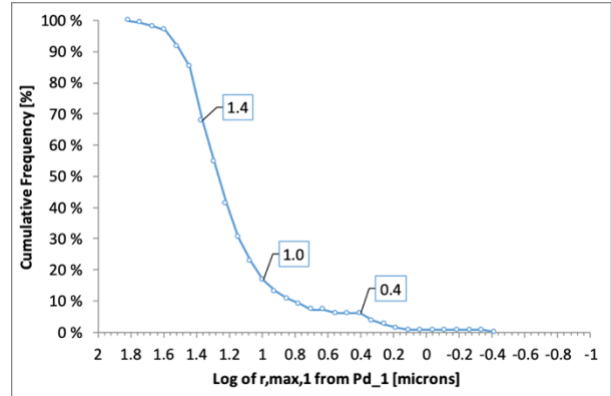| Group | Symbol | Definition |
|---|---|---|
| 1 | ⬤ | $\text{Log}(r_{max,1}) > 1.4$ |
| 2 | ⬛ | $1 < \text{Log}(r_{max,1}) < 1.4$ |
| 3 | ◆ | $0.4 < \text{Log}(r_{max,1}) < 1$ |
| 4 | ▲ | $\text{Log}(r_{max,1}) < 0.4$ |



Figure 6.21: Histogram of cumulative frequency [%] of $r_{max,1}$ calculated from $P_{d,1}$. Selected $r_{max,1}$ limits for grouping are highlighted.

### 6.5.1.2 Method Based on Thomeer Parameter, $P_d$

Next, a study based on Clerke et al. (2008) Porositons grouping method was performed. The method involves grouping after modes of $P_d$ distribution. Thomeer parameter, $P_d$, from up to three pore systems for each sample were used for grouping. $P_d$ is converted to size of the largest pore-throat for pore system i ($r_{max,i}$) to be more relatable.

In Figure 6.22, a scatter chart of permeability and porosity measured by CCA was made. The points are colored by rock/pore type based on combinations of $P_d$ values for each sample. Note that the general trends are quite similar to that observed for rock/pore typing attempt based on $P_{d,1}$, in Figure 6.20.

The definitions used for the classification of each pore system are listed in Table 6.7, and the definition of the groups is present in Figure 6.22. An example, if the first pore system classifies as 2 and the second as 3, then the sample has combination 2-3, and belongs to group E.

The definition of the classifications was defined by observations and trials from the cumulative frequency of $r_{max,i}$, shown in Figure 6.23, so it should be improved for proper analyses. However, the results of the grouping after $P_d$ is quite similar to grouping after $P_{d,1}$.

Based on this observation, the grouping after $P_{d,1}$ may be preferred rather than $P_d$, since it only contain one cut-off parameter.
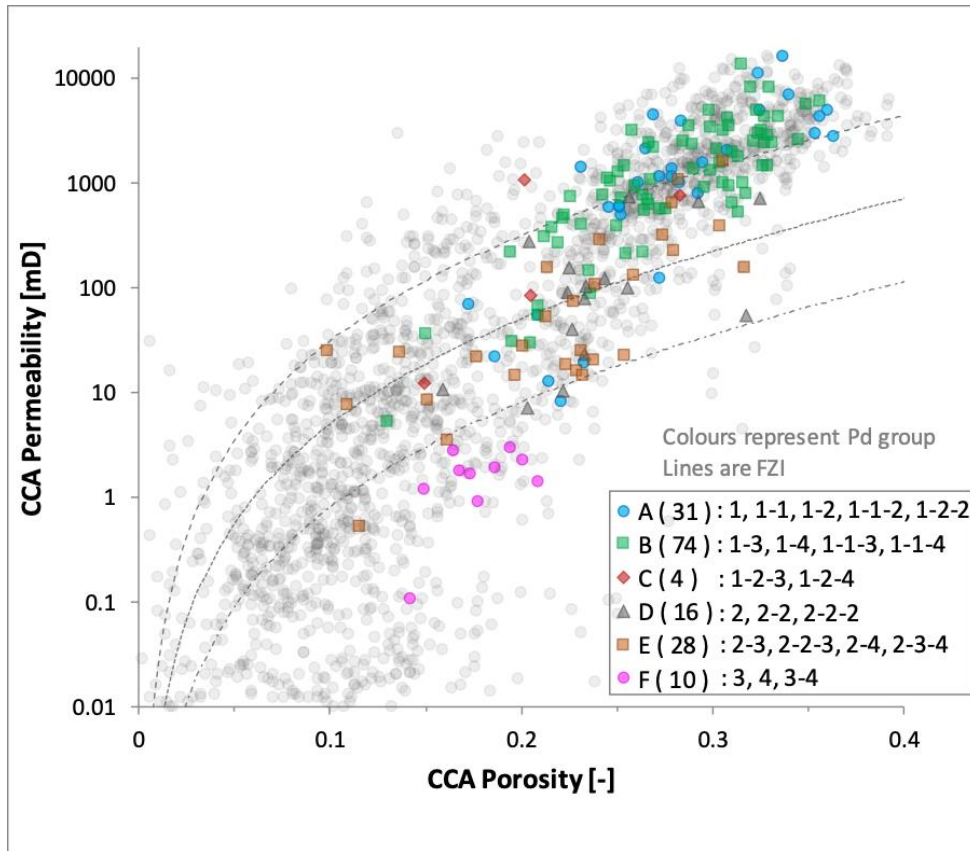


*Figure 6.22: Graph of permeability against porosity, with petrophysical rock types based on combinations of the Thomeer parameter $P_d$, from each pore system. The grey circles are CCA data and the lines are FZI, added as a reference.*

*Table 6.7: Classifications of pore systems (up to three) for each sample.*

| Classification | Definition (i = pore system, 1-3) |
|---|---|
| 1 | $\text{Log}(r_{max,i}) > 1.17$ |
| 2 | $0.43 < \text{Log}(r_{max,i}) < 1.17$ |
| 3 | $-0.53 < \text{Log}(r_{max,i}) < 0.43$ |
| 4 | $\text{Log}(r_{max,i}) < -0.53$ |
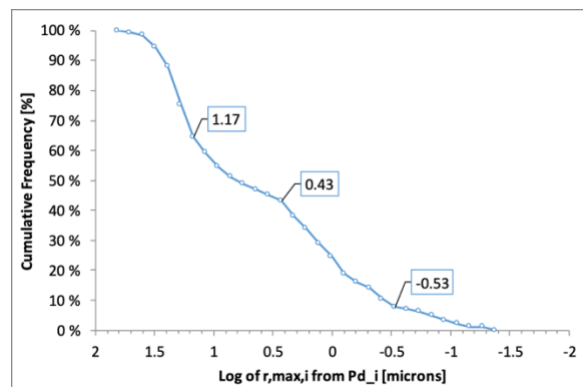


*Figure 6.23: Cumulative frequency [%] of $P_{d,i}$ converted to $r_{max,i}$.*

## 6.5.2 Rock/Pore Typing Based on Mode of Pore-Throat Size Distribution

Rock/pore typing attempt based on the mode of the pore-throat distribution was performed.

In Figure 6.24, a scatter chart of permeability and porosity measured by CCA was made. The points are colored by rock/pore type based on mode of pore-throat size distribution. Note that there is a relatively clear distinction between the rock types, especially if one combines the Micro and Meso groups.

The cut-off values used for each group are listed in Table 5.3. The values were selected based on the pore-throat size definitions given in Table 5.3. Note that the nano size is added to the Micro group.
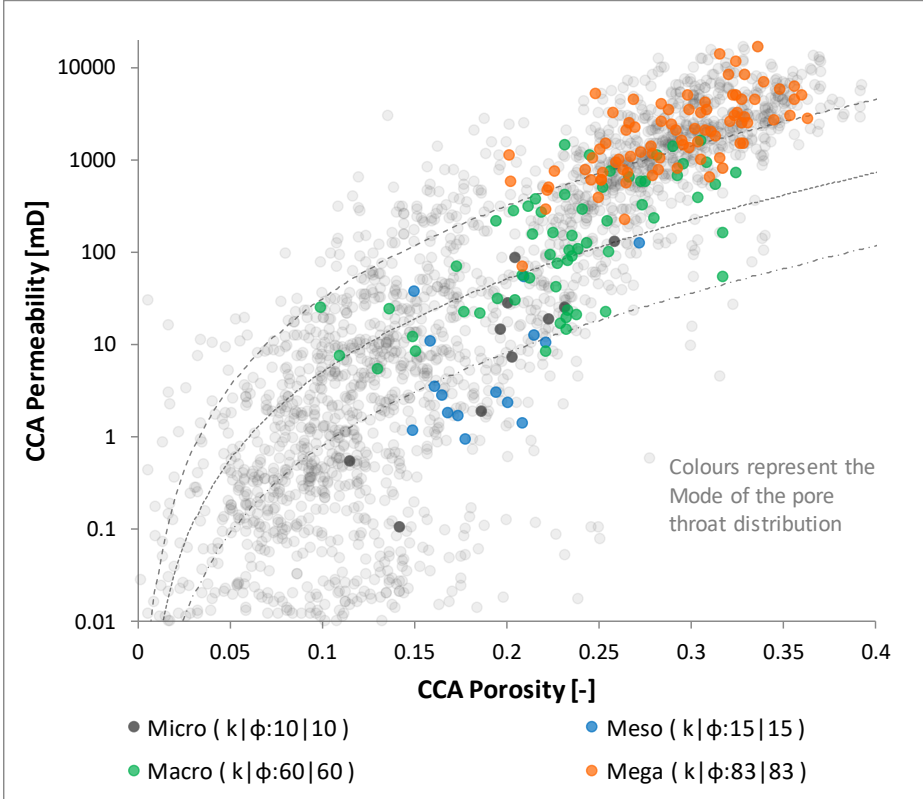


*Figure 6.24: Graph of permeability against porosity, with petrophysical rock types based on mode of pore-throat size distribution. The grey circles are CCA data and the lines are FZI, added as a reference.Porosity-permeability rock. FZI lines are added as reference.*

*Table 6.8: Definitions of groups based on mode of pore-throat distribution.*

| Group | Symbol | Definition [µm] |
|-------|--------|-----------------|
| Micro | ● | $r_{mode} < 0.5$ |
| Meso | ● | $0.5 < r_{mode} < 2$ |
| Macro | ● | $2 < r_{mode} < 10$ |
| Mega | ● | $r_{mode} > 10$ |

Overall, these rock/pore typing attempts suggest that parametrization of MICP curves may have potential for rock/pore typing of the complex, multi-modal formations in Edvard Grieg field, but future studies are needed to confirm.

# 7 Conclusions and Future Recommendations

This study aimed to investigate whether parametrization of MICP data could be used for rock/pore typing of the complex, multi-modal formations in Edvard Grieg field. Among other applications, this could improve the predictions of the permeability distribution in this field. In this study, 273 MICP samples were analyzed, including QC, with lithology ranging from aeolian sandstones to alluvial fan conglomerates. The parametrizations were conducted using Thomeer hyperbolas and modified Gaussian error functions. Special attention was given to QC of the MICP raw data, parametrizations, and the resulting MICP dataset.

## 7.1 Conclusions

The following conclusions can be drawn from the results:

- The study identified biased MICP sampling towards best-quality rocks. An implication of this is the possibility that any MICP-based rock types might not be representative of the formations in Edvard Grieg field.

- The study also identified a critical weakness of the Thomeer curve fitting procedure: it is sensitive to heterogeneous pore-throat distributions, resulting in unrealistic Thomeer parameters. These findings clearly indicate that the Thomeer curve fitting procedure is not suitable for evaluation of alluvial fan conglomerates, since the complex microstructure of these formations is often associated with heterogeneous pore-throat distributions.

- The results suggest that modified Gaussian error functions could be a better alternative for MICP parametrization of MICP data from Alluvial fan conglomerates than the Thomeer curve fitting procedure, but further investigations are needed. On the other hand, the Thomeer hyperbolas provides good curve fitting results for samples with less heterogeneous pore-throat distributions, such as aeolian sandstone.

- In the analyzed data, there was a very high correlation between measured permeability and permeability estimated using the Thomeer (1983) permeability equation. There was also a high correlation between measured permeability and the Thomeer parameter for displacement pressure ($P_{d,1}$). In addition, the two-term permeability model proposed by Clerke et al. (2008) with modified empirical constants for the data from the Edvard Grieg field provided good results, reducing the number of unknowns to maximum pore-throat size and porosity. This suggests that permeability can be predicted from log-derived porosity if it is possible to find a clear link between maximum pore-throat size

and a parameter that can be extrapolated in 3D models, like facies. Further investigations are needed to establish such relations.

- Results from simple rock/pore typing attempts suggest that the Thomeer parameter equivalent to largest pore-throat radius, could be used as cut-off parameter for rock/pore typing of the complex, multi-modal formations in Edvard Grieg field, but future studies are needed to confirm.

Overall, the study suggests that rock/pore typing based on parametrization of MICP data may be useful for the Edvard Grieg field, but future studies are needed to confirm.

## 7.2  Future Recommendations

Future studies are recommended and might explore:

- Repeating the study with a separate QC filter for curve fitting results from modified Gaussian error functions, for potentially better evaluation of the alluvial fan conglomerates in the Edvard Grieg field.
- A more automated workflow while maintaining the sample-by-sample QC, to increase analysis speed.
- Additional MICP sampling, to gather a more representative MICP database.
- Using more advanced analyses to identify rock/pore types, like in porosity-permeability space or 3D space of the Thomeer (or Gaussian) parameters.
- Potentially utilizing Thomeer parameter results for improved water saturation modeling.

# 8 References

Abdallah, W., Buckley, J. S., Carnegie, A., Edwards, J., Herold, B., Fordham, E., . . . Ziauddin, M. (2017). Fundamentals of Wettability. *Oilfield Review, 19*(2). Retrieved from https://www.slb.com/~/media/Files/resources/oilfield_review/ors07/sum07/p44_61.pdf.

Ahmed, T. (2010). *Reservoir engineering handbook* (4th ed. ed.). Amsterdam: Elsevier.

Al-Raoush, R., & Papadopoulos, A. (2010). Representative elementary volume analysis of porous media using X-ray computed tomography. *Powder Technology, 200*(1), 69-77. Retrieved from http://www.sciencedirect.com/science/article/pii/S0032591010000859. doi:https://doi.org/10.1016/j.powtec.2010.02.011

Amaefule, J. O., Altunbay, M., Tiab, D., Kersey, D. G., & Keelan, D. K. (1993). *Enhanced Reservoir Description: Using Core and Log Data to Identify Hydraulic (Flow) Units and Predict Permeability in Uncored Intervals/Wells*. Paper presented at the SPE Annual Technical Conference and Exhibition, Houston, Texas.

Anderson, W. (1986). Wettability Literature Survey- Part 2: Wettability Measurement. *Journal of Petroleum Technology, 38*(11), 1246-1262. doi:10.2118/13933-PA

Archie, G. E. (1950). Introduction to petrophysics of reservoir rocks. *Bulletin of the American Association of Petroleum Geologists, 34*(5), 943-961. doi:10.1306/3D933F62-16B1-11D7-8645000102C1865D

Bailey, S. (2009). Closure and Compressibility Corrections to Capillary Pressure Data in Shales. Oral presentation given at the DWLS 2009 Fall Workshop.

Bear, J., & Bachmat, Y. (1991). *Introduction to modeling of transport phenomena in porous media* (Vol. vol. 4). Dordrecht: Kluwer Academic Publishers.

Brooks, R. H., & Corey, A. T. (1964). *Hydraulic properties of porous media*. Fort Collins, Colerado: Colorado State University.

Christiansen, R. L. (2005). Chapter 15 Relative Permeability and Capillary Pressure. In J. R. Fanchi (Ed.), *Petroleum Engineering Handbook : General Engineering* (Vol. I, pp. 727-765).

Clerke, E., W Mueller, H., Craig Phillips, E., Y Eyvazzadeh, R., H Jones, D., Ramamoorthy, R., & Srivastava, A. (2008). *Application of Thomeer Hyperbolas to decode the pore systems, facies and reservoir properties of the Upper Jurassic Arab D Limestone, Ghawar field, Saudi Arabia: A "Rosetta Stone" approach* (Vol. 13).

Ebnesajjad, S., & Ebnesajjad, C. (2013). *Surface Treatment of Materials for Adhesive Bonding*. Norwich, UNITED STATES: William Andrew.

Elnaggar, O., & Temraz, M. (2018). Miocene reservoir rocks: pore throat size distribution as a strong controller on petrophysical attributes is a reflection of facies change. *Journal of Petroleum Exploration and Production Technology, 8*(3), 667-675. doi:10.1007/s13202-017-0413-4

Fanchi, J. R. (2010). *Integrated reservoir asset management : principles and best practices*. Retrieved from https://ebookcentral-proquest-com.ezproxy.uis.no/lib/uisbib/detail.action?docID=648751

Gao, B., Wu, J., Chen, S., Kwak, H., & Funk, J. (2011). *New Method For Predicting Capillary Pressure Curves From NMR Data In Carbonate Rocks*. Paper presented at the SPWLA 52nd Annual Logging Symposium, Colorado Springs, Colorado.

Glover, P. (n.d.). Petrophysics MSc Course Notes - Fluid Saturation and Capillary Pressure. Retrieved from http://homepages.see.leeds.ac.uk/~earpwjg/PG_EN/CD%20Contents/GGL-66565%20Petrophysics%20English/Chapter%204.PDF

Gomes, J., Teresa Ribeiro, M., J. Strohmenger, C., Naghban, S., & Kalam, M. (2008). *Carbonate Reservoir Rock Typing - The Link between Geology and SCAL* (Vol. 3).

Google Earth Pro. (June 19, 2015). Death Valley. 36°43'15.15" N 117°10'25.39" W, Eye alt 17.25 km. Landsat / Copernicus. (Version 7.3.2.5776).

Göppert, A. (2016). *Development of a Thomeer Analysis Software and Characterization of Capillary Pressure Data with regard to the Depositional Environment.* (Master of Science in Applied Geophysics), Delft University of Technology, Delft, Netherlands.

Green, D. W., & Willhite, G. P. (1997). *Enhanced Oil Recovery*. Richardson, UNITED STATES: Society of Petroleum Engineers.

Gunter, G. W., Finneran, J. M., Hartmann, D. J., & Miller, J. D. (1997). *Early Determination of Reservoir Flow Units Using an Integrated Petrophysical Method*. Paper presented at the SPE Annual Technical Conference and Exhibition, San Antonio, Texas.

Guo, G., A. Diaz, M., Paz, J., Smalley, J., & A. Waninger, E. (2007). *Rock Typing as an Effective Tool for Permeability and Water-Saturation Modeling: A Case Study in a Clastic Reservoir in the Oriente Basin* (Vol. 10).

Hartmann, D. J., & Beaumont, E. A. (2000). Chapter 9: Predicting Reservoir System Quality and Performance. In E. A. B. N. H. Foster (Ed.), *Treatise of Petroleum Geology / Handbook of Petroleum Geology: Exploring for Oil and Gas Traps.* (pp. 9-1 - 9-154). Retrieved from http://archives.datapages.com.ezproxy.uis.no/data/specpubs/beaumont/ch09/images/ch09.pdf

Hirasaki, G. J. (n.d.). Chapter 3 Rock Properties. Retrieved from http://www.owlnet.rice.edu/~ceng571/CHAP3.pdf

Hirsch, L., & Thompson, A. (1995). *Minimum saturations and buoyancy in secondary migration* (Vol. 79).

Lundin Norway. (2012). Edvard Grieg development brochure. Retrieved from https://www.lundin-petroleum.com/Documents/ot_Edvard_Grieg_05-12_e.pdf

Lundin Norway. (2017). Edvard Grieg. Retrieved from https://www.lundin-norway.no/2017/02/02/edvard-grieg/

Lundin Norway. (2018a). The desert dunes of the North Sea. Retrieved from https://www.lundin-norway.no/2018/03/26/the-desert-dunes-of-the-north-sea/?lang=en

Lundin Norway. (2018b). New reservoir types on the Norwegian shelf. Retrieved from https://www.lundin-norway.no/2018/02/15/new-reservoir-types-on-the-norwegian-shelf/?lang=en

Lundin Norway. (2018c). Reservoir at Edvard Grieg created by major floods. Retrieved from https://www.lundin-norway.no/2018/07/11/reservoir-at-edvard-grieg-created-by-major-floods/?lang=en

Lundin Norway. (2018d). Successful well test on Rolvsnes opens up a larger potential. Retrieved from https://www.lundin-norway.no/2018/08/27/successful-well-test-on-rolvsnes-opens-up-a-larger-potential/?lang=en

Mahmic, O., Dypvik, H., & Hammer, E. (2018). Diagenetic influence on reservoir quality evolution, examples from Triassic conglomerates/arenites in the Edvard Grieg field, Norwegian North Sea. *Marine and Petroleum Geology, 93*, 247-271. doi: https://doi.org/10.1016/j.marpetgeo.2018.03.006

McPhee, C., Reed, J., & Zubizarreta, I. (2015). *Core Analysis: A Best Practice Guide* (Vol. 64). Amsterdam, Netherlands: Elsevier Science.

Norwegian Petroleum. (n.d.). Edvard Grieg. Retrieved from https://www.norskpetroleum.no/en/facts/field/edvard-grieg/

NPD interactive FactMaps. (2019). Discovery included in field, Producing: 16/1-8 Edvard Grieg. Retrieved from http://gis.npd.no/factmaps/html_21/

Oljedirektoratet. (n.d.). Edvard Grieg. Retrieved from http://factpages.npd.no/FactPages/default.aspx?nav1=field&nav2=PageView%7CAll&nav3=21675433&culture=en

Pearson, K. (1900). X. On the criterion that a given system of deviations from the probable in the case of a correlated system of variables is such that it can be reasonably supposed to have arisen from random sampling. *The London, Edinburgh, and Dublin Philosophical Magazine and Journal of Science, 50*(302), 157-175. doi:10.1080/14786440009463897

Purcell, W. R. (1949). Capillary Pressures - Their Measurement Using Mercury and the Calculation of Permeability Therefrom. *1*(2), 39-48. doi:10.2118/949039-G

Schlumberger. (n.d.-a). water-wet. Retrieved from https://www.glossary.oilfield.slb.com/Terms/w/water-wet.aspx

Schlumberger. (n.d.-b). wettability. Retrieved from https://www.glossary.oilfield.slb.com/en/Terms/w/wettability.aspx

Shafer, J., & Neasham, J. (2000). *Mercury porosimetry protocol for rapid determination of petrophysical and reservoir quality properties*. Paper presented at the International Symposium of the Society of Core Analysts, Abu Dhabi, United Arab Emirates. http://www.ux.uis.no/~s-skj/ipt/Proceedings/SCA.1987-2004/1-SCA2000-21.pdf

Skalinski, M., & Kenter, J. (2014). *Carbonate petrophysical rock typing: Integrating geological attributes and petrophysical properties while linking with dynamic behaviour* (Vol. 406).

Speight, J. G. (2017a). Chapter 5 - Properties of Organic Compounds. In *Environmental Organic Chemistry for Engineers* (pp. 203-261). doi: 10.1016/B978-0-12-804492-6.00005-8

Speight, J. G. (2017b). *Rules of Thumb for Petroleum Engineers*. Retrieved from http://ebookcentral.proquest.com/lib/uisbib/detail.action?docID=4812517

Swanson, B. F. (1981). A Simple Correlation Between Permeabilities and Mercury Capillary Pressures. *Journal of Petroleum Technology, 33*(12), 2498-2504. doi:10.2118/8234-PA

Tavakoli, V. (2018). *Geological Core Analysis: Application to Reservoir Characterization*. Cham: Springer International Publishing.

The University of Auckland. (n.d.). Conglomerate. Retrieved from https://flexiblelearning.auckland.ac.nz/rocks_minerals/rocks/conglomerate.html

Theologou, P. N., Skalinski, M., & Mallan, R. K. (2015). *An MICP-Based Pore Typing Workflow – Core Scale to Log Scale*. Paper presented at the SPWLA 56th Annual Logging Symposium, Long Beach, California, USA.

Thomeer, J. H. M. (1960). Introduction of a Pore Geometrical Factor Defined by the Capillary Pressure Curve. *Journal of Petroleum Technology, 12*(3), 73-77. doi:10.2118/1324-G

Thomeer, J. H. M. (1983). Air Permeability as a Function of Three Pore-Network Parameters. *Journal of Petroleum Technology, 35*(4), 809-814. doi:10.2118/10922-PA

Vavra, C. L., Kaldi, J. G., & Sneider, R. M. (1992). Capillary Pressure: Part 5. Laboratory Methods. In D. Morton-Thompson & A. M. Woods (Eds.), *Methods in Exploration Series. Development geology reference manual* (Vol. No. 10, pp. 221-225).

# Appendix A: Comparison Study of Curve Fitting Parameters

A small comparison study of the curve fitting parameters of the Thomeer model and the Gaussian model was performed to investigate whether one model would prove to be significantly better than the other. The study was conducted using scatter plots of permeability measured by CCA against the curve fitting parameters of the two models. This is illustrated in Figure A.1. There are six plots, one for each curve fitting parameter. The grey hollow circles are data points, while the red lines are non-weighted regression lines.

Permeability measured by CCA is plotted against the Thomeer fitting parameter $P_{d,1}$ and the Gaussian fitting parameter $P_{m,1}$ in Figure A.1 (a) and (d), respectively. The correlation factor ($R^2$) is higher for $P_{m,1}$ than $P_{d,1}$. However, the trends are similar and the lower $R^2$ for $P_{d,1}$ is probably a result of unweighted regression due to there being slightly more spread in the data from the Thomeer model.

Permeability measured by CCA is plotted against the Thomeer fitting parameter $V_{b\infty,1}$ and the Gaussian fitting parameter $V_{b\infty,1}$ in Figure A.1 (b) and (e), respectively. The trends are similar for both models. There is slightly more spread in the data from Thomeer. $R^2$ is low for both models.

Permeability measured by CCA is plotted against $G_1$ and $S_1$ in Figure A.1 (c) and (f), respectively. $R^2$ is low for both models.

In conclusion, this study suggests that there is not a significant difference in the correlations between permeability and the curve fitting parameters of the Thomeer model compared to the Gaussian model, at least for the samples investigated from the QC filtered MICP database. The QC process described in Chapter 5.1 is based on Thomeer curve fitting results, so these parameters were used in further analyses.
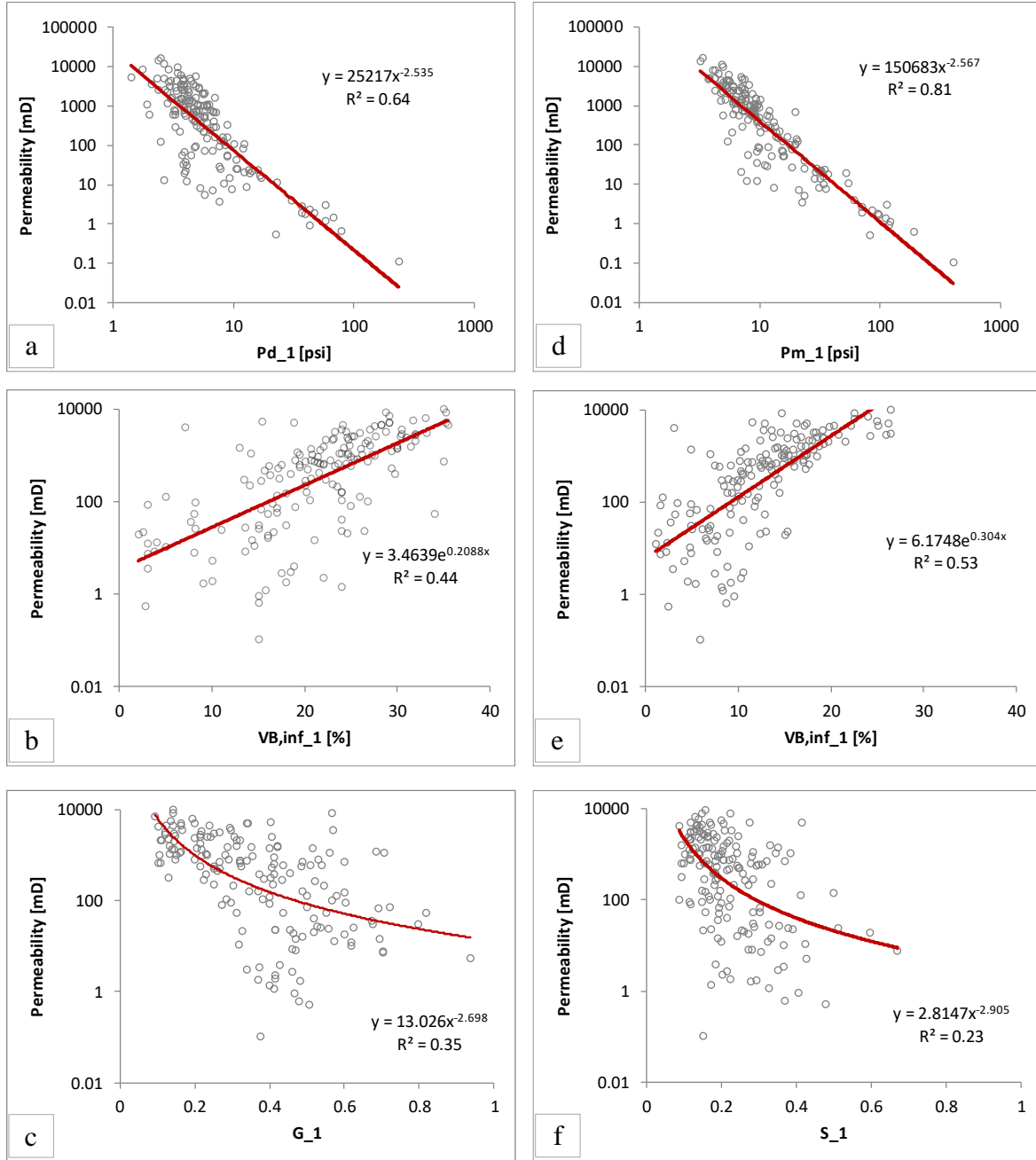
*Figure A.1: Permeability measured by CCA is plotted against Thomeer parameters (a) $P_{d,1}$, (b) $V_{b\infty,1}$, and (c) $G_1$, respectively. Permeability is plotted against modified Gaussian parameters in (d) $P_{m,1}$, (e) $V_{b\infty,1}$, and (f) $S_1$ , respectively. The grey hollow circles are data points while the red lines illustrate the trend.*